VIBRATION SENSORS UTILIZING

FIBER FABRY-PEROT INTERFEROMETERS

AND PERMANENT MAGNETS

A Dissertation

by

ANDREW P. CONKEY

Submitted to the Office of Graduate Studies of
Texas A&M University
in partial fulfillment of the requirements for the degree of

DOCTOR OF PHILOSOPHY

August 2007

Major Subject: Interdisciplinary Engineering

VIBRATION SENSORS UTILIZING

FIBER FABRY-PEROT INTERFEROMETERS

AND PERMANENT MAGNETS

A Dissertation

by

ANDREW P. CONKEY

Submitted to the Office of Graduate Studies of
Texas A&M University
in partial fulfillment of the requirements for the degree of

DOCTOR OF PHILOSOPHY

Approved By:

Co-Chairs of Committee,	John Vance
	Arun Srinivasa
Committee Members,	Ohannes Eknoyan
	Luciana Barosso
	Henry F. Taylor (in memoriam)
Head of Department,	N.K. Anand

August 2007

Major Subject: Interdisciplinary Engineering

ABSTRACT

Vibration Sensors Utilizing Fiber Fabry-Perot Interferometers

and Permanent Magnets. (August 2007)

Andrew P. Conkey, BS Texas A&I University;

MS, Texas A&M University-Kingsville

Co-Chairs of Advisory Committee: Dr. John Vance
Dr. Arun Srinivasa

A unique set of vibration sensors was designed that incorporate the fiber Fabry-Perot interferometer (FFPI) and permanent magnets. Feasibility of the design and its advantages over traditional sensors were verified by experiments. The new sensors consist of one that monitors the motion of a body across an air gap with the other designed to respond to the motion while in contact with the vibrating body. The FFPI is the device used to transmit the vibrational response while permanent magnets are used to transfer the vibratory motion to the FFPI.

In the non-contacting sensor, a permanent magnet was used as the motive to transfer the vibratory motion to be registered at the FFPI. Although the magnet resulted in a non-linear response, the effect of the non-linearity can be removed by signal processing. The fiber optic gap sensor (FOGS) developed has a sensitivity of 250 mV/mil for a 30 mil gap to 50 mV/mil for a 65 mil gap and a dynamic range up to 820 Hz. An advantage of the FOGS over traditional eddy current based gap sensors (ECP), for measuring rotor vibration, was demonstrated with a test rotor face that had brass strips attached to it. The FOGS response was not affected by the strips whereas the

response of the traditional ECP was greatly affected by the strips. This demonstrated the potential of the FOGS for measuring the motion of a coated shaft.

The fiber optic vibration sensor (FOVS) had a marginal response as its construction led to spurious signals. The feasibility of it to act as a vibration sensor, however, was demonstrated. Due to problems in maintaining the proper gap between the proof mass and sensor head during assembly the natural frequency of the FOVS was around 31 Hz and not the targeted 10 Hz.

The sensors presented were meant to be a first generation. However, access to additional FFPI elements was restricted limiting further development. Improvements to the sensors would be to modify the sensing head, magnet size, and the embedment of the FFPI as well as to employ tighter machining precision and assembly practices.

DEDICATION

This work is dedicated to many people who have left enduring memories for me to draw upon to see the completion of this work. Although it will be hard to name them all, I do need to acknowledge some. First, I would like to dedicate the work to my wife, April, for enduring with the trials and tribulations to reach this point. Second, I would like to dedicate this work to my parents, Ron and Carol Conkey, and my brother David and my sister Maureen and her family for their continued support throughout my long academic career. My extended family, Thelma Torres and Carlos Torres and my other in-laws, deserve acknowledgement for their support over the years too. Lastly, I would like to dedicate the work to Carter Harrington, Dr. Henry F. Taylor and Dr. Robert McLachlan, who all left in an untimely fashion.

ACKNOWLEDGMENTS

There are a number of folks who have been very supportive over the years. Each person provided some facet that enabled this work to reach this point. These people are Robert X. Perez, Robert A. Atkins, Jim Gardner, Dr. Arun Srinivasa, Dr. Dara Childs, Malcom Leader, Dr. Christi Madsen, Dr. John Vance, and Steve Smith.

TABLE OF CONTENTS

Page

Page

LIST OF FIGURES

Page

Page

Page

Page

Page

LIST OF TABLES

Page

1 INTRODUCTION

Monitoring vibration of machines that operate in hazardous environments with electrically based sensors requires extensive protection and stringent guide lines to insure that the chance of an electrical spark setting off an explosion does not occur (NEC 70, API 670) [1, 2]. Examples of such environments are facilities that are classified as Class I Locations. Class I Locations are areas where gases or vapors are present in the air at sufficient levels to produce an ignitable mixture [2]. Examples of such locations are reciprocating compressors used to process hydrogen. Although the threat of explosion maybe minimal, as sensors for these systems require them to be intrinsically safe, there still exists the threat of explosion due to a frayed wire, loose connection, or other type of electrical problem. The added cost to ensure that a monitoring system is intrinsically safe is about 20 to 30% of the total installation cost [3]. In addition, there are environments that can create problems for applying many existing vibration sensors. Areas that have high intensity electromagnetic fields, including high intensities of radio frequencies, or situations where there are stray currents are examples of such harsh environments [4].

One other problematic area is when raw signals from electrical based sensors are transmitted over distances greater than 1000 ft. (305 m) [5]. The transmission of the signal from electrically based sensors is strongly influenced by cable runs greater than 1000 ft (305 m) due to a combination of accumulated resistance and capacitance which

---

This dissertation follows the style of the ASME Journal for Vibration and Acoustics.

tend to cause a roll off on the upper frequency that can be monitored along with a phase change. Although technology to amplify or transmit the signal through wireless means is available, placement of these devices may not be practical or allowed due to interference and security reasons. Mono-mode fiber optic cables can have runs over 59,000 ft (18 km) before a 3db attenuation of the signal occurs while many electrically based systems can only have runs of 10,000 ft (3 km) before a 3db roll-off occurs. In fact, API 670 sets restrictions on the length of cable used to connect the transducer to the signal conditioning system for both accelerometer and eddy current proximity sensors. The development of vibration sensors that incorporate fiber optic technology would lead to a set of sensors that are passive in operation in that they would not rely on any electrical source to translate the vibratory motion into a signal. In addition, a fiber optic based system would also be immune to electromagnetic fields and electrical noise and provide a means to monitor machinery over distances greater than 1000 ft (305 km) with minimal degradation of the raw signal.

A solution to these issues is implementing the fiber Fabry-Perot interferometer (FFPI) as the primary sensing element in a vibration transducer. The FFPI is embedded in an optical fiber and has the all the benefits associated with optical fibers along with the capability of high strain sensitivity. Fiber optic sensors are essentially passive devices, as they do not rely on an electrical power source to activate the sensing mechanism and have been proven in harsh environments [6, 7, 8]. The laser light that is used to monitor the change in the sensor is low power. That is, there is no spark source within the sensor. Additional advantages of using fiber optics are low attenuation of

fiber optics to allow for monitoring over long distances and an optically based sensor are immune to high electro-magnetic fields [4]. Vibration sensors that are non-electrical based could reduce some of the extensive safety measures required to make an electrical based sensor operational in a hazardous environment.

Application of the Fabry Perot interferometer technique for the measurement of vibrations is not new. However, most research has been for generating a general-purpose accelerometer or accelerometers at the micro-scale [9, 10, 11, 6]. The configuration for these systems consists of a bare fiber in a cantilever beam configuration as opposed to an axial orientation. In addition, these systems often implement the extrinsic mode of operation relying on light reflecting over an air gap. Extrinsic configurations are often difficult to align and contamination of the gap can degrade the quality of the signal.

Optical methods have been employed to monitor proximity motion by using reflected light over an air gap. Two examples of this method of approach are fiber optic bundles that monitor light reflected from the target and laser-Doppler vibrometers [12, 13]. Both of these methods can be influenced by the finish of the target surface and by a dirty air gap. A rough surface of a target could cause a high amount of scatter of the signal. Another application attaches a fiber to a diaphragm that has a magnet attached to it. The overall construction of this method may not be practical as the fiber could be susceptible to undesirable motion.

The FFPI technology has been applied successfully in a wide range of condition monitoring applications that range from pump cavitation, monitoring of cylinder

pressures on large diesel engines, to rail road bridge monitoring [6, 7, 8]. The technology has also been adapted to the monitoring of roller element bearing loads too [14]. Each of these environments demonstrates the ability of the FFPI to withstand a wide range of loadings.

The intent of this dissertation is to demonstrate that non-contacting and contacting vibration sensors utilizing permanent magnet and fiber Fabry-Perot interferometer technologies can be developed. Section 2 will cover core concepts for vibration sensors, permanent magnets, and fiber Fabry-Perot interferometry. Section 3 will present how the concepts from Section 2 can be applied to the proposed sensors and what demonstrate what can be expected from the testing. Testing strategies and objectives will be discussed in Section 4. Resulting data for each prototype sensor from each test will be covered in Section 5. Section 6 will cover a final commentary and present future research issues.

2 BASICS OF VIBRATION SENSORS, PERMANENT MAGNET APPLICATION, AND FFPI APPLICATION

2.1 Introduction

The following discussion will present the core ideas and relations that are applied for the vibration sensors that were developed. The sensors that were developed require an understanding of concepts in vibrations, permanent magnets, and fiber interferometery. To understand the role that each technology contributes in the operation of the sensors it is necessary to establish the fundamental principals from each technology. By presenting the vibration theory that demonstrates the core components of a vibration sensor this will lead into understanding the core concepts of permanent magnets, then into the core concepts of the FFPI. Finally, a summary of how the three concepts are combined to produce a means for examining the response of a given sensor.

Vibration monitoring is conducted on a machine so that information on how it is moving is obtained. The measure of the motion can be in displacement, velocity, or acceleration. The operating speed of the machine often dictates the motion criterion used to establish nominal operating guidelines. As an example, reciprocating compressors normally operate around 600 rpm (10 Hz) and displacement and velocity criterion are applied, where as a turbine or gearboxes operating at 36000 rpm (600 Hz) might rely on acceleration criterion [15, 16]. In addition, when it is desired to verify machine models displacement is often the output from the model and having displacement data from the actual machine would make comparison more applicable.

2.2 Vibration Sensors

The motion of a vibrating body can be measured by being in contact or not in contact with the body in question. Vibration sensors that are in contact with the body general rely on the motion of the body to cause the sensor to be excited and produce an output signal that corresponds to the level of excitation, or vibration. Non-contacting vibration sensors require a means to respond to the vibration over a gap. To accomplish this there needs to be a means to act across a gap.

2.2.1 Contacting Vibration Sensors

Vibration sensors that rely on contact with the vibrating body in question typically consist of four elements. The mass, spring, and damping of the sensor are three of the elements. The fourth element represents how the motion of the proof mass relative to the base is converted to a signal. The modeling of the system assumes that the proof mass is lumped, the stiffness and damping are linear, and that the base excitation can be represented by a single harmonic function with an excitation frequency of ω. Figure 2.1 shows the relationship of the three elements.

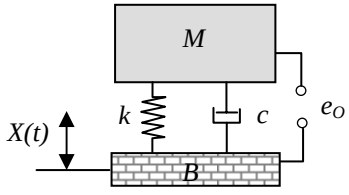

Vibration sensor model of components: *M*-Proof mass,
k-spring element, *c*-damping element, *B*-excited base, e_O-electrical signal

Figure 2.1 Components of a Seismic Based Vibration Sensor

The fourth element typically is based either on piezoelectric, capacitance, or induction principles and typically generate a voltage, e_O, that is monitored. The measure of motion, whether it is displacement, velocity, or acceleration, is often associated with the relationship that defines the output voltage to the motion. Piezoelectric sensors are often associated with acceleration measures as the voltage is a function of the acceleration of the proof mass. However, there is a critical distinction between how the piezoelectric response model compares to the seismic model presented. The seismic accelerometer model presented above in figure 2.1 assumes that the output e_0 is a function of the relative motion, whether it is displacement, velocity, or acceleration, between the proof mass and the housing. This is not the model that defines how a piezoelectric accelerometer responds. A piezoelectric based accelerometer actual responds due to the inertial accelerations acting on the crystal and thus provides an absolute measure. The confusing aspect for this is that the resulting response curves for the seismic accelerometer and the piezo based accelerometer are similar. Also, piezoelectric sensors typically are designed so that the natural frequency (10 to 50 kHz) of the sensor is higher than the frequency to be measured. Further discussions regarding accelerometer responses will be based on the seismic system model. Capacitance and inductance based sensors typically have outputs that are a function of velocity or displacements. Also, the natural frequencies (1 to 10 Hz) of velocity and displacement based systems are typically lower than the frequency to be measured when applied as seismometers to monitor displacement motion.

The expression that is generally used to express the relationship between the motion of the proof mass *M* and the base *B* can be obtained from the equation of motion based on the relative motion between the two bodies. Figure 2.2 shows the assumed motion (a) and the resulting free body diagram (b). The equation of motion for this system is

$$M\ddot{\delta} + c\dot{\delta} + k\delta = M\ddot{X} \tag{2.1}$$

where *M* is the proof mass, *c* is the damping value, *k* is the stiffness, and δ=*X*-*Y* defines the relative motion between the absolute motion of the proof mass, *Y(t)*, and the absolute motion of the base, *X(t)*. Equation (2.1) can be restated by dividing through by the mass, *M*, yielding

$$\ddot{\delta} + 2\zeta\omega_n\dot{\delta} + \omega_n{}^2\delta = \ddot{X} \tag{2.2}$$

where $\omega_n = \sqrt{k/M}$ and $c/M = 2\zeta\omega_n$ where ζ defines the damping factor. By assuming

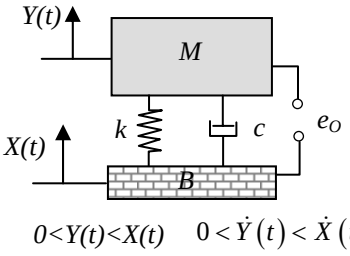

a) Kinematic Diagram

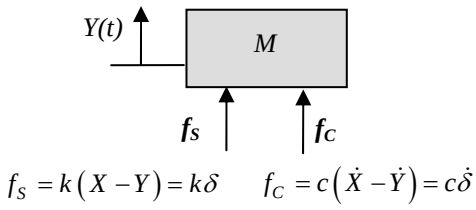

b) Free Body Diagram

Figure 2.2 Kinematic and Free-Body Diagrams for the Seismic Model

that the base excitation, $X(t) = X_0 \sin(\omega t)$, is a sinusoidal motion at a single frequency

of ω, a relationship can be obtained that relates the relative displacement, δ, to the base excitation amplitude, X_O

$$\frac{\delta}{X_O} = \frac{r^2}{\sqrt{\left(1-r^2\right)^2 + 4\zeta^2 r^2}} \tag{2.3}$$

where $r=\omega/\omega_n$. Equation (2.3) provides an indication of the input X_0 to the relative output motion δ. Again, the model also assumes that the output signal, e_0 is related to δ so equation (2.3) also provides a relation between the excitation X_0 and the output response e_0. This defines the relation for the response of a seismic based vibrometer. A second relationship that is required identifies the phase between the motion of the base and the proof mass. This relation is found to be

$$\phi = \tan^{-1}\left[\frac{2\zeta r}{1-r^2}\right] \tag{2.4}$$

Figure 2.3 shows a plot of eq. (2.3) for a $\xi=0.07$ and for $\zeta=0.7$ and figure 2.4 shows the

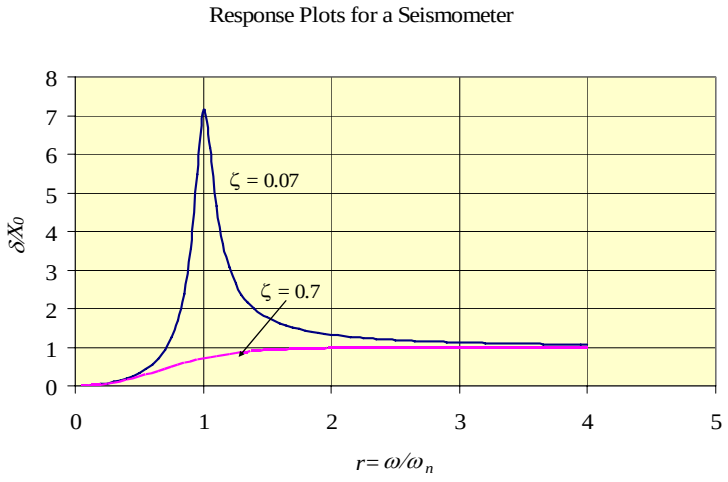

Figure 2.3 Seismometer Response Curve

shift in phase of the proof mass *M* relative to the base motion. Figures 2.3 and 2.4 are

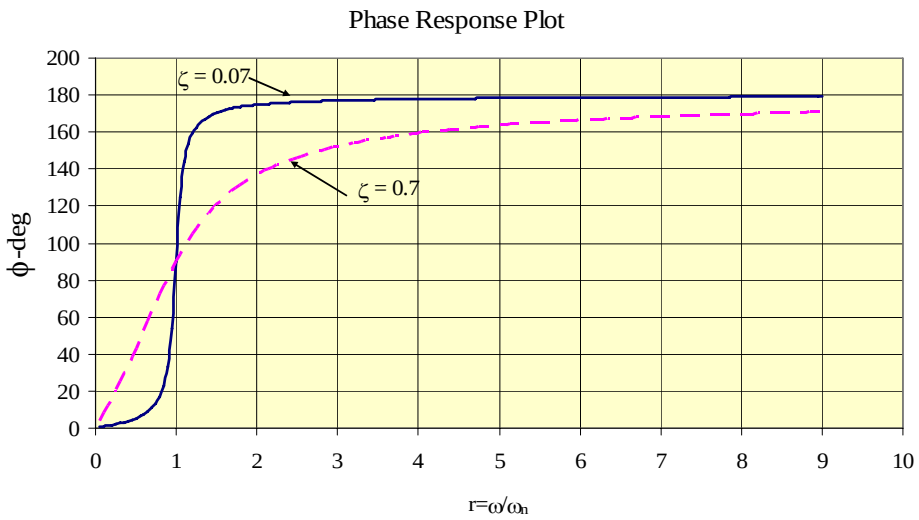

Figure 2.4 Phase Response

used to aid in establishing the range of performance for a seismometer vibration sensor and they can also be used as a correction factor so that the observed signal can be adjusted to show the correct measure of the excitation.

Equation (2.3) represents the response for a vibration sensor that is configured as a seismometer. Equation (2.3) can be restated to represent the response for a sensor configured for acceleration, or an accelerometer, or for one to represent the response of a sensor configured for velocity. This is accomplished by noting that the absolute peak response between displacement, velocity, and acceleration are expressed as X_0, $X_0\omega$, and $X_0\omega^2$, respectively. So, this allows equation (2.3) to be restated as

$$\frac{\delta\omega_n}{X_0\omega} = \frac{v_\delta}{v_{X0}} = \frac{r}{\sqrt{\left(1-r^2\right)^2 + 4\zeta^2 r^2}} \tag{2.5}$$

for a velocity sensor, and

$$\frac{\delta{\omega_n}^2}{X_0\omega^2} = \frac{a_\delta}{a_{X_0}} = \frac{1}{\sqrt{\left(1-r^2\right)^2 + 4\zeta^2 r^2}} \tag{2.6}$$

for a seismic based accelerometer. Figures 2.5 (a) and (b) demonstrate the respective responses for equations (2.5) and (2.6).

The phase expression for each of the cases shown is the same as that presented in equation (2.4) as the phase is dependent upon the quantities in the denominator for each expression, as long as the respective motions are the same. The phase would need to be adjusted if the comparison were to change. That is, if the displacement response was to be compared to a velocity measure, then a 90^0 factor would need to be applied while a 180^0 factor would be needed if the output displacement was to be compared to acceleration.

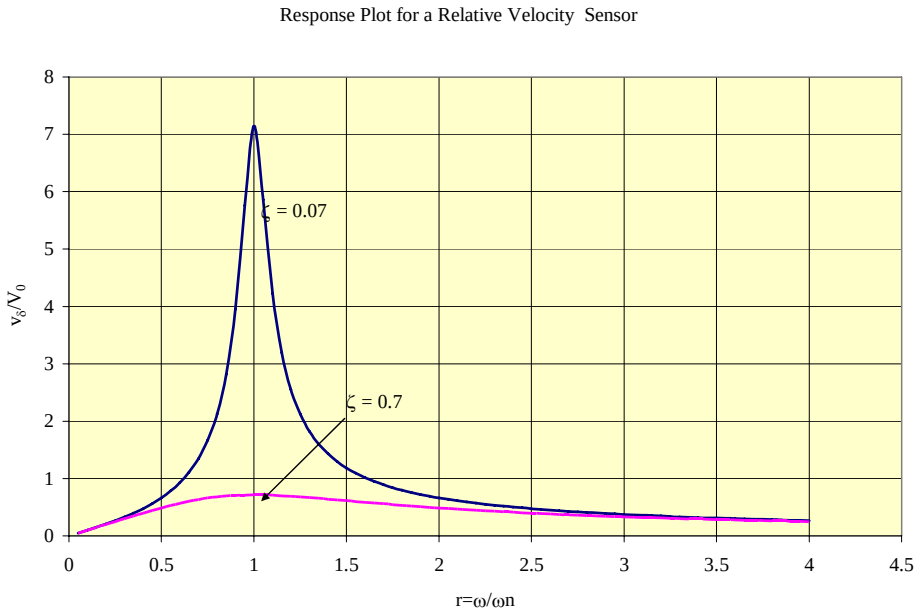

(a) Response Plot for a Velocity Sensor.

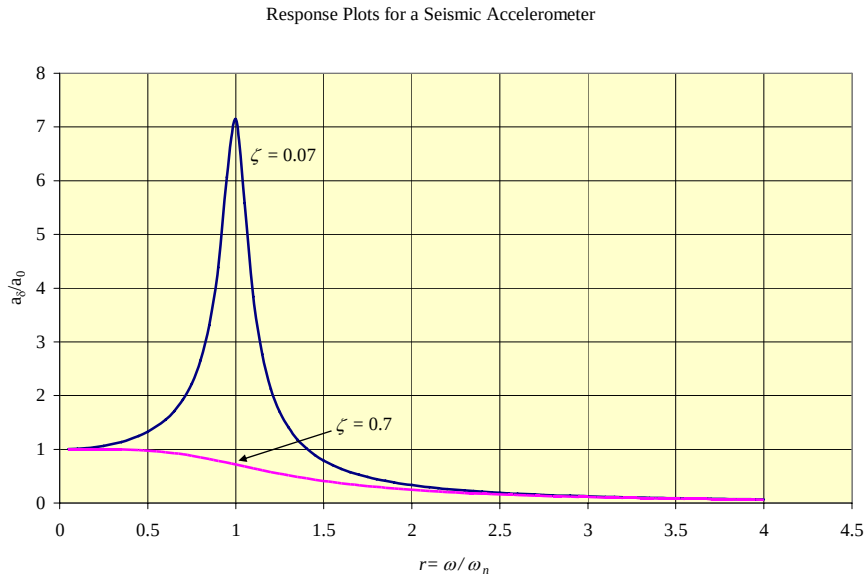

(b) Response Plot for a Seismic Accelerometer.

Figure 2.5 Response Plots for Velocity and Seismic Accelerometer

The distinction as to whether a vibration sensor is a seismometer, velocity sensor, or accelerometer is generally based upon how the relative motion between the proof mass and base is converted into a usable signal. The operating point of the vibration sensor relative to the maximum peak response, around *r=1,* is also of significance. It is worth noting that for these systems, due to the presences of damping, the peak response of the system does not occur when the frequency ratio is one. Ideally it is desired that the response of the sensor be independent of the excitation frequency. Examination of the response curves in figures 2.3, 2.5(a) and 2.5(b) shows that there are regions where a flat response condition is observed. For seismometers, typically, this occurs to the right of the response peak, for accelerometers this occurs to the left of the response peak. Velocity sensors do not have regions where the response is truly flat, nor do they approach a constant value of one; but far to the right of the response peak, there is a region where the response level slowly changes. Also, if the damping is sufficiently high, the region around *r=1* is fairly flat and is useable. Table 2.1 shows how assuming conditions on the operating point allows for simplification of the response expressions.

Table 2-1 Response Expressions

Motion Measured	Expression	Operating point	Reduced Expression
Displacement	$G(r)\frac{\delta}{X_O} = \frac{r^2}{\sqrt{\left(1-r^2\right)^2 + 4\zeta^2 r^2}}$	r>>1	$\frac{\delta}{X_O} \cong \frac{r^2}{r^2} = 1$
Velocity	$H(r) = \frac{\delta\omega_n}{X_0\omega} = \frac{v_\delta}{v_{X0}} = \frac{r}{\sqrt{\left(1-r^2\right)^2 + 4\zeta^2 r^2}}$	r>>1	$\frac{v_\delta}{v_{X0}} \cong \frac{r}{r^2} = \frac{1}{r}$
Acceleration	$J(r) = \frac{\delta\omega_n^{\,2}}{X_0\omega^2} = \frac{a_\delta}{a_{X_0}} = \frac{1}{\sqrt{\left(1-r^2\right)^2 + 4\zeta^2 r^2}}$	r<<1	$\frac{a_\delta}{a_{X_0}} \cong \frac{1}{1} = 1$

Another distinction between accelerometers and seismometers is that accelerometers generally rely on a “hard” spring, or a really stiff system, producing a high natural frequency, versus seismometers that rely on a “soft” spring mounting of the proof mass.

It should be pointed out that the solution for the equation of motion of eq. (2.3) assumed a single excitation frequency. However, vibrations rarely consist of a single sinusoidal wave. Since the equation of motion eq. (2.1) is linear, the principle of superposition can be applied, and equations (2.3) and (2.4) are valid for any combination of frequencies. But, for practical applications, it is useful for the response to be independent of excitation frequency.

Phase, or the lag between the response of the proof mass to the excitation, is another property that needs examination. Inspection of Figure 2.4 for the low damping factor value of 0.07 shows the accelerometer response, values of $r << 1$, the phase

difference is nearly zero for all excitation frequencies, ω. The second case, *r>>1*, the phase becomes approximately 180^0 for all excitation frequencies. However, as the damping factor is increased, the phase response curves do not display zones of zero of 180^0 phase change.

The damping factor ζ is critical too, as it does extend the range at which equations (2.3) and (2.6) are applicable. Table 2.2 shows relations that can be used to determine when the peak response for each case will occur for a given value of the damping factor ζ [17]. Figures 2.6 and 2.7 show how damping can cause an increase in the "flat" region of the curve for the seismometer and accelerometer response motions. Figure 2.8 shows how the response of the velocity sensor configuration results in damping reducing the peak at *r=1* but having all the damping cases converging to a common response trend for $r > 5$. A note on figure 2.7 is needed as the response shown would give the impression that the sensor would work if no excitation is present. This is not the case. Generally, there is a threshold vibration level that is required to achieve the threshold response for the sensing element to respond.

Table 2-2 Peak Response and Damping

Motion Measured	Expression for Peak Response in terms of ζ
Displacement	$r_{\max} = \frac{1}{\sqrt{1-2\zeta^2}}$
Velocity	$r_{\max} = 1$
Acceleration	$r_{\max} = \sqrt{1-2\zeta^2}$

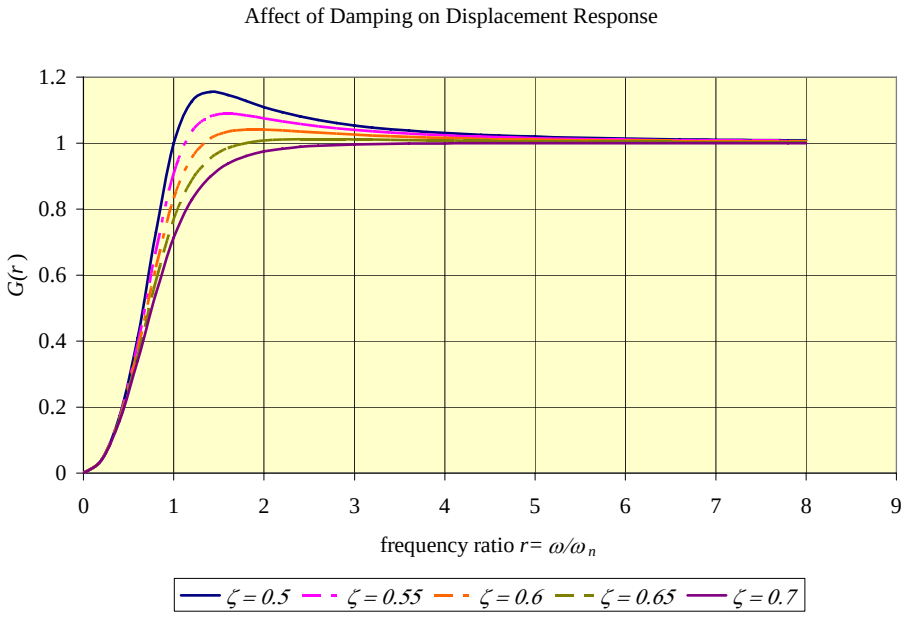

Figure 2.6 Seismometer Response for Various ζ

Values for ζ ranging from 0.65 to 0.70 are typical for most vibration sensors [18]. A high damping factor can also protect the sensor if it ever goes through a resonance response, which is quite possible if it is operating as a seismometer.

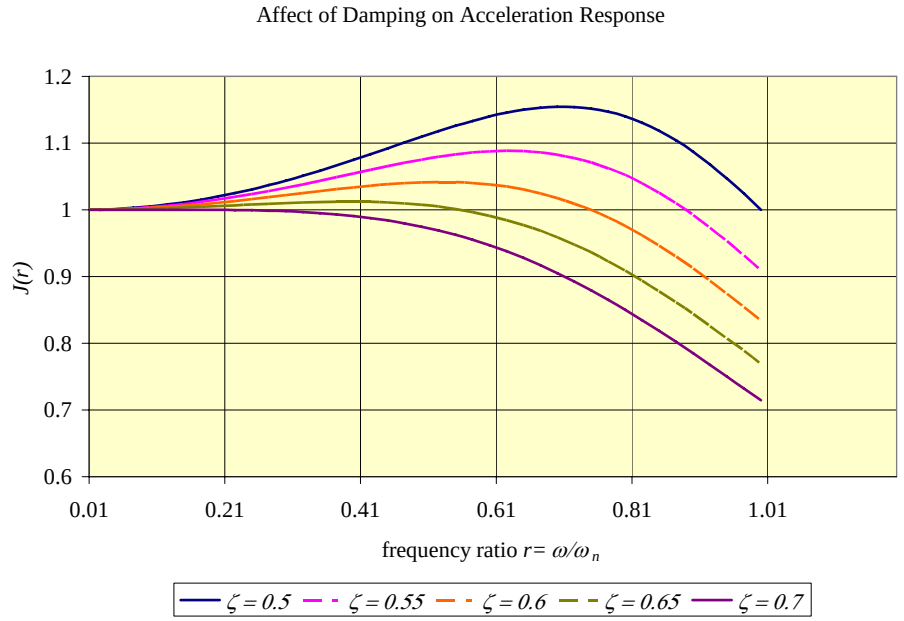

Figure 2.7 Accelerometer Response for Various ζ

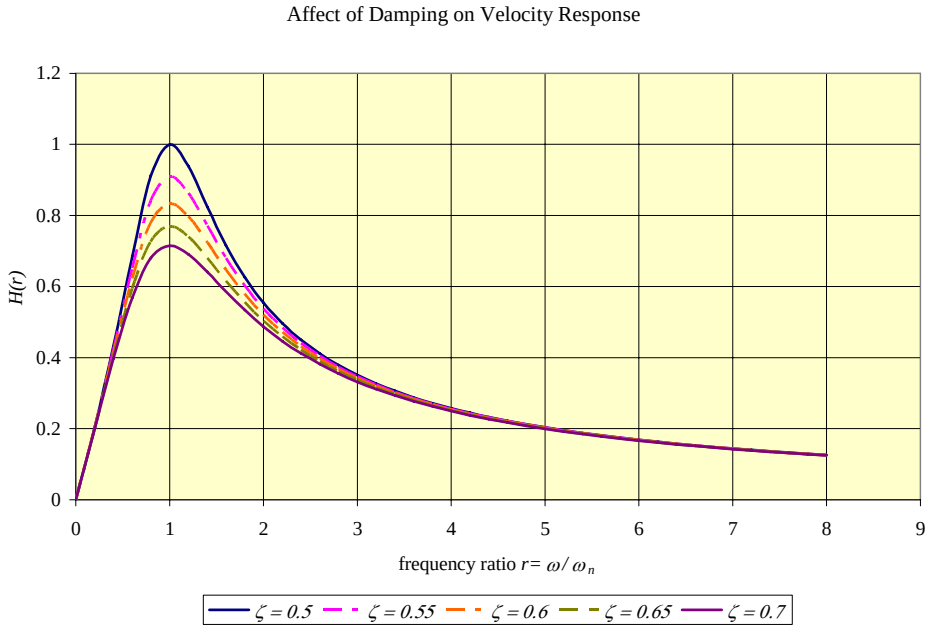

Figure 2.8 Velocity Sensor Response for Various ζ

2.2.2 Seismometer Configuration

The seismometer configuration will be applied for the initial application of the fiber Fabry-Perot interferometer (FFPI) to monitor displacement vibrations. The sensor will consist of a mandrel, or sensing post, that will contain the FFPI element, a load plate that is acted upon by a set of springs loaded by a proof mass, figure 2.9 demonstrates two possible configurations.

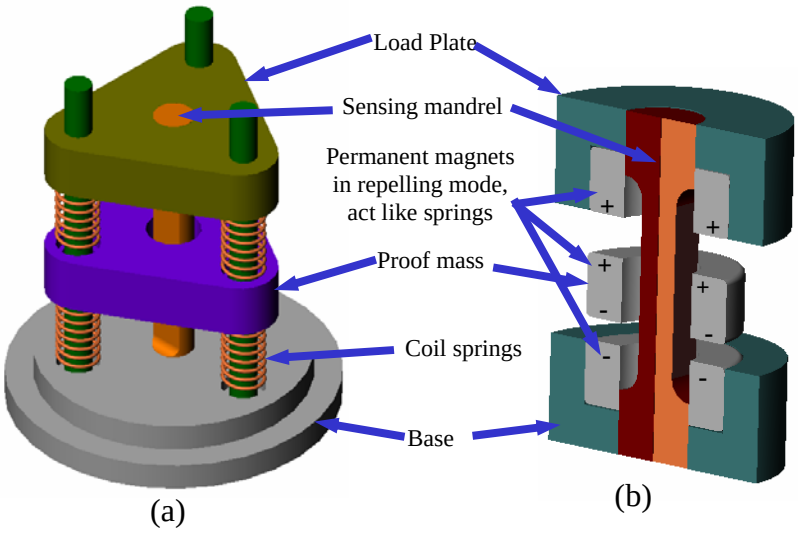

Figure 2.9 Fiber Optic Based Seismometers

The left configuration, figure 2.9(a), utilizes coil springs as the stiffness elements, which is typical for most industrial seismometers, while the right configuration, figure 2.9(b) utilizes permanent magnets repelling each other as the stiffness elements. The principal of the operation is that as the base is excited at a frequency above the natural frequency of the proof mass, the force in the springs

between the load plate and the proof mass will vary. These two sensors utilize a “soft” mount system and can be classified as a seismometer. The load plate, which is rigidly attached to the sensing post, will transfer the change in spring load to the mandrel, and hence, to the FFPI sensor. The three posts in figure 2.9(a), which constrain the springs, are only attached to the base plate, that is, both the load plate and the proof mass are free to move along the guideposts. The damping in these configurations can be provided by the addition of fluid once the assemblies are encased in a housing. Again, the sensing mandrel will provide a means for the FFPI to react to the relative change in motion between the proof mass and the base. The assembly shown in figure 2.9(a) has disadvantages in that the coil spring are subject to fatigue and could fail, matching six coils springs such that the proof mass is level could be tasking, and there are six points of possible contact friction (three between the proof mass and guide rods and three between the load plate and guide rods. The second assembly, figure 2.9(b), utilizing the permanent magnets in a repelling mode, requires that the proof mass has a suitable guide and the primary potential point of friction contact would be between the proof mass and the sensing mandrel or housing (not shown). The advantage of the system shown in figure 2.9(b) is that there are no mechanical components that could fail due to fatigue

2.2.3 Non-Contacting, or Gap Vibration Sensors

Non-contacting vibration sensors, or gap sensors, utilize a change in a gap measurement to correlate a vibration measure. The vibration signal resulting from a change in gap is actually a measure of relative motion. Figure 2.10 shows the two sides

of the gap, *A* the sensor and *B* the target. The resulting oscillatory motion of the gap could result due to three possible relative motions: 1) the probe is fixed and the target

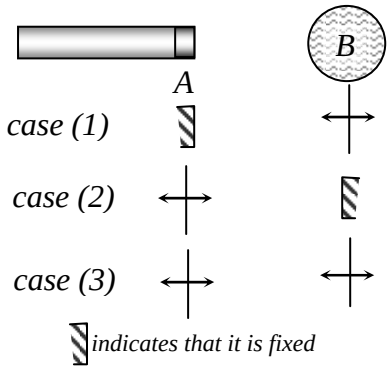

Figure 2.10 Relative Motion for a Gap Sensor

moves, 2) the target is fixed and the probe moves, and 3) both probe and target move. Case 3) is inherent in all applications, but most of the time the motion of the sensor is within in the noise level of the sensor and case 1) applies. However, there are instances when the motion of the sensor does mask the true response of the target. The desired output of a gap monitoring system is expected to be linear with respect to the gap change. Sensors that monitor gap changes generally rely on monitoring how an electromagnetic field or electrostatic field is altered as the gap changes. The challenge here is the relation between the change in the developed field is generally non-linear in nature and requires some means for linearization. Systems that utilize eddy current fields or capacitance rely on the electrical properties associated with a gap change. Another issue that can often arise with proximity based probes is the ability of putting probes, namely eddy current based probes, too close to each other as their fields can generate

cross-talk issues. Eddy current probes operate by having a current pass through a coil of wire wrapped around a core. As the target distance varies, this changes the eddy current field and causes a modulation of the primary current that generates the field. The change in the eddy field is a non-linear behavior, but a complete sensor system incorporates a linearizing circuit to produce a linear output. In addition, the permeability of the gap of an eddy current probe can affect the probes response. Essentially any metallic crystalline structure will influence the eddy field. This makes successful operation very dependent on the quality of the target surface. Another option is to utilize the magnetic force of attraction that is produced when a magnet is brought within proximity of suitable target, namely a ferromagnetic material, figure 2.11. The strength of attraction developed by a permanent magnet is a function of the magnetic properties of the material. Paramagnetic materials, such as aluminum and brass, that would affect an eddy current probe, would have little to no affect on the field generated by a permanent magnet.

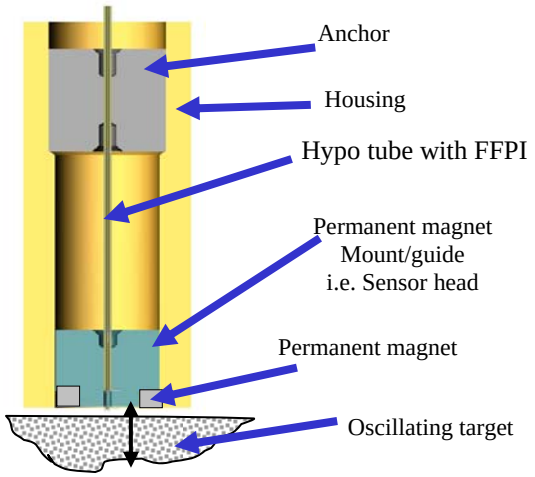

Figure 2.11 Fiber Optic Gap Sensor Configuration

The sensor configuration shown in figure 2.11 utilizes a magnet that is mounted on a sensor head that is attached to a strain tube that contains the FFPI. As the sensor head is brought within proximity of a target, the force developed between the magnet and the target will strain the tube, thus straining the FFPI. This system assumes that the tube will act as a "hard" spring. Section 3 will show that although the force of attraction is non-linear, it is possible to assume a linear response for "small" ranges of motion, and, if the range of motion is "large" a calibration scheme can be applied to preserve the excitation.

The focus of this research is to develop a set of vibration sensors, contacting and non-contacting, that incorporates the FFPI to measure the vibratory response of the sensors. The primary mechanism that will be utilized to transfer the vibratory response to the FFPI is through use of permanent magnets. The primary mechanism for sensing the changes, and hence the vibratory motion, within each sensor is through the FFPI.

2.3 Permanent Magnet Theory Basics and Background

2.3.1 Magnet Material and Geometry

Permanent magnets are the elements that provide the motive for transferring the vibratory excitation to the FFPI element. Permanent magnets can provide a force that can act over a gap, be formed into geometries that can optimize performance and space, and now have a robust nature that permits them to be used in vibratory type of environments.

Permanent magnets are utilized for a wide variety of applications because they have the capability of producing a large motive for a small volume, can be easily formed

into compact shapes, and the robustness has greatly improved. One class of permanent magnets is the rare earth category. One such example of rare earth magnets are neodymium iron boron, NdFeB, which are incorporated into the developed sensors. These magnets have one of the highest field strengths per volume and can operate with minimal loss of the field over a wide range of environmental conditions. In addition, most rare earth magnets like NdFeB can be molded into almost any configuration and it can be obtained in a flake form which could allow it to be embedded directly on the FFPI. The application of the permanent magnets for this research is for their ability to generate an attracting or repelling force over a gap. The actual analysis of the developed field between the permanent magnet and target surface is thoroughly discussed in numerous texts, so only key concepts will be presented here. Key concepts that are relevant for thought here are how do the magnetic field lines interact, how do the magnetic quantities contribute and included, how are the field lines expressed and how do they relate to the force developed. The discussion here is to show how the magnetic field, and hence the resulting force, is a non-linear in nature. The intent of the research is not to optimize the performance, but rather to understand what properties will influence the response of the sensors. For this reason, the core concepts of the relations for magnetic field, force, and gap change will be presented by discussing the core concepts.

2.3.2 Performance

The performance of the gap sensor and the vibration sensor that incorporate permanent magnets can be approximated using field equations that are based on the existing magnet geometries. Factors that can influence the behavior of the actual device that may not be accounted for in the preliminary models are flux leakage, temperature changes, actual available magnetic field, and influence of shock. Advancements of permanent magnets have increased the available energy and the stability of their properties [19, 20] so that the development of passive proximity sensor is feasible. Parameters such as flux leakage and actual available magnetic field can only be determined once the device is made and the magnetic fields are measured. However, to get an idea of what size magnet that might be needed for an initial start a static model will be applied. Although the systems under study are affected by vibrations the frequency of these vibrations are much less than the frequency at which the magnetic field responds to changes.

Magnetic fields developed by a permanent magnet can be modeled by a number of methods. Two of which are a surface current model and the charge model. The surface current model assumes a current function that acts on the surface of the permanent magnet. This model stems from the principle that a wire carrying a current produces a magnetic field. The other model assumes that a charge density exists on each pole that results in a field akin to the magnetic field. Simplified versions of the models assume that the magnets act in free space, that is, not in contact with anything else and

that the gap is air. Assuming a current model, the expression that describes the magnetic field is found to be

$$B(\mathbf{x}) = \frac{\mu}{4\pi}\int \frac{J(\mathbf{x}')\times(\mathbf{x}-\mathbf{x}')}{|\mathbf{x}-\mathbf{x}'|^3} dV' \tag{2.7}$$

where **x'** represents the location of the source, **x** represents the target, *J(***x'***)* represents the surface current, *dV'* represents the volume of the source, and μ is the permeability of the target [21]. To determine the force from the resulting field, the Lorentz equation for the force developed by the current flowing through a conductor can be restated for the surface current model as

$$\mathbf{F} = \int_V \mathbf{J}_m \times \mathbf{B}_{ext}\, dv + \oint_S \mathbf{j}_m \times \mathbf{B}_{ext}\, ds \tag{2.8}$$

where *V* and *S* represent the volume and surface respectively [21].

Applying equations (2.7) and (2.8) to a cylindrical magnet is quite common and solutions are readily available. One such solution is [22]

$$B(x) = \frac{B_r}{2}\left[\frac{L+x}{\sqrt{R^2+(L+x)^2}} - \frac{x}{\sqrt{R^2+x^2}}\right] \tag{2.9}$$

where *L* is the length of the magnet, *R* is the radius of the magnet, B_r is the remanence of the magnet in *Gauss*, and *x* is the distance from the magnet to the target. The resulting force can then be expressed as

$$F = K\left(B(x)\right)^2 A \tag{2.10}$$

where *K* contains conversions and permeability factors, and *A* is the projected area of the magnet. A common value of *K* is 0.577 [22]. Equation (2.9) shows that the magnetic field declines as the target moves away from the magnet, and as long as *x* is less than *L*,

the trend will decrease in a parabolic fashion, and then equation (2.10) will amplify the decay rate as *x* increases. These results show that the magnet geometry plays a roll in the developed magnetic field, and that the force developed follows a second order polynomial trend. Figures 2.12 and 2.13 show the results of equations (2.9) and (2.10) with figure 2.13 illustrating the nearly linear relationship that the fields generated for "small" gap changes, and also shows the targeted gap range for the developed gap sensor. Figures 2.12 and 2.3 are based upon a cylindrical magnet about 0.31 in.(7.87 mm) in diameter, 0.125 in.(3.17 mm) in length, with a B_r of 11 kG. The actual response that may be observed in the actual system may differ significantly as the above model assumes that the magnet is neither in contact nor in the vicinity of any other material that may influence the magnetic field.

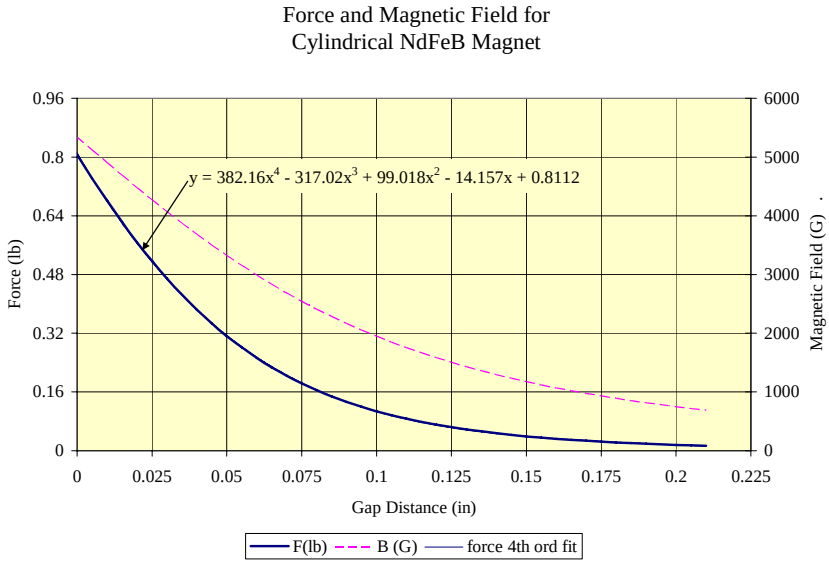

Figure 2.12 Magnetic Field and Developed Force over a Large Gap.

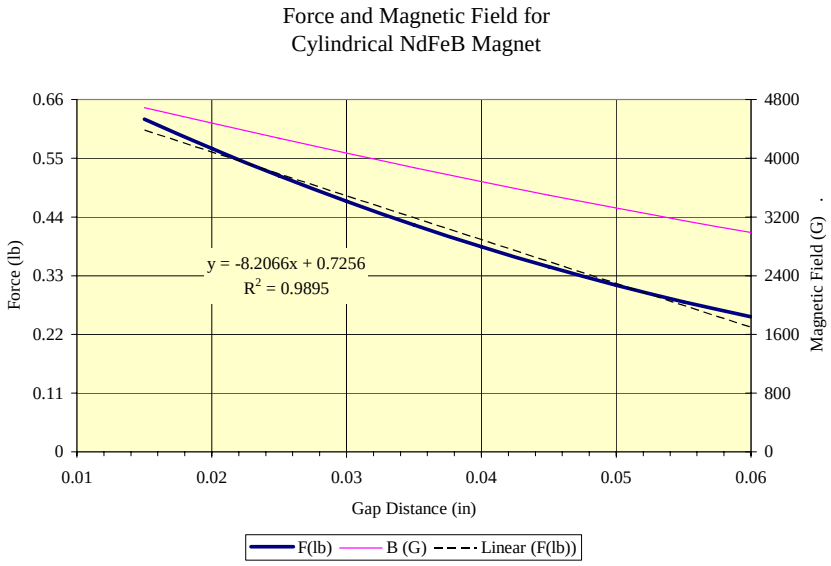

Figure 2.13 Magnetic Field and Developed Force over a Small Gap.

The type of material that the target is made of will determine the magnitude of the static force of attraction, if any. If the target surface is of ferrous nature, i.e. steel, then there will be a force of attraction. This force is dependent on the gap distance, the permanence, and the area of the magnet tip. This expression is non-linear for large changes in gap, but for small gap motions, the force of attraction is nearly linear. A non-ferrous target, i.e. aluminum or brass, will not generate a force of attraction under static conditions. Some non-ferrous targets can generate field a when traversing a magnetic field that would result in a force between the sensor and the target [23]. However, investigation of this phenomenon on sensor response will be left for future exploration.

The selection of a permanent magnet for an application requires knowledge of a number operating parameters. Four parameters to consider when narrowing down the selection are temperature, magnetic remanence, coercivity, and maximum potential [24].

The connection that these three parameters have is in regards to the demagnetization of the magnet. There is a temperature called the *Curie Temperature (T_C)* where the magnetization of the permanent magnet diminishes. The magnetic remanence, B_r, is a measure of the potential magnetic field that exists within the magnet when no external magnetizing field is applied. The coercivity, H_C, is the required external field to fully demagnetize a magnet. The maximum potential, $(BH)_{max}$, is a measure of the overall maximum available energy that is available for that magnet. Other factors that would eventually need to be considered are cost and manufacturing needs. The above factors need to be considered when the time comes to explore in future works and for industrial applications.

2.4 FFPI Theory

The FFPI consists of two dielectric mirrors embedded in a mono mode optical fiber. The mirrors are made of a thin film of TiO_2 deposited on the ends of two fibers that are then spliced together such that a length of fiber separates the two-coated surfaces thus forming the interferometer [25]. This type of construction is referred to as an intrinsic interferometer. Extrinsic interferometers separate the mirrors by an air gap. Laser light, typically in the near infrared wavelength region, around $\lambda=1310\ nm$, is pumped down the fiber and is reflected off of the two mirrored surfaces. Figure 2.14 shows a schematic of the interferometer and the path of the lights. The FFPI is an amplitude splitting interferometer as the initial wave that strikes the first mirror is divided into two wave fronts, one that reflects off the mirror surface, and one wave that is transmitted through the mirror. The light striking the second mirror has a similar

amplitude splitting affect resulting in the second reflective wave to pass through the first mirror and combining with the wave initially reflected off of the first mirror. The two combined wave travels back along the fiber for monitoring. As the gap between the mirrors changes, the power of the returned light due to the two reflections changes accordingly. This allows for a relationship to be established between the phase, or power of the laser light, to the relative change between the two mirrors and this allows for the FFPI to be applied as a strain sensor. That is, if there is a force acting on the FFPI system, a displacement relationship can be obtained.

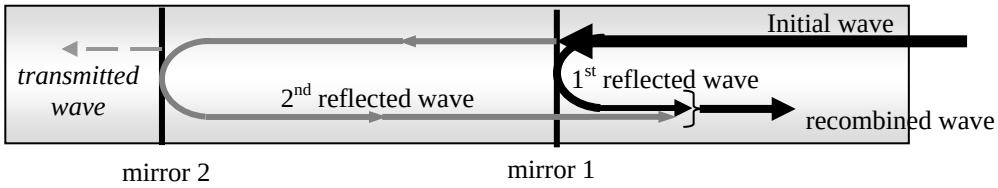

Figure 2.14 FFPI Optical Path Model

The mechanics relating the change in mirror gap to change in phase of the two recombined waves is determined by looking at two relationships. The first relationship arises from the fact that the recombined wave is a summation of two coherent beams of light and that the phase difference between them is defined by

$$\Phi = \frac{4\pi n}{\lambda} \Delta L \tag{2.11}$$

where n is the index of refraction, λ is the wavelength of the laser light, Φ is the change in phase, and ΔL is the change in mirror gap [26, 27]. The change in Φ is cyclic and related to a 2π cycle. Since each cycle, in theory, should show the same response the FFPI provides a relative change in gap as opposed to an absolute change in gap. The second relationship is if the strain is known, it will allow for the determination of the change in phase. This relationship results from the fact that as a fiber is stretched axially, it causes a dilation of the diameter [26], which influences the index of refraction. This phenomenon is presented by the following expression,

$$\Phi = \frac{4\pi nL\varepsilon}{\lambda}\left\{1 - 0.5n^2\left[P_{12} - \nu\left(P_{11} + P_{12}\right)\right]\right\} \tag{2.12}$$

where P_{ij}-*strain optic coefficient for the fiber*

υ-*Poisson's ratio for the fiber*.

Equation (2.11) represents the change in phase due to the change in path while (2.12) represents what happens mechanically.

2.4.1 Additional FFPI Relationship

The method by which the mirror gap is monitored requires that the laser be driven such that an optimal quadrature point is detected. The laser ramp adjusts the wavelength output of the laser which causes the observed wave to cycle through a series of maximum and minimum power levels. The quadrature point is the point on the resulting fringe plot that has the highest linearity and happens to coincide with the midway point of one of the sine waves. Figure 2.15 shows an example of the laser ramp and resulting fringe trace. The monitoring system, or signal conditioning unit, used for

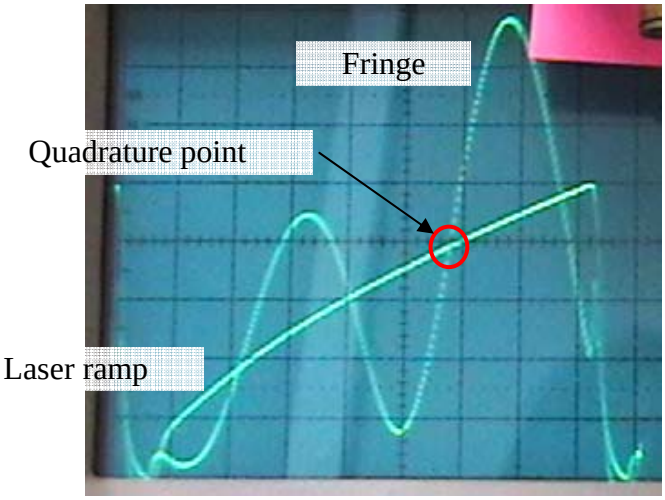

Figure 2.15 Fringe Trace on Oscilloscope

this study has a signal processing system that results in the following relation between phase change and voltage

$$\%\Phi = 100\frac{\Phi}{2\pi} = \frac{F/C}{0.2}V \qquad (2.13)$$

or,

$$\Phi = \frac{F/C(2\pi)}{20}V \tag{2.14}$$

where *F/C* is the ratio of the full-scale (*F)* setting to the calibration (*C*) setting of the SCU, and *V* is the monitored voltage. The above expression is based on the full scale output of 10 volts if operating in a uni-polar mode, or ±5 volts if operated in a bi-polar mode. The relative change in mirror gap, ΔL, is related to the strain developed within the mandrel, or hypo-tube, and will be discussed further in Section 3. The assumption made here is that the FFPI is bonded to the hypo-tube through a thin film of adhesive. This allows for the assumption that the strain loss across the adhesive layer is minimized. This assumption is similar to the assumption made when bonding foil strain gages to the test specimen.

2.5 Summary

Sensors that are used to monitor vibration are composed of four main elements, a proof mass, stiffness, damper, and a relative motion transducer. A sensor that is configured to monitor vibrations without contacting the body requires a means to react to the motion over an air gap. Permanent magnets can provide a means to allow a non-contacting vibration sensor to act over the gap and can be configured to provide a stiffness element for a seismic based contacting vibration sensor. The FFPI due to its fiber optic construction can provide a non-intrusive means to monitor the response generated by each type of sensor to some external excitation. An added benefit of using the FFPI is that the magnetic field generated by the magnets will not influence the laser

light. Section 3 will show how knowledge presented, such as the non-linear force to gap change relation for a permanent magnet, can be employed to generate expressions that will provide insight as to expected responses for the proposed gap and seismic vibration sensors.

3 RELATIONS TO DESCRIBE THE RESPONSE OF THE SENSORS

3.1 Introduction

The following discussion will present how the relationships presented in Section 2 along with some additional analysis can provide some insight into how the developed sensors will most likely respond. The most significant difference between the motion relations presented in Section 2 and those to be developed in Section 3 is the non-linear contribution of the forces developed by the permanent magnets. The discussion will also demonstrate relationships that will be instrumental in establishing the type of calibration tests to conduct and for verifying the results from the calibration tests. The sensors will be introduced by first presenting the construction of each sensor. The discussion for the relationships that define performance operation of the FFPI embedded within the hypo-tube will be presented within the FOGS section and it applies to both sensors, and then the force curves for an oscillatory motion for the permanent magnets can be modeled, and lastly, how the response of the sensor under discussion can be modeled and how those results can be interpreted.

3.2 Fiber Optic Gap Sensor (FOGS)

The first generation of non-contact vibration sensor that was developed was constructed with the intent of having a minimal number of elements. The intent was to fabricate a sensor which would allow for the housing of the sensor head and support of the hypo-tube (mandrel). Figure 2.11 shows a cross-section of such a construction. The

following will discuss the characteristics of the sensor construction and formulation of the response characteristics.

The Fiber Optic Gap Sensor (FOGS) consists of five parts. The parts consist of 1) the magnet/sensor head, 2) the hypo-tube containing the FFPI, 3) the anchor cap, 4) the housing, and 5) the permanent magnet. Figure 3.1 shows the key components and the completed assembly.

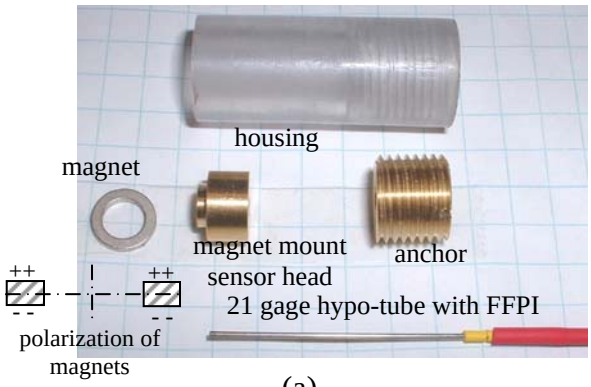

(a)

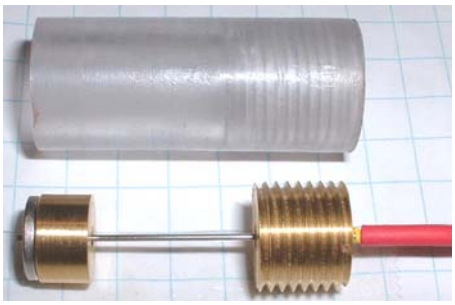

(b)

(c)

FOGS assembly. (a) key components, (b) assembled (c) Final assembly

Figure 3.1 Fiber Optic Gap Sensor (FOGS) Assembly

The magnet utilized was a NdFeB ring magnet that was leftover from a previous project. The magnetization of the magnet is such that the plane faces are in opposite polarity, that is, one face is “North”(++) and the other face is “South”(--), figure 3.1. The magnet is about 0.3125 in.(7.11 mm) in diameter with the inner diameter of 0.28 in.(1.65 mm), and a thickness of 0.065 in. (0.254 mm). The sensor head is made from brass and machined so that it would accommodate the magnet. There is about 0.007 in.(0.178 mm) that protrudes beyond the magnet to prevent the magnet from directly impacting any targets as this could cause some demagnetization of the magnet and could fracture the magnet as these magnets are essentially ceramics and are quite brittle. This protrusion also needs to be accounted for when setting the gap between the target and sensor head for calibration purposes. The hypo-tube houses the FFPI and provides a means to provide transverse and axial support of the FFPI. The tube utilized here was a 21 gauge stainless steel tubing (outer diameter of 0.032 in. (0.813 mm), inner diameter of 0.020 in.(0.508 mm)). This size of tubing was readily available and provides ample axial sensitivity for the sensor. The selection of the mandrel/tubing is a compromise between axial sensitivity and lateral resistance. That is, it is desired to optimize the axial sensitivity of the mandrel, but minimize the sensitivity to any lateral excitation. But, as a prototype, and in an effort to minimize fabrication issues, the focus of construction was on axial sensitivity. Stainless-steel is not necessarily the optimal material for this type of application primarily because it is rather susceptible to thermal growth. Also, the modulus of elasticity of stainless steel is rather high and that decreases the sensitivity too. This will be discussed further in section 3.4.1. The sensor head is designed to slide

within the housing and its length is long enough, in theory, to minimize bending of the hypo-tube. The tooling used to machine the components was not maintained on a regular basis and maintaining tight tolerances, particularly angular, was difficult. Also, the parts of the sensors were machined by the author who has a novice level of machining skills. The sensor head and the anchor point are adhered to the hypo-tube using a cyanoacrylate adhesive, i.e. super glue. The space between the sensor head and anchor point could be filled with a material such as silicone to reduce the chance of the hypo-tube to experience any bending or lateral flexing. This was not done as it was desired to observe how the bare minimum for the sensor elements responded. Additional configurations and tests will be discussed in Section 6.

The placement of the fiber within the hypo-tube is critical in that it is desired that only the portion of the fiber between the mirrors should experience the primary loading. Common practice is to allow about 0.375 to 0.5 inches (9.52 to 12.7 mm) of strain relief prior to the first mirror to reduce the chance of the exiting fiber to introduce any effect on the first mirror. The hypo-tube extends through the anchor point and extends approximately 0.4 in. (10 mm) beyond the anchor point. The mirror gap of the FFPI is 0.5 in. (12 mm) which is a standard size and matches the reference interferometer within the signal conditioning unit (SCU*)* that is used to monitor the FFPI. Figure 3.2 shows the relative position of the two mirrors and the area of strain relief. Shorter mirror spacings are possible, but would require a corresponding reference gage in the SCU. By decreasing the mirror spacing, a more compact sensor could be developed.

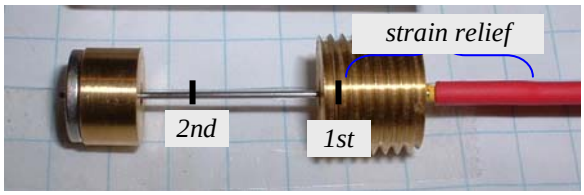

Relative mirror spacing

Figure 3.2 Relative Mirror Gap Spacing for FOGS

3.3 FOGS Response

The FOGS sensor construction consists of a sensing mass to which the permanent magnet is attached to and a hypo-tube that connects the sensing mass to the housing. During operation, the housing is not attached to the object to be monitored and it is assumed that the housing does not move. The gap between the sensing head and the vibrating body results in a force acting on the sensor head that is assumed to vary in a periodic fashion. Figure 3.3 shows the physical arrangement as well as representative models.

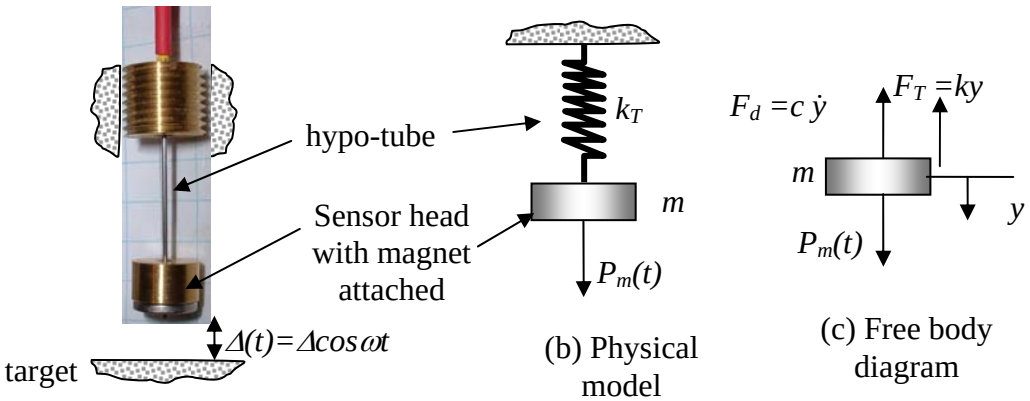

(a) Actual configuration with housing removed

(b) Physical model

(c) Free body diagram

Figure 3.3 FOGS Operational Model

The response of the FOGS sensor can be described as one due to a periodic forced excitation. This response initially starts out in a different fashion than what was described in Section 2 for the typical vibration sensor model, but the end result is a response similar to the accelerometer model. The free-body diagram in figure 3.3(c) shows the magnetic force $P_m(t)$ acting on the sensor head and the resulting equation of motion is stated as

$$m\ddot{y} + c\dot{y} + k_T y = P_m(t) \tag{3.1}$$

The damping force, F_d, is assumed to be of a linear damping form. The magnetic force is non-linear and can be described by a summation of higher order sine waves, or

$$\begin{aligned} P_m(t) &= P_1\Delta\cos(\omega t) + P_2\Delta^2\cos(2\omega t) + P_3\Delta^3\cos(3\omega t) \\ P_m(t) &= \sum_{i=1}^{3} P_i\Delta^i\cos(i\omega t) \end{aligned} \tag{3.2}$$

The development of equation (3.2) is presented in section 3.5. The actual gap change, $\Delta(t)$, is the relative gap change and not the absolute gap. That is, the actual gap span can be expressed by

$$X(t) = X_0 + \Delta(t) \tag{3.3}$$

where X_0 is the initial gap setting between the sensor head and the target. The total force acting on the sensor head consists of a static portion and a dynamic portion, or

$$P_m(X) = P_m(X_0 + \Delta(t)) = P_m(X_0 + \Delta\cos\omega t) = P_m(X_0) + P_m(\Delta\cos\omega t) \tag{3.4}$$

From a dynamic standpoint, the constant magnetic force, $P_m(X_0)$, cancels out as this essentially causes a preload on the hypo tube, ky_0, and the two forces cancel each other out, leaving the dynamic portion. The equation of motion is a linear differential

equation and the fact that the excitation force is series of higher harmonics allows for a superposition of solutions. That is, the equation of motion can be restated as

$$m\ddot{y} + c\dot{y} + k_T y = P_i \cos \omega_i t \tag{3.5}$$

The equation of motion can be restated to include natural frequency, $\omega_n = \sqrt{k_T / m}$ and damping terms $2\zeta\omega_n = c/m$ as

$$\ddot{y} + 2\zeta\omega_n \dot{y} + \omega_n{}^2 y = \frac{P_i}{m} \cos \omega_i t \tag{3.6}$$

Assuming that the response is steady state and of the form of the excitation the resulting response can be expressed as

$$y = \frac{P_i}{k_T} \frac{1}{\sqrt{\left(1 - r_i^2\right)^2 + 4\zeta r_i^2}} \tag{3.7}$$

where $r_i = \omega_i / \omega_n$. The phase response is then found to be

$$\tan \phi = \frac{2\zeta r_i}{1 - r_i^2} \tag{3.8}$$

Equation (3.7) can be restated to relate the input force, P_i, to the response force, yk_T, as

$$F\left(r_i\right) = \frac{yk_T}{P_i} = \frac{1}{\sqrt{\left(1 - r_i^2\right)^2 + 4\zeta^2 r_i^2}} \tag{3.9}$$

The quantity in the numerator, yk_T, represents the force developed within the hypo tube while P_i represents the magnitude of the force applied on the sensing mass due to the magnetic force resulting from the gap change. Assuming that the primary excitation

frequency is below the natural frequency of the FOGS, or $r<<1$, the resulting response shown in equation (3.9) reduces to

$$\frac{yk_T}{P_i} \approx 1 \tag{3.10}$$

and the resulting phase reduces to

$$\tan\phi \approx 0 \rightarrow \phi \approx 0^0 \tag{3.11}$$

These results indicate that the FOGS sensor will respond directly in synch with the change in the gap. Figures 3.4 and 3.5 show the resulting trends for two damping factor cases. The role of damping in this case is that the lower the damping factor, the broader the phase response is. That is, low damping will extend the range for which the response of the FOGS will be in phase with the excitation. The overall response plots shows that for a 4% difference between the force on the FOGS and the force developed in the gap provides an operational r of 0.2. This can be used to define the dynamic range of the sensor, $f_{\max} = 0.2 f_n$ where f_{max} is the maximum excitation frequency and f_n is the natural frequency in Hz. Increasing damping would expand the possible range of operation, but the resulting phase error could make implementation not practical. The above analysis resembles the response described in Section 2 for the accelerometer model. The primary difference between this analysis and that analysis is that the accelerometer is in direct contact with the body in question and the response relates the relative change in position of the proof mass, while for the FOGS, the response relates the applied force to the force developed in the hypo tube. Additionally, unlike an accelerometer, the FOGS sensor does provide information at a zero excitation frequency.

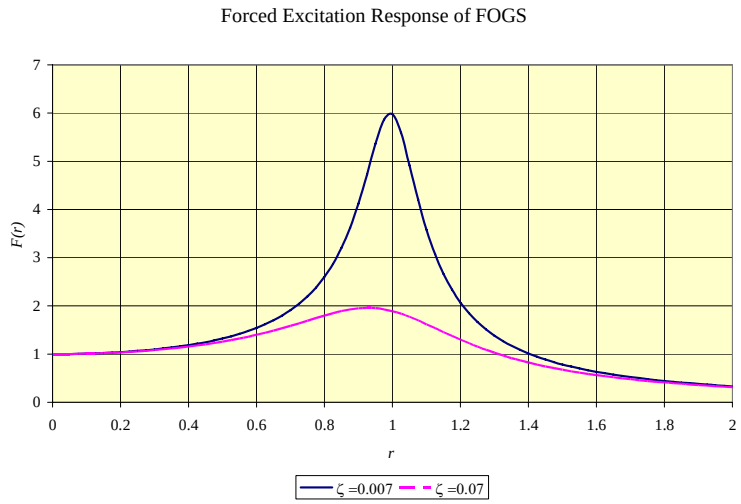

Figure 3.4 FOGS Forced Excitation Response

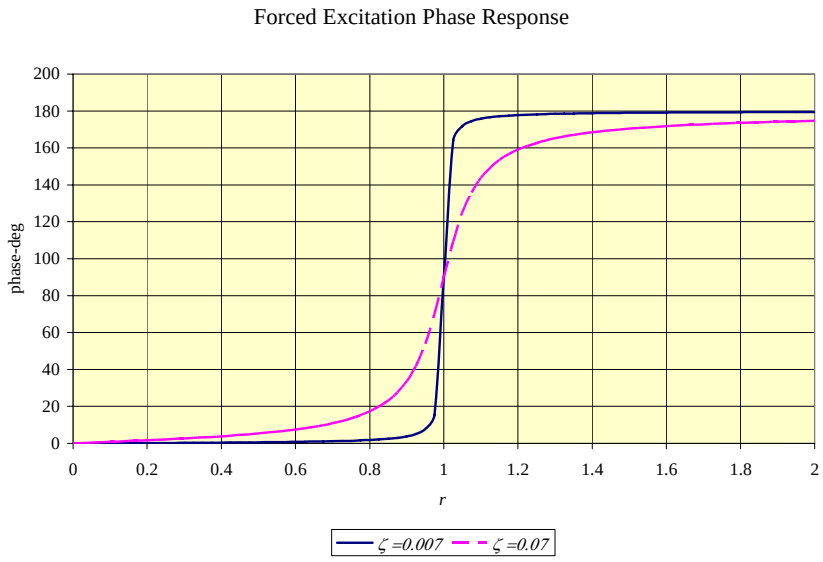

Figure 3.5 FOGS Phase Response

3.4 FFPI and Mandrel Relationships

The FFPI is constructed by stripping away the protective polyimide coating leaving the cladding and glass core exposed. This results in a segment of the fiber to be brittle. To protect this core, as well as to limit birefringence from side to side motion and kinking, it is common to embed the FFPI into a mandrel. The mandrel incorporated

for the developed sensors was hypodermic tubing, or hypo-tube. It is worth noting that it is possible to recoat the exposed fiber core with polyimide which would restore a large majority of the original strength and robustness of the original fiber. At the time of this research, a recoating system was not available. The bonding of the FFPI to the mandrel is similar to the bonding of foil strain gages in that the response of the gage is assumed to mirror that of the test specimen providing the bonding layer is thin. To be able to relate the change in the FFPI due to the applied loading on the mandrel, or hypo-tube, it is necessary to develop relationships expressing the loading of the hypo-tube to its physical characteristics such as material and geometry.

3.4.1 Hypo-tube Relationships

The response of the hypo-tube to the load applied due to the pull of the permanent magnet can be expressed through Hooke's law. Hooke's law relates the stress developed in a body to the developed strain and material properties. Assuming the hypo-tube under goes a purely axial tensile loading, the stress strain relation that can be applied is

$$E = \frac{\sigma}{\varepsilon} = \frac{PL}{A(\Delta L)} \tag{3.12}$$

where, P is the applied load, A is the cross-sectional area of the tube, L is the mirror gap, E is the modulus of elasticity of the hypo-tube, and ΔL is the gap change between the mirrors. Equation (3.12) can be rearranged as follows

$$\Delta L = \frac{L}{EA} P \tag{3.13}$$

Equation (3.13) relates the applied load to the relative stretch of the tube which then can be related to the phase change, or observed voltage, of the FFPI. The deformations that occur here is strictly within the elastic region of the tube. To define an upper limit of allowable load, two yield conditions need to be applied. The first is that the tube can experience a maximum load before the elastic region is overshot. This can be defined by

$$\sigma_{YP} = \frac{P}{A} \rightarrow P_{YP} = \sigma_{YP} A \tag{3.14}$$

where σ_{YP} is the yield stress for the hypo-tube and P_{YP} is the resulting yield load. The second parameter that needs to be observed is the maximum strain and stress that the FFPI can withstand. The strength of the interferometer is fairly high 40 kpsi (275.8 MPa), but the ductility is low. The allowable strain for typically bare fiber is 0.5 to 1.5%.

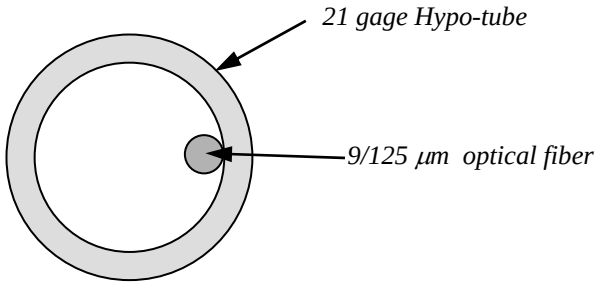

Figure 3.6 Relative Size of Optical Fiber to Hypo-tube

The assumption that the loading of the FFPI within the hypo-tube experiences solely a uni-axial loading is a bit of a stretch as there are a number of sources as to why this wouldn't occur. Three sources are 1) fiber not parallel to hypo tube as fiber is up to

one fourth the inner diameter of the tube, figure 3.6, 2) load applied is off-center to hypo-tube, and 3) machining and stack tolerance errors could create misalignment. To further expand the load to mirror gap change, a combined state of stress model that includes uni-axial loading and moment loading can developed as follows

$$\sigma = \frac{P}{A} + \frac{Mc}{I} \tag{3.15}$$

where M is the applied moment, c is the distance the axis of the tube to the point of interest, and I is the polar area moment of inertia of the hypo-tube, figure 3.7. The applied moment can be stated as

$$M = \pm eP \tag{3.16}$$

where e is the eccentricity of the applied load P from the center axis of the hypo-tube. This allows equation (3.15) to be restated as

$$\sigma = \left(\frac{1}{A} + \frac{\pm ec}{I} \right) P \tag{3.17}$$

Figure 3.7 shows the relative location and trends that equation (3.17) is based upon

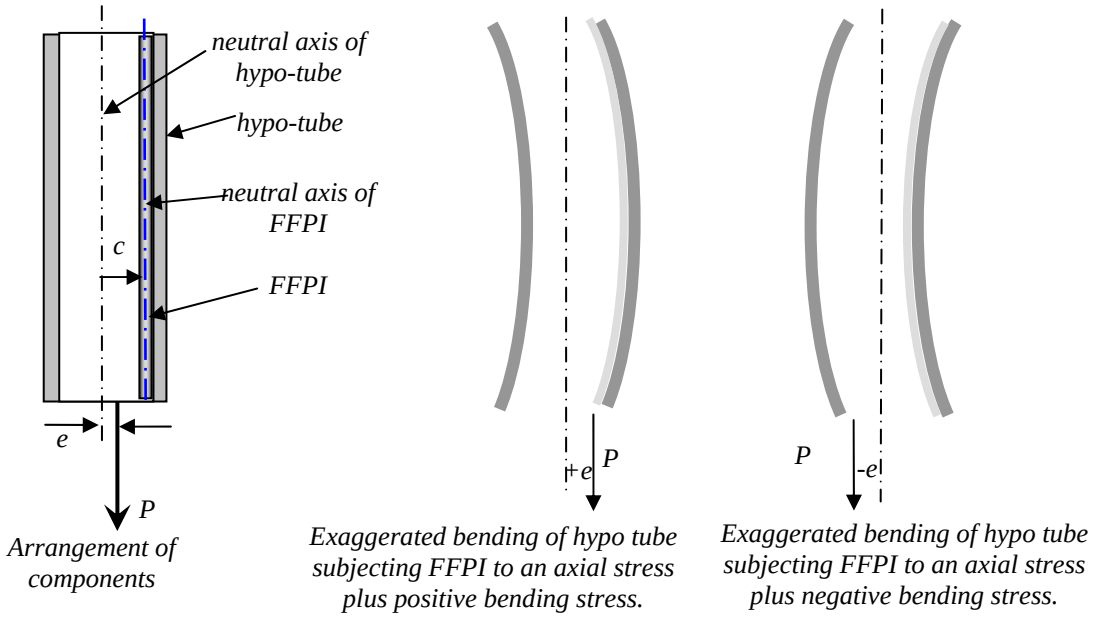

Figure 3.7 FOGS and Hypo-tube Relations

.Equations, 2.12, and 2.13 can be combined that will allow for the determination of the input load P to the output signal V. The obtained relation is

$$P = \left(\frac{E}{L}\right)\left(\frac{AI}{I \pm ecA}\right)\left(\frac{\lambda}{2n}\right)\left(\frac{F/C}{20}\right)V \tag{3.18}$$

For convenience, it is reasonable to take c as the radius of the inner diameter of the hypo-tube partly because the difference would be about the radius of the optical fiber, about 2.5 mils (63.5 μm), and it is difficult to know exactly where the fiber is within the tube. Equation (3.18) can be further reduced by letting the values before the voltage, V, be replaced by

$$R = \left(\frac{E}{L}\right)\left(\frac{AI}{I \pm ecA}\right)\left(\frac{\lambda}{2n}\right)\left(\frac{F/C}{20}\right) \tag{3.19}$$

This relation is limited to use with the signal conditioning unit (SCU*)*, but could easily be modified to provide an insight into the expected fringe for a given load for other detecting schemes.

3.5 Probe Response to a Variable Gap Change

The force that acts on the sensor head of the FOGS probe results from a change in the gap between the sensor head and target. Assuming that the system is a stiff system, the force applied to the sensor head is directly transferred to the FFPI embedded with the hypo-tube. The objective here is to determine what form the motion to be measured takes once transformed by the magnetic force. The ideal force relationship to apply for the magnetic force developed for a given gap change would be a linear relationship. However, this cannot be counted on so a fourth order polynomial can be assumed as a worse case scenario. The application of fourth order polynomial was selected as preliminary measurements resulted in a good fit, coefficient of determination of 0.99. Responses resulting from a fourth order polynomial can be easily reduced down to a first order response if the results permit this. Again, understanding how the force response over time will reflect the measurand is necessary as this will allow for a proper study and correction of the resulting time waveform and corresponding frequency response plots.

First, let the force generated by a magnet in proximity of a target be described by a fourth order polynomial

$$f\left(x\right) = Ax^4 + Bx^3 + Cx^2 + Dx + E \tag{3.20}$$

where *A, B, C, D,* and *E* are coefficients that are determined from a best curve fit algorithm. The 4th order polynomial, again, is a worst case scenario. If the curve fit can be done by applying a 2nd or 3rd order polynomial the following development applies by setting the appropriate coefficients, *A* or *B,* to zero. Next, the motion about a gap will be assumed to take the following form

$$X(t) = X_0 + \Delta \sin \omega t \tag{3.21}$$

where X_0 is the initial gap setting, Δ is the 0-Pk change in gap, ω is the angular rate of change of the gap. Substituting equation (3.21) into equation (3.20) and collecting terms yields the following

$$\begin{aligned} F(X + \Delta \sin \omega t) = F(X_0) &+ \left[4AX_0{}^3 + 3BX_0{}^2 + 2CX_0 + D\right]\Delta \sin \omega t \\ &+ \left[6AX_0{}^2 + 3BX_0 + C\right]\Delta^2 \sin^2 \omega t + \left[4AX_0 + B\right]\Delta^3 \sin^3 \omega t \\ &+ A\Delta^4 \sin^4 \omega t \end{aligned} \tag{3.22}$$

Equation (3.22) can be further reduced by applying multiple angle identities to the sine terms and also observing that the coefficients of the sine terms are successive derivatives of the original function observed in equation (3.20), or,

$$\begin{aligned} F(X_0 + \Delta \sin \omega t) &= \bar{A} + \bar{B} \sin \omega t + \bar{C} \cos 2\omega t + \bar{D} \sin 3\omega t + \bar{E} \cos 4\omega t \\ \bar{A} &= F(X_0) + \frac{1}{4} F'(X_0)\Delta^2 + \frac{1}{64} F''''(X_0)\Delta^4 \\ \bar{B} &= F'(X_0)\Delta + \frac{1}{8}\left[F'''(X_0)\right]\Delta^3 \\ \bar{C} &= \frac{-1}{4} F''(X_0)\Delta^2 - \frac{1}{48} F''''(X_0)\Delta^4 \\ \bar{D} &= \frac{-1}{24} F'''(X_0)\Delta^3 \\ \bar{E} &= \frac{1}{192} F''''(X_0)\Delta^4 \end{aligned} \tag{3.23}$$

Equation (3.23) indicates that the resulting response of the sensor head would exhibit contributions of two, three, and even four times the primary excitation frequency. This is a concern as an ideal sensor construction should result in reproducing the original signal without generating any additional harmonics. This is important as there are monitoring situations where tracking higher order harmonics is necessary to identify particular phenomena. The results shown in eq. (3.23) are a result of the magnetic force acting over the gap as if there was a nonlinear hardening spring acting between the sensor head and the target surface. Figure 3.8 is an exemplar case of the force versus gap response as the relative change in force as the gap is increased from 30 to 80 mils (0.762 to 2.03 mm). The use of the fourth order fit could be required as the actual response may not necessarily follow the curves depicted in Section 2, figure 2.12, due to possible sticktion, flux leakage, non-parallel faces, and assembly issues. Figure 3.8

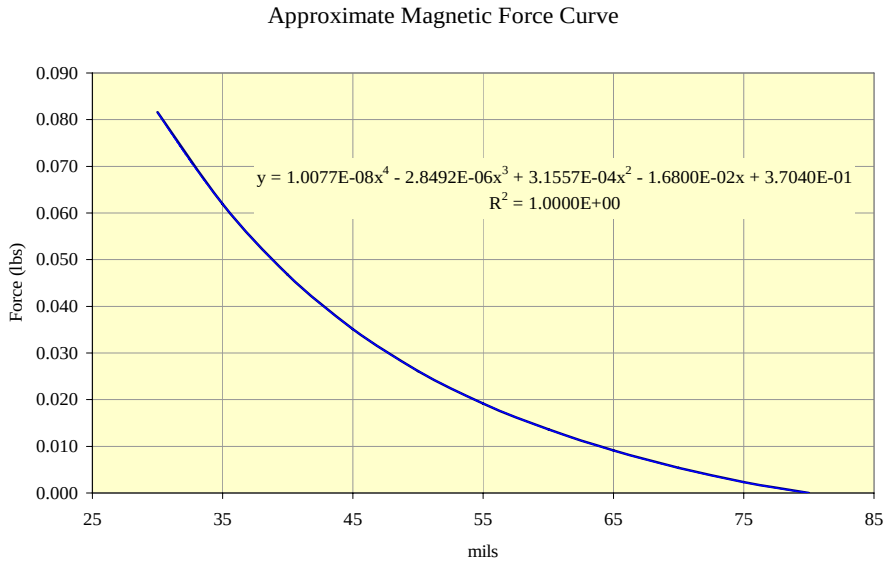

Figure 3.8 Relative Change in Force for a 30 to 80 mil Change in Gap

shows that the difference in force from an 80 mil (2 mm) gap to a 30 mil (0.76 mm) gap is about 0.081 lb (0.361 N), that is, because the force reading at 80 mils is zero does not mean that the force acting on the sensor head is zero. The coefficients from the polynomial displayed in figure 3.8 can be used to determine the relative contribution of the higher harmonics over the shown gap range. Taking a nominal gap of 40 mils (1.02 mm) with a 0-peak (0-Pk) change in gap of 4 mils (0.102 mm) and solving for the barred coefficients shown in eq. (3.23), a relative measure of response can be obtained by looking at a power comparison, or,

$$dB_i = 20\log\left(\frac{\bar{i}}{\bar{B}}\right) \qquad i = \bar{C}, \bar{D}, \bar{E} \tag{3.24}$$

The power *dB* measure is employed as it is desired to look at the relative contribution of each higher harmonic to the principle harmonic in the spectrum of the time waveform. Figure 3.9 shows the results. Table 3-1 shows a comparison of the contributions by approximating a mean *dB* level for the three cases shown based on eqs (3.23) and (3.24) by assuming a 40 mil (1.02 mm) gap with a 0-Pk value of 4 mils (0.102 mm). The far

Table 3-1 Harmonic Contribution Comparison
Assumed gap: 40 mils, 0-Pk: 4 mils

Harmonic	Coefficient	dB	% of $\bar{B}$
2nd	$\bar{C}$	-25	5.5
3rd	$\bar{D}$	-55	0.2
4th	$\bar{E}$	-85	0.005

right column of Table 3-1 indicates that the 2nd harmonic component can be up to 5.5% of the amplitude of the primary harmonic component while the other two components are much less and could be masked by noise in actual data.

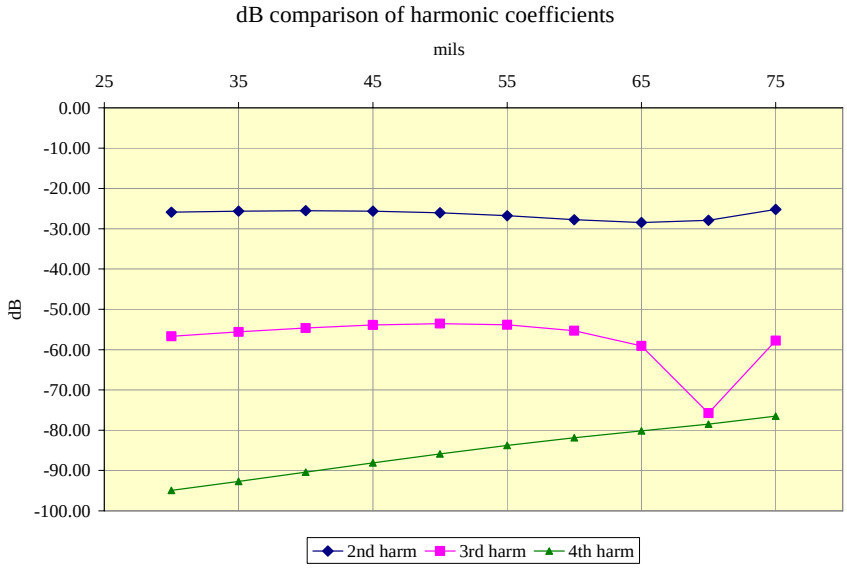

Figure 3.9 Relative *dB* for Super Harmonic Force Components

The resulting time waveform of eq. (3.23) when the values from figure 3.8 are applied to an initial 40 mil (1.02 mm) gap with a 0-Pk gap change of 4 mil (0.102 mm) is shown in figure 3.10. The resulting trend at first appears as a smooth sine wave. However, closer inspection shows that the valleys appear to be more rounded than the peaks. This can be explained as that the valleys coincide with an increase in gap, and hence, a lower force acting on the sensor head, while the peaks correspond to a gap decrease which corresponds to a higher force acting on the sensor head. This further demonstrates the non-linear nature that arises when applying the permanent magnet. Figure 3.11 shows a comparison of the valleys and peaks. Two observations from figure

3.11 are that the peaks are not of equal amplitude, and that the peak response occurs at the same time.

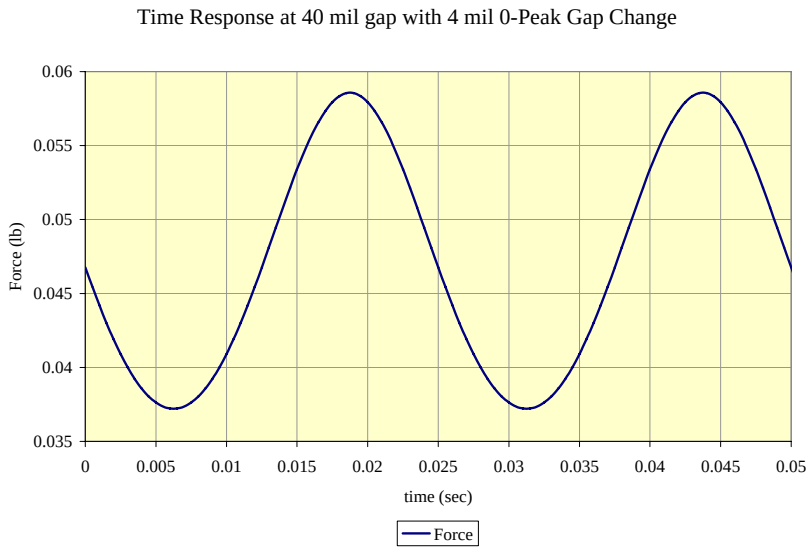

Figure 3.10 Resultant Force Gap Response

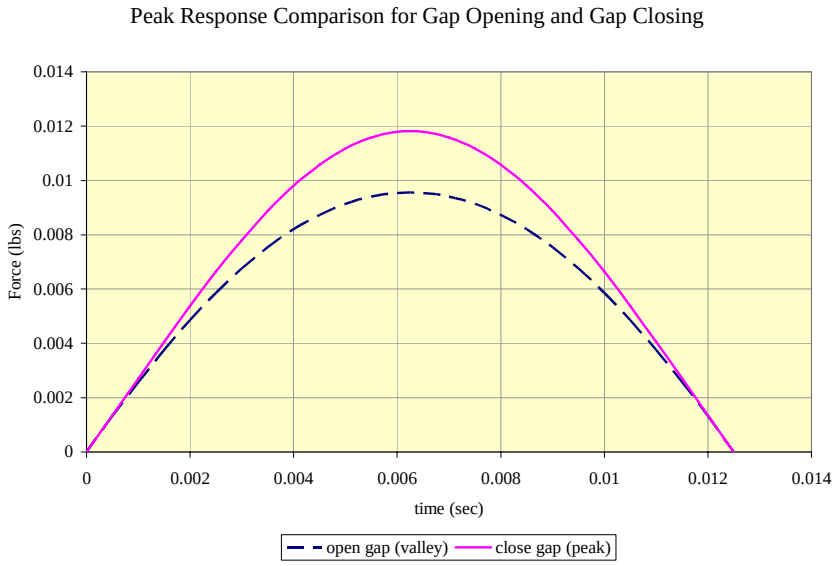

Figure 3.11 Peak and Valley Comparison

Applying a Fourier transform to the time waveform will provide an indication as to the relative contribution of the higher harmonics that were previously discussed. Figure 3.12a displays the Fourier transform in a linear plot and figure 3.12b shows the spectrum in a semi-log plot so that the higher harmonics are more pronounced. The first three harmonics are apparent in figure 3.9b, but the 4^{th} harmonic is not clearly defined. The resulting *dB* between the first harmonic and the 2^{nd} and 3^{rd} are -25.7 and -56.4 *dB,* respectively. These values are comparable to those shown in table 3-1. The results provide insight into what form data could take as tests are conducted to determine the performance of the FOGS probe. Although the responses shown are not ideal from an application point of view, they do provide insight as to how the sensor can be expected to behave.

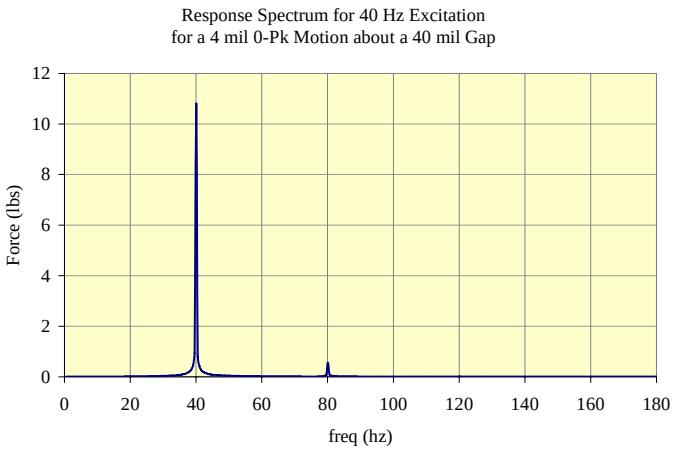

(a) Linear plot

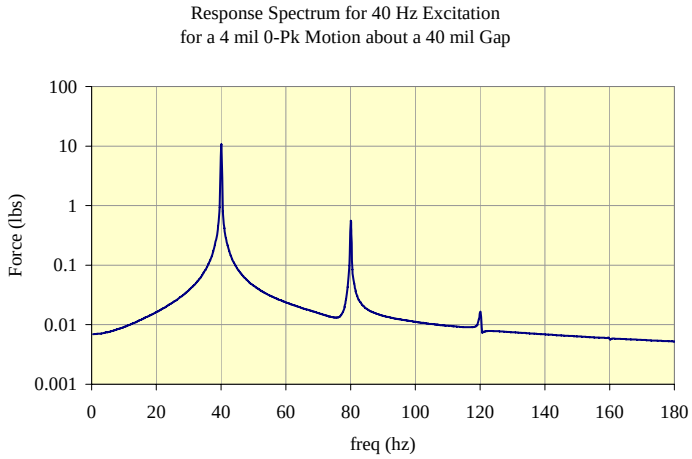

(b) Semi-log plot

Figure 3.12 Fourier Transform of Time Waveform of Fig 3.10

Recalling that there is a direct relation between the measured voltage from monitoring the FFPI due to the applied force, equation (3.18), allows the user to apply a monitoring scheme, figure 3.13, where the obtained signal would be fed through an

inverse relation, or anti-calibration curve, that relates *volts* to *gap*, figure 3.14 and figure 3.15. A strategy that can be employed to exploit these results are as follows:

1) Set gap for FOGS probe and reset SCU to zero (reset quadrature point).
2) Determine the nominal gap voltage from polynomial from figure 3.14, V_{X0}.
3) Calculate the augmented gap voltage by $V_A = V_{X0} + V_{read}$, where V_{read} is the FOGS output voltage from the SCU.
4) Determine the resulting gap value by use of polynomial from Figure 3.15, $G(V_A)$.

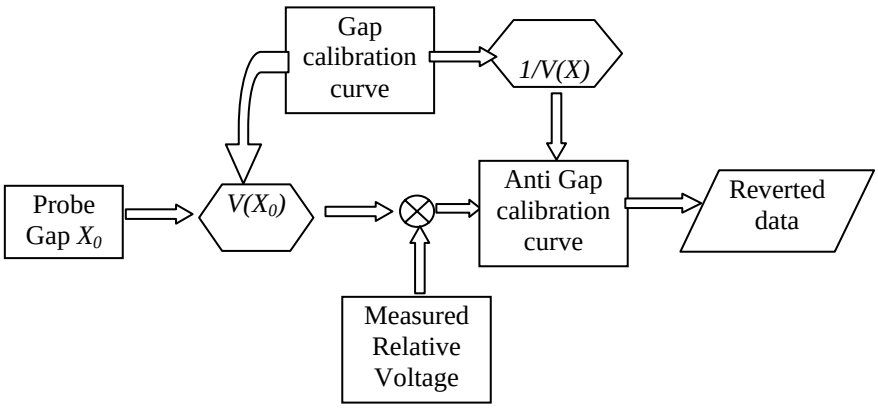

Figure 3.13 Data Collection Scheme for the FOGS

The procedure shown in figure 3.13 would allow for the user to monitor the gap without having to correct for the change in slope and it would also provide a means to remove the nonlinear distortion of the signal which results in the generation of higher harmonics that may not be present in the measurand. The gap setting used could be dictated by the

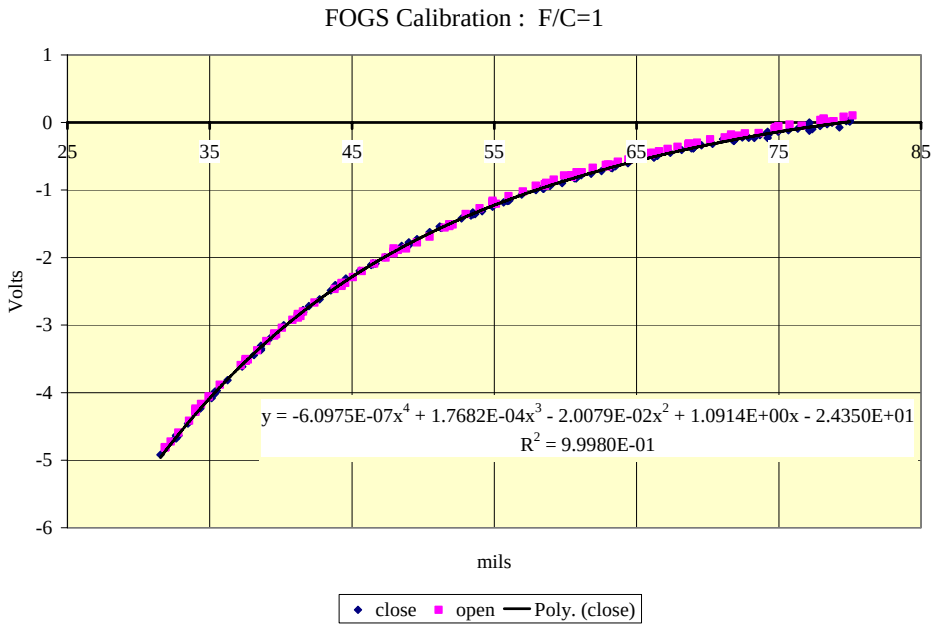

Figure 3.14 FOGS Volt Response for Gap Change

sensitivity required. Figure 3.16 shows the sensitivity in volts/mils and the corresponding minimum mil measurement. The sensitivity is a plot of the first derivative of the calibration curve shown in figure 3.15. The minimum mil measurement is based on the minimum voltage that can be observed on a system that has a 12 byte processor on a 10 volt full range.

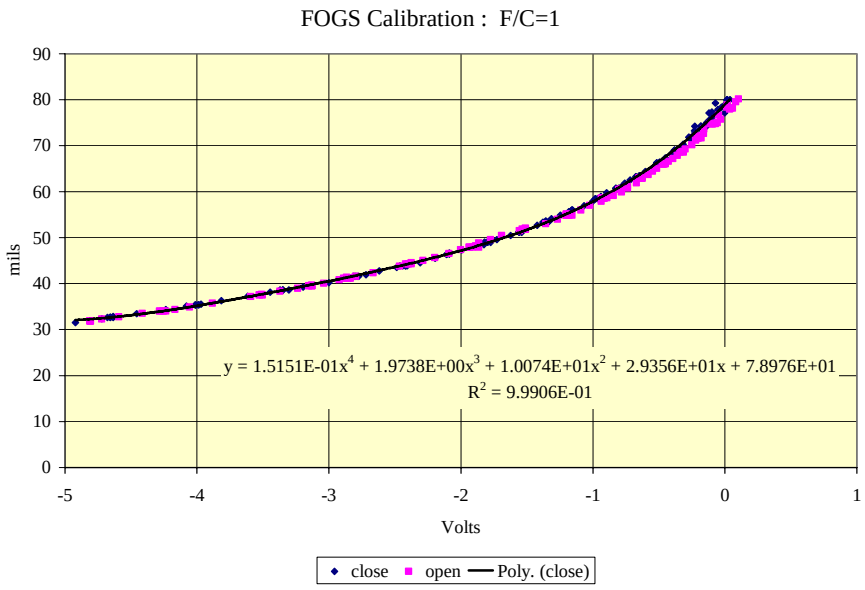

Figure 3.15 FOGS Inverse Volt Response for Gap Change

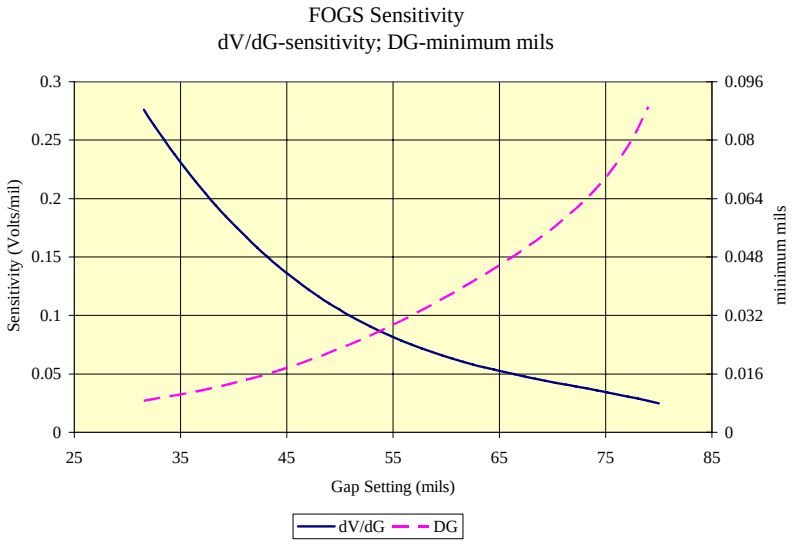

Figure 3.16 FOGS Sensitivity

3.6 Fiber Optic Vibration Sensor (FOVS)

The next item to discuss is the development of the contacting vibration sensor. The intent was to develop a sensor that responds as a seismic system. The permanent magnets would be used to float the proof mass and the FFPI would be used to monitor the response between the proof mass and the sensor head. The general configuration of the sensor will be presented and then expanded response models will be developed.

The fiber optic vibration sensor (FOVS) is composed of six main parts. The parts are: 1) the proof mass, 2) sensor head, 3) cap, 4) hypo-tube (FFPI), 5) permanent magnets, and 6) the housing. Figure 3.17 shows the key components and the completed assembly. The FOVS is assembled by placing the magnets on each end of the proof mass and magnets in opposite pole on the sensor head and cap. The cap, proof mass, and sensor head are bored so that the hypo-tube containing the FFPI passes through. The bore through the proof mass is larger than the hypo-tube so that it can slide freely along the hypo tube. The bores on the sensor head and cap are closer to the hypo-tube outer diameter so that alignment is maintained. The clearance between the outer diameter of the proof mass and the inner diameter of the housing is less than the clearance between the hypo-tube and the bore of the proof mass. This is done so as to prevent the proof mass from striking the hypo-tube if the proof mass was to experience side to side motion. The desired clearance between the sensor head and housing is such

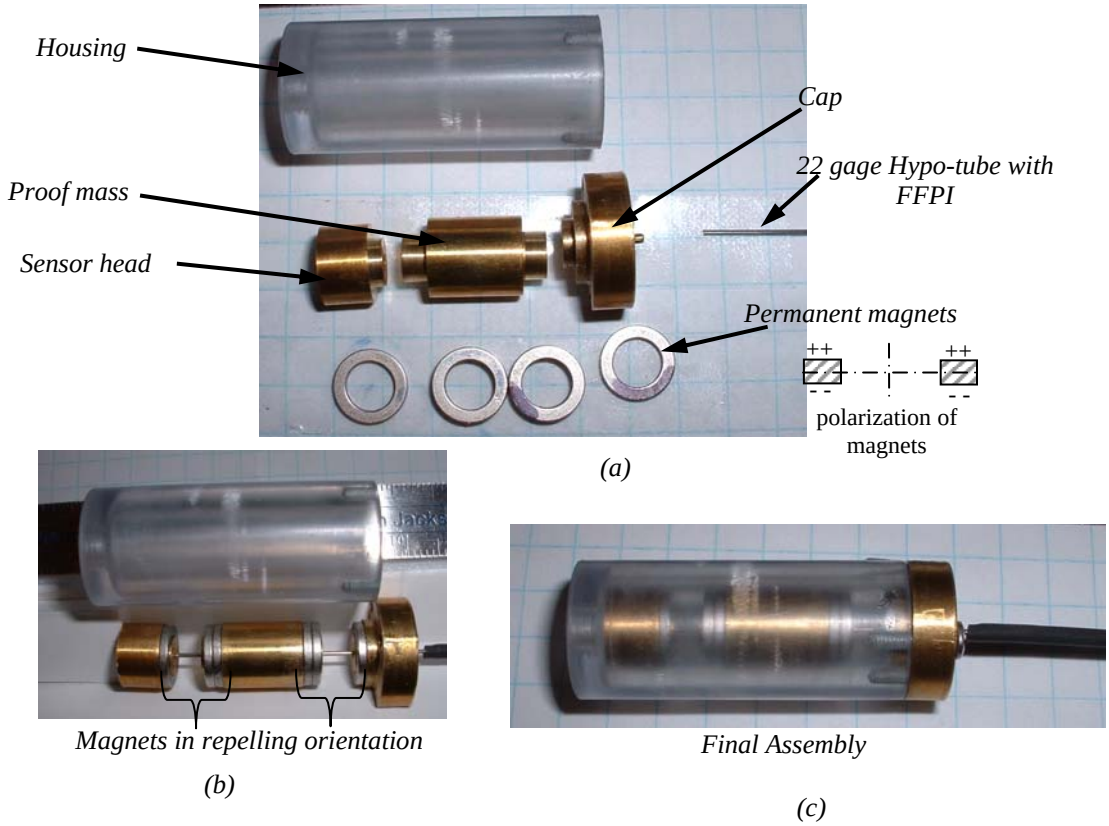

FOVS assembly. (a) primary components, (b) components relations, (c) final assembly.

Figure 3.17 Fiber Optic Vibration Sensor Components

that the sensor head can slide freely, but not allowed to pivot about its length much like the sensor head arrangement used on the FOGS. To minimize the potential for pivoting, the length of the sensor head is greater than the diameter of the tube by 1.25. The hypo-tube is adhered to the sensor head and cap by the use of cyanoacrylate. As in the case of the FOGS construction, the 1st mirror is near to the cap and the strain relief zone extends through the cap ends about ¼ inch beyond the cap. The permanent magnets that were utilized, again, are ones that were leftover from a previous project.

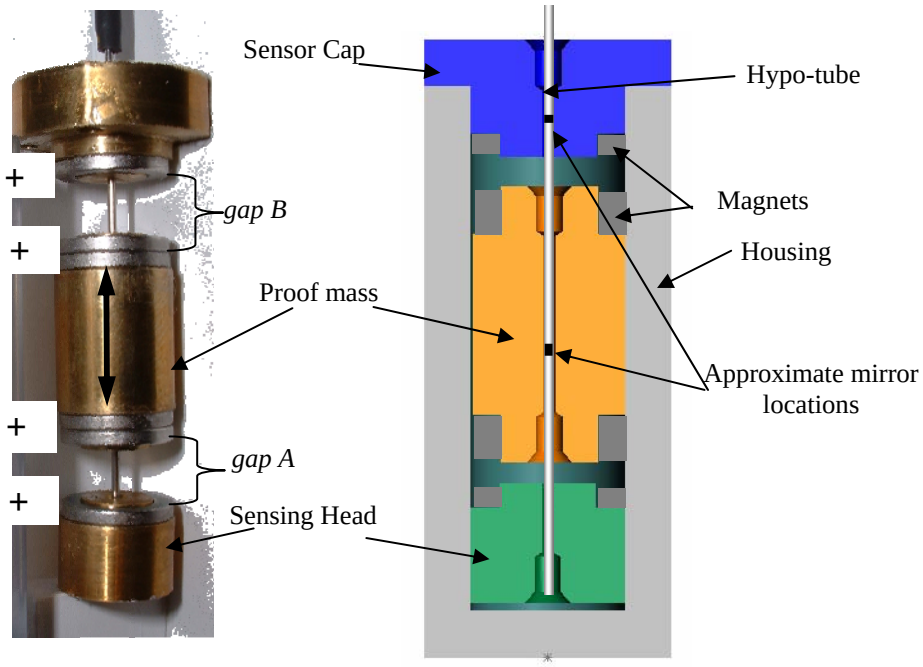

Figure 3.18 FOVS Repelling Mode

The magnets are oriented such that the poles repel one another which results in a spring effect to be generated between the proof mass and the sensor head as well as the cap. The basic operation of the FOVS is that the housing transmits the excitation source to the cap, which in turn, transmits the motion through the hypo-tube to the sensor head. Then the sensor head affects gap *A* in figure 3.18 resulting in a force to act against the proof mass. The proof mass responds which again affects the overall force developed across gap *A*. This results in an oscillatory change in gap *A* which in turn results in the hypo-tube experiencing an oscillatory loading that acts on the FFPI within the tube. A body that is suspended by a repelling magnet field has six degrees of freedom and is inherently unstable. The design intent here was to allow for two degrees of motion,

namely axial motion along the hypo-tube and rotation about the hypo-tube. Radial translation would be restricted as well as tilting of the proof mass. The effectiveness is dependent on the tolerances of manufacturing. The model that better represents how the FOVS will respond is similar to that presented in Section 2. The key difference in this model is that the spring elements are no longer linear due to the non-linear nature of the force between the opposing faces as the gap changes.

The development of the model that reflects the response of the sensors proof mass will assume that the force acting on each face of the proof mass are modeled by the same force polynomial, damping force is proportional to velocity, and that the initial gap on each side are the same. Also, the stiffness of the hypo-tube is orders of magnitude greater than the "magnetic" stiffness, so any changes in gap *A* due to the elongation of the hypo-tube will be neglected. Figure 3.19 shows the kinematic and resulting free body diagram for the system. The equation of motion for this system takes on the form of

$$m\ddot{Y} = F_A\left(G_A\right) - F_B\left(G_B\right) \tag{3.25}$$

Note that damping is neglected in this model as the final expression will be non-linear and the key objective here is to establish an idea as to what the natural frequency of the system will be. Damping in the form of a viscous damping can be included as a first cut approximation if a more refined model or a numerical solution is to be obtained.

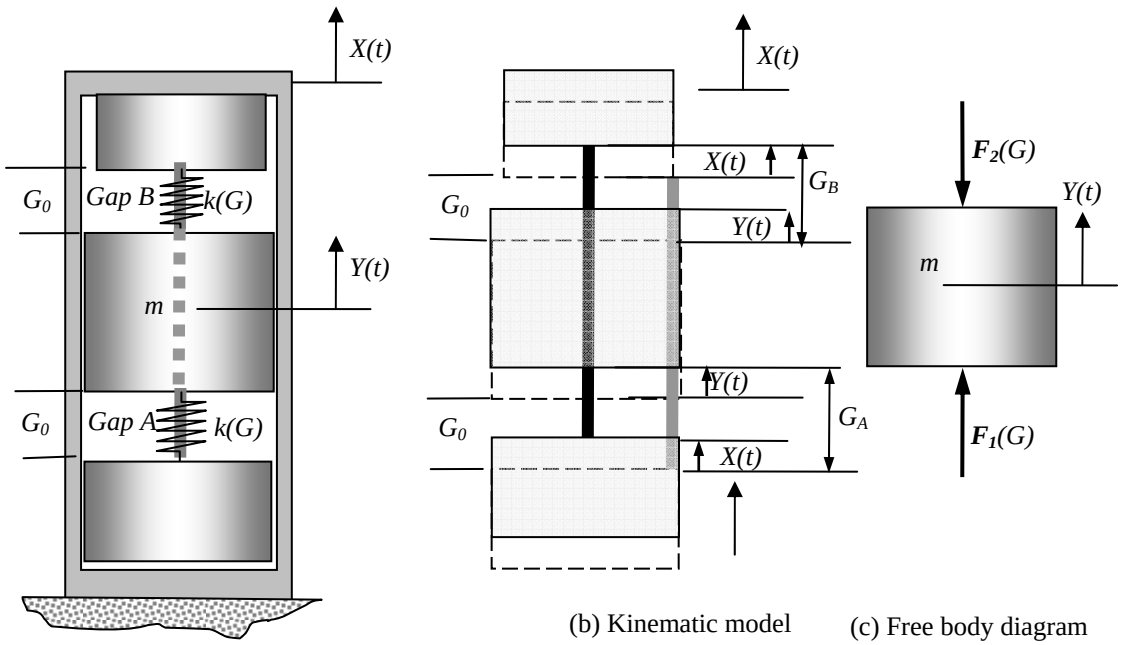

(a) Element model (b) Kinematic model (c) Free body diagram

Figure 3.19 FOVS Models

The forces developed by the magnetic "springs" F_1 and F_2 can be expressed by a 3rd order polynomial, or,

$$F_m(G) = AG^3 + BG^2 + CG \tag{3.26}$$

where G is the gap size. A higher order polynomial such as the one developed for the FOGS can be implemented if required. The resulting gap changes due to the housing motion and proof mass motion can be expressed by

$$\begin{aligned} G_B &= G_0 + X - Y \\ G_A &= G_0 - X + Y \end{aligned} \tag{3.27}$$

where G_0 is the initial gap, X is the excitation, and Y is the motion of the proof mass. Defining the relative gap change as $\Delta = X - Y$ allows for equation (3.27) to be restated as

$$\begin{aligned} G_B &= G_0 + \Delta \\ G_A &= G_0 - \Delta \end{aligned} \tag{3.28}$$

Substituting equation (3.28) into equation (3.26) will yield the spring forces

$$F_m\left(G_0 \pm \Delta\right) = F\left(G_0\right) \pm A\Delta^3 + \left(3AG_0 + B\right)\Delta^2 \pm \left(3AG_0{}^2 + 2BG_0 + C\right)\Delta \tag{3.29}$$

The right hand side of equation (3.25) can be expressed as

$$F_1\left(G_A\right) - F_2\left(G_B\right) = 2A\Delta^3 + 2\left(3AG_0{}^2 + 2BG_0 + C\right)\Delta \tag{3.30}$$

Also, applying time derivatives to equations (3.27) and (3.28) will yield the following

$$\ddot{\Delta} = \ddot{X} - \ddot{Y} \rightarrow \ddot{Y} = \ddot{X} - \ddot{\Delta} \tag{3.31}$$

Substituting equation (3.31) and(3.30) into (3.25) yields

$$m\ddot{\Delta} + 2A\Delta^3 + 2\left(3AG_0{}^2 + 2BG_0 + C\right)\Delta = m\ddot{X} \tag{3.32}$$

which is the equation of motion for the system. The form that equation (3.32) takes is recognized as the Duffing oscillator. Inspection of the Δ coefficients of equation (3.32) show that they are functions of the first and third derivatives of equation (3.26), or,

$$\begin{aligned} K_1 &= \frac{dF\left(G_0\right)}{dG} = 3A\left(G_0\right)^2 + 2B\left(G_0\right) + C \\ K_3 &= \frac{d^3F\left(G_0\right)}{dG^3} = 6A \end{aligned} \tag{3.33}$$

This allows for equation (3.32) to be restated as

$$m\ddot{\Delta} + \frac{K_3}{3}\Delta^3 + 2K_1\Delta = m\ddot{X} \tag{3.34}$$

Dividing through by the proof mass, *m*, yields

$$\ddot{\Delta} + \left(\frac{K_3}{3m}\right)\Delta^3 + \left(\frac{2K_1}{m}\right)\Delta = \ddot{X} \tag{3.35}$$

The cubic Δ term in equation (3.35) makes the resulting equation of motion non-linear and obtaining an exact solution is not as convenient as for the linear equation of motion presented in Section 2. A further extension of the equation of motion can be made by assuming that the excitation is a single harmonic excitation, or,

$$\begin{aligned} X &= X_0 \sin(\omega t) \\ \ddot{X} &= -\omega^2 X_0 \sin(\omega t) \end{aligned} \tag{3.36}$$

where ω is the excitation frequency, X_0 is the excitation amplitude. Then, eq. (3.35) can be restated as

$$\ddot{\Delta} + \left(\frac{K_3}{3m}\right)\Delta^3 + \left(\frac{2K_1}{m}\right)\Delta = -\omega^2 X_0 \sin(\omega t) \tag{3.37}$$

To include damping, a linear viscous damping relation can be assumed as a first cut approximation and the equation of motion can then be further expanded to

$$\ddot{\Delta} + \frac{c}{m}\dot{\Delta} + \left(\frac{K_3}{3m}\right)\Delta^3 + \left(\frac{2K_1}{m}\right)\Delta = -\omega^2 X_0 \sin(\omega t) \tag{3.38}$$

The resulting expression can then be solved via numerical analysis methods to obtain an overall system response. Approximate solutions to equation (3.38) can be obtained by applying the bi-harmonic method as an example. The key information that is desired from the analysis is what is the fundamental natural frequency of the system, how does the equation behave for a given range of excitation amplitudes, what influence does damping play, and is the linear damping assumption adequate. Another assessment of equation (3.38) would also provide insight as to how non-linear the response of the proof mass is. The strength or degree of nonlinearity is strongly dependent on the relative

change in gap size. And, the key objective is to determine what the response of the FFPI would be due to the resulting motion of the proof mass and the applied excitation. So, it is necessary to determine what the overall change in gap *A* is so that the force applied to the sensor head, and hence to the hypo-tube and FFPI can be determined.

An analytical means to determine the response of equation (3.38) can be accomplished by applying the method of iterations. This requires that an initial response is selected and that the coefficients of another assumed response are compared. First, equation (3.38) can be restated as

$$\ddot{\Delta} + 2\zeta\omega_n\dot{\Delta} + \beta\Delta^3 + \alpha\Delta = \Lambda_0 \sin(\omega t + \phi) \tag{3.39}$$

where $\beta = K_3/3m$, $\alpha = \omega_n{}^2 = 2K_1/m$, $2\zeta\omega_n = c/m$ and $\Lambda_0 = -\omega^2 X_0$. The phase term, ϕ, represents the fact that due to the damping, the response of the system and the force will fall between 0 and 180^0. A second modification splits the forcing term into two components, or,

$$\ddot{\Delta} + 2\zeta\omega_n\dot{\Delta} + \beta\Delta^3 + \alpha\Delta = A_0 \cos\omega t + B_0 \sin\omega t \tag{3.40}$$

where $\Lambda_0 = \sqrt{A_0{}^2 + B_0{}^2}$, and $\tan\varphi = B_0/A_0$. The next step is to assume a solution to the response as

$$\Delta = H \sin\omega t \tag{3.41}$$

and substituting it into equation (3.40). This results in the following after collecting like terms

$$\left[-H\omega^2 + \tfrac{3}{4}\beta H^3 + \alpha H\right]\sin\omega t + \left[2\zeta\omega_n H\omega\right]\cos\omega t - \frac{\beta H^3}{4}\cos 3\omega t = A_0\cos\omega t + B_0\sin\omega t \tag{3.42}$$

Equating the coefficients of the harmonic terms and neglecting the *cos3ωt*, yields the following

$$\begin{aligned} &\sin\omega t: \; -H\omega^2 + \tfrac{3}{4}\beta H^3 + \alpha H = B_0 \\ &\cos\omega t: \; 2\zeta\omega_n H\omega = A_0 \end{aligned} \tag{3.43}$$

or,

$$\left(\omega^2 X_0\right)^2 = \left[-H\omega^2 + \tfrac{3}{4}\beta H^3 + \alpha H\right]^2 + \left[2\zeta\omega_n H\omega\right]^2 \tag{3.44}$$

Note that if β is zero, equation (3.44) can be restated in the form of the response relation, equation 2.3, stated in Section 2. Solving for a relationship between *H* and X_0 cannot be done directly, so the equation is restated such that ω is the unknown. Assessing equation (3.44) can be done by solving for an expression in ω, the excitation frequency, for given values of *H*, the response, for fixed values of the excitation amplitude X_0, and the damping factor ζ and selecting only real value results. The form in which (3.44) takes is

$$\begin{aligned} &\left(H^2 - {X_0}^2\right)\left(\omega^2\right)^2 + \left(4\zeta^2{\omega_n}^2H^2 - 2\alpha H^2 - \frac{3}{2}\beta H^4\right)\omega^2 \\ &+\left(\alpha^2H^2 + \frac{9}{16}H^6 + \frac{3}{2}\alpha\beta H^3\right) = 0 \end{aligned} \tag{3.45}$$

which is a quadratic equation in terms of the excitation frequency ω. A plot of the response is shown in figure 3.20 for various excitation amplitudes utilizing α=3913.9, β=518645.5, and ω_n=199.7 rad/s. Figure 3.21 demonstrates the contrast in the phase

response between the linear model and the non-linear model. Figure 3.20 shows that as the excitation amplitude increases, the response "hump" tends to lean toward the right causing the range of frequency at which high amplitude responses can occur. The curve also indicates that there are points where the response of the sensor could experience a sudden jump in response as there are more than one response points at certain frequencies. The actual response of the proof mass of the sensor is limited by hard stops, so the amplitudes displayed would not necessarily occur. The figure demonstrating the phase does show that around the fundamental natural frequency, the phase can vary for various excitation frequencies, but, once above a certain amplitude, the phase is 180^0 out from the excitation which is similar to the linear response model. Also, from figure 3.20, it can be observed that once well above the unstable frequency, and with a suitable amount of damping, the non-linear response is equivalent to the linear model response and approaches a response ratio of one. The non-linear analysis

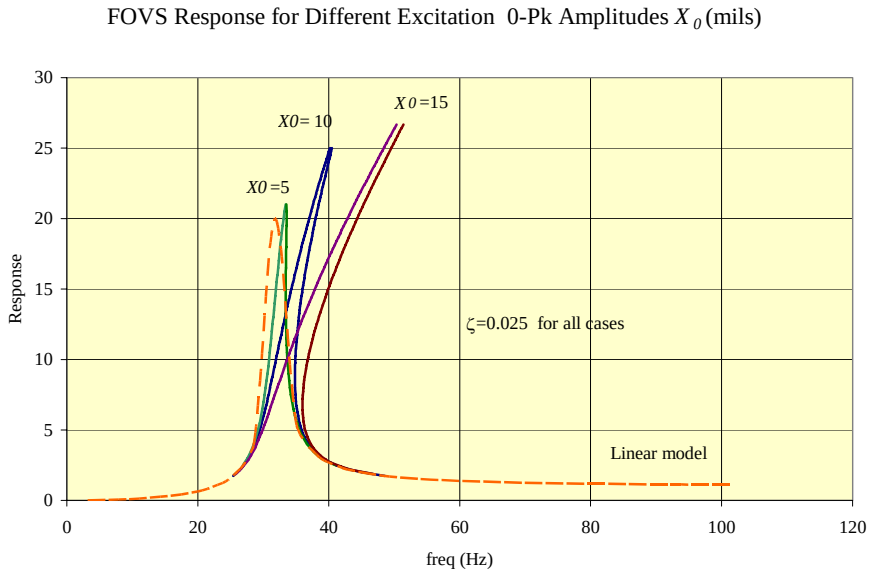

Figure 3.20 Non-Linear Response of FOVS Seismic Mass

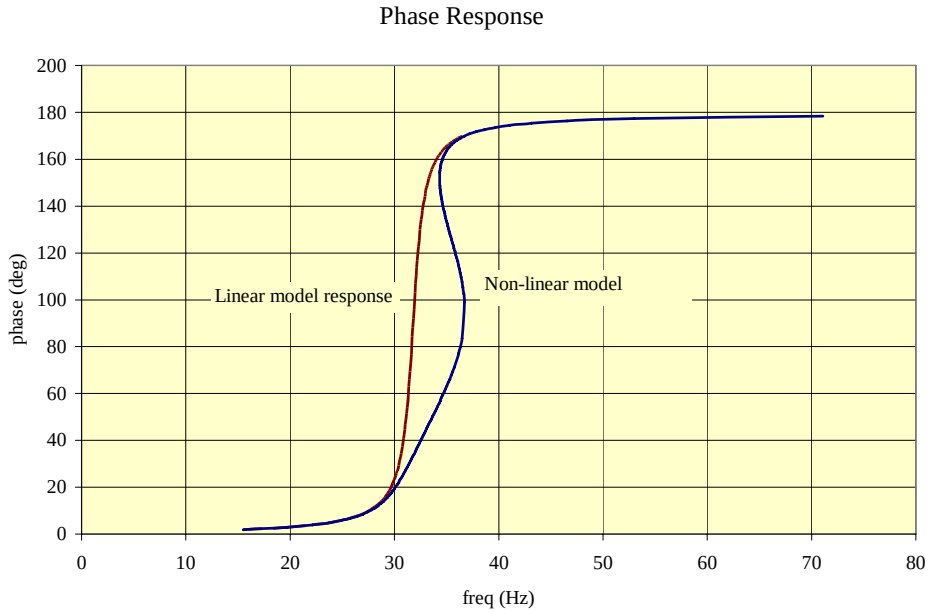

Figure 3.21 Comparison of Phase Response

shown does indicate that a non-linear model is only required if operation is required near the resonance frequency to account for the error in amplitude and for phase.

3.6.1 Assuming FOVS Output is Related to Acceleration Excitation

Assuming that the FOVS sensor output is related to acceleration it is necessary to obtain an expression that relates the response of the FOVS to the acceleration excitation. To obtain the relation, the analysis will pick up with equation(3.44). The expression on the left hand side of the equation represents the excitation source and will be replaced by g_P, which will represent some fractional value for the acceleration due to gravity. So, equation (3.44) can be restated as

$$\left(g_P\right)^2 = \left[-H\omega^2 + \tfrac{3}{4}\beta H^3 + \alpha H\right]^2 + \left[2\zeta\omega_n H\omega\right]^2 \qquad (3.46)$$

Again eq. (3.46) will be rearranged solving for an expression in terms of ω, the excitation frequency yielding

$$\begin{aligned}&\left(H^2\right)\left(\omega^2\right)^2+\left(4\zeta^2{\omega_n}^2H^2-2\alpha H^2-\frac{3}{2}\beta H^4\right)\omega^2\\&+\left(\alpha^2H^2+\frac{9}{16}H^6+\frac{3}{2}\alpha\beta H^3-{g_P}^2\right)=0\end{aligned}\tag{3.47}$$

Again, the strategy for solving the equation above is to assume a value for H and solve for the corresponding ω and keeping only the real solutions. This will result in a set of response plots similar to those obtained in Section 2 with the exception that the added cubic terms cause the response peak to lean to the right. Figure 3.22 demonstrates the resulting response for various g_p and ζ combinations. The observed discrepancy between the peak response frequencies for a given damping factor and excitation level, i.e. ζ=0.02 and g= 1, between figures can be attributed to the fact that the excitation value is a calculated value and the step used to increment through H, the response amplitude might be slightly different for each case. This results in the slight discrepancy between the peak response values of 37.36 *Hz* and 37.47 *Hz* observed in figure 3.22 (a) and (b) respectively.

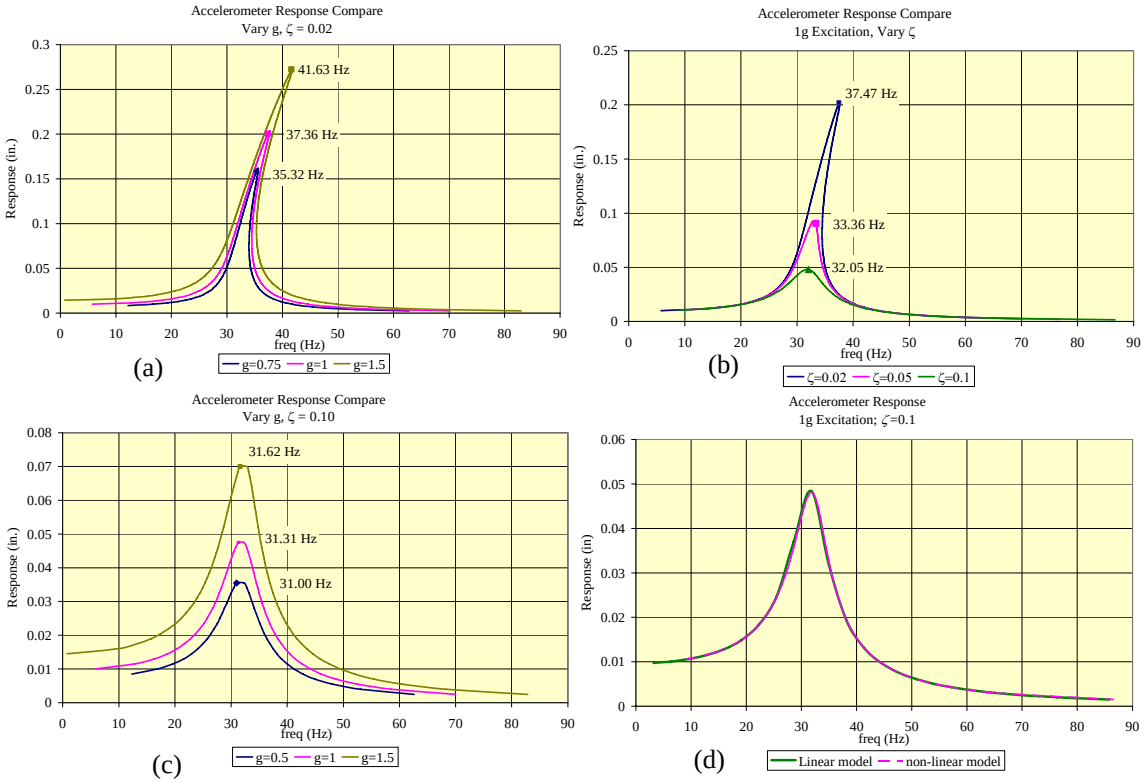

Figure 3.22 Non-linear Response to Acceleration Excitation

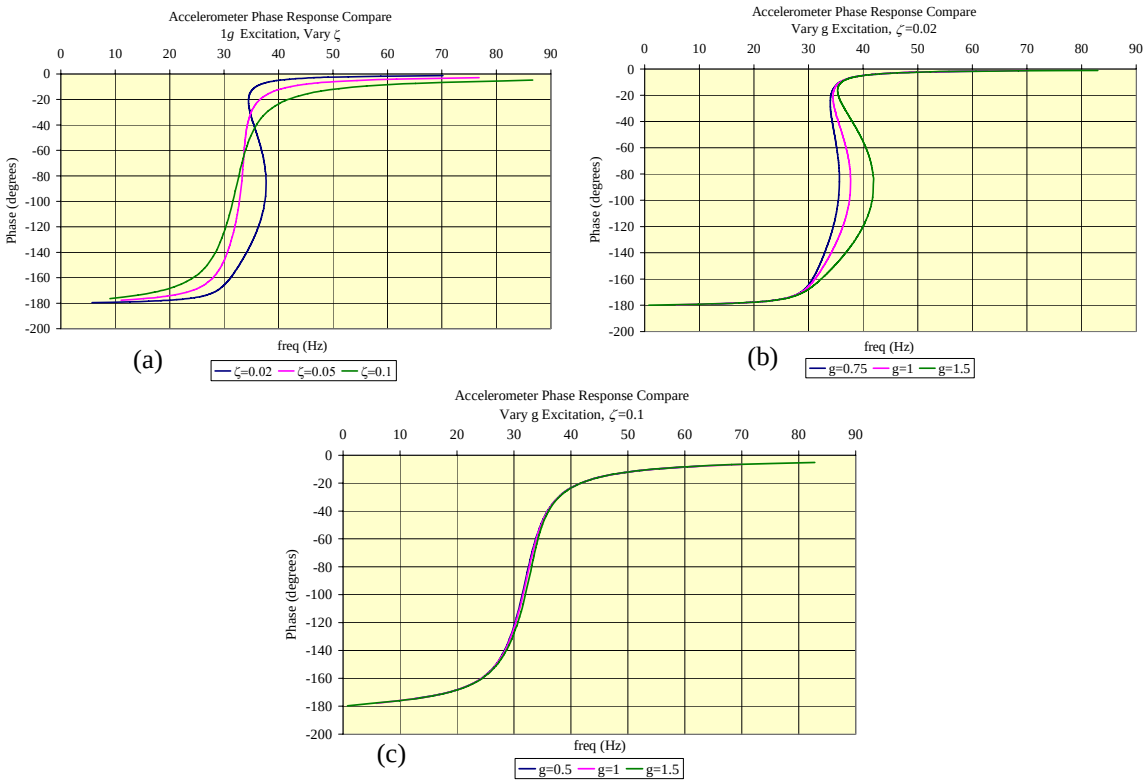

Figure 3.23 Non-linear Accelerometer Phase Response

3.6.2 Assuming FOVS Output is Related to Velocity Excitation

Although the response of the FOVS as a velocity based sensor is unlikely, it cannot be ruled out without investigating how the non-linear system might respond to a velocity based input. Again, equation (3.44) will be restated to reflect velocity, $v=X_0\omega$,

$$\left(\left(X_0\omega\right)\omega\right)^2 = \left(v_0\right)^2\omega^2 = \left[-H\omega^2 + \tfrac{3}{4}\beta H^3 + \alpha H\right]^2 + \left[2\zeta\omega_n H\omega\right]^2 \qquad (3.48)$$

Again, redefining equation (3.48) in terms of ω yields,

$$\begin{aligned}&\left(H^2\right)\left(\omega^2\right)^2 + \left(4\zeta^2\omega_n{}^2H^2 - 2\alpha H^2 - \frac{3}{2}\beta H^4 - v_0{}^2\right)\omega^2 \\ &+\left(\alpha^2H^2 + \frac{9}{16}H^6 + \frac{3}{2}\alpha\beta H^3\right) = 0\end{aligned} \qquad (3.49)$$

Figure 3.23 shows the response for a combination velocity excitation levels and ζ levels. Again, results of this analysis is that the response curves for the non-linear case do show the leaning of the response curves as observed for the seismometer and accelerometer response. Also, figures in 3.24 show the phase response and the influence of the damping ratio, ζ.

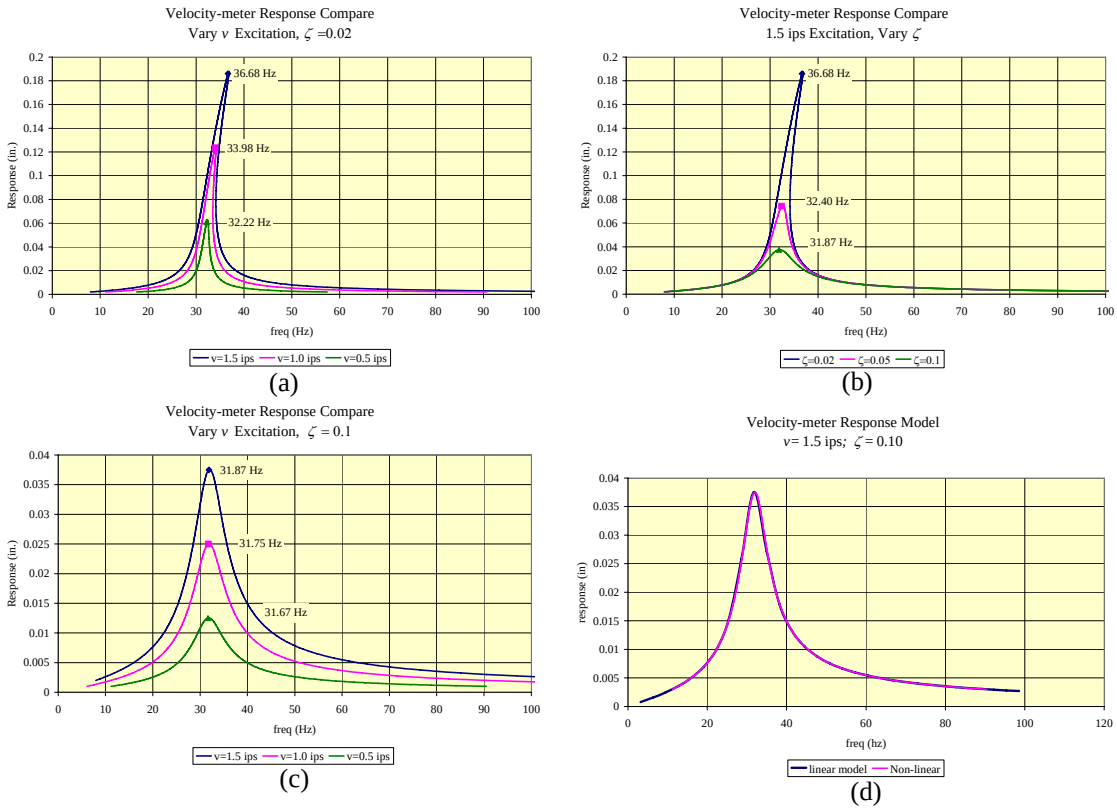

Figure 3.24 Non-linear Velocity Sensor Response

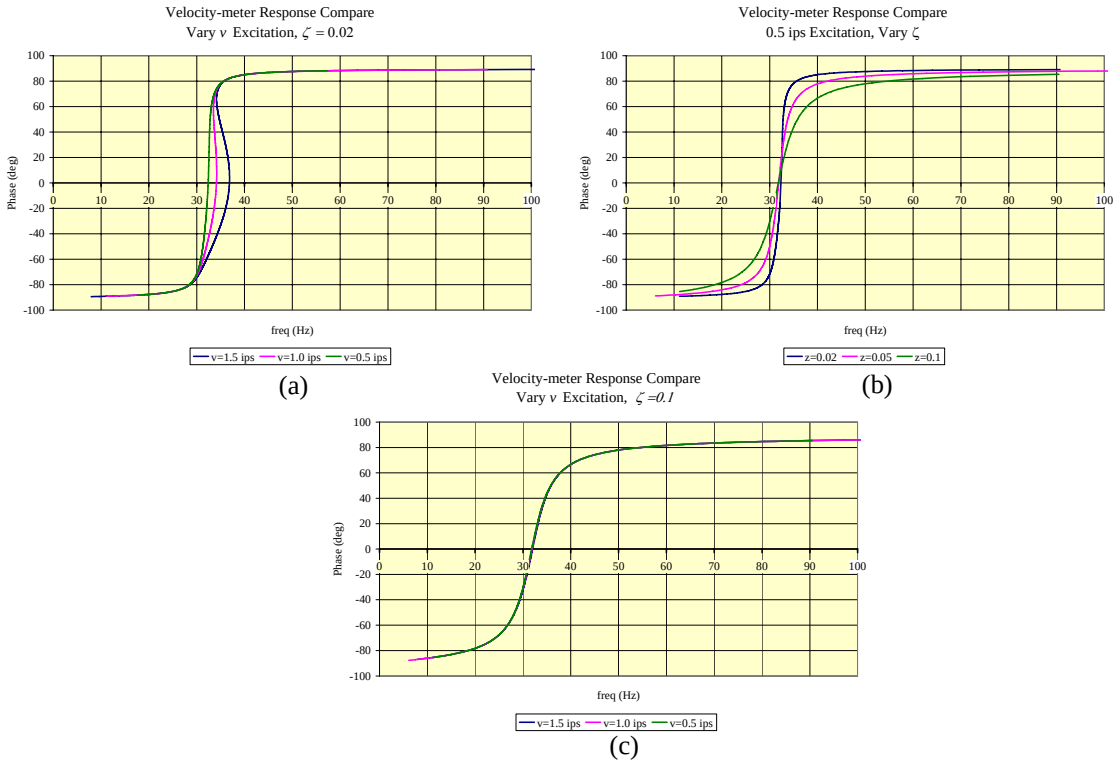

Figure 3.25 Non-linear Velocity Phase Response

3.6.3 Interpretation of Results

The results from the acceleration and velocity analysis yield results that will provide information regarding how the gap spacing between the proof mass and the sensor head will vary for a given excitation level as well as for various levels of damping. This is different from the response plots presented in Section 2 as those plots presented the response as ratios of output to input, H/X_0, v/v_0, a/a_0, and, the abscissas of those plots are defined in terms of the frequency ratio, ω/ω_n. Applying the following parameters for the acceleration and velocity based models, $\alpha=3913.9$, $\beta=518645.5$,

ω_n=*31.8* Hz.(199.7 rad/s) and the appropriate damping ratio and excitation levels yields the results shown in figures 3.22 through 3.24.

Two parameters that are of concern are the excitation level and the amount of damping as it is desired to get an understanding of how these two parameters influence the overall response for a given system. The first case, figure 3.22-a, shows the response when the damping ratio is fairly light, ζ=*0.02*, and the excitation levels vary from 0.5 to 1.5 *g's*. Here it can be observed that the response peaks lean to the right as the excitation levels increase. This causes two things to occur. The first is that the response point increases to the right and the second is that the area of instability (excitation frequency that can have more than one response level) increases as well. Figure 3.22-b shows how increasing damping for a given excitation level, *g=1*, causes the response curve to tend toward the geometry that is observed for the linear model. Also, it is important to note that damping causes the response peak to shift to the left, or reducing in value. Figure 3.22-c shows if the damping is sufficiently high enough, the response curves for different levels of *g*, take on the shape for a linear response. Also, unlike the responses shown in figure 3.22-a, the peak response point does not vary as greatly and there are no regions of instability. The last figure in this series, figure 3.22.d, shows the linear model and the non-linear model on top of each other. These results are not indicative of all possible operating configurations, but it does provide insight into possible response modes.

The second set of figures examines the response for a velocity based sensor. A similar approach for analysis was applied as for the previous case of the accelerometer

based sensor. The results from this analysis are similar as that found in the accelerometer case. However, comparison of when the peak response frequency occurs will show that the values for the accelerometer case and the velocity case are slightly different. The reason for this is that the natural frequency of response is dependent on the excitation amplitude for the non-linear case. Also, the combination of the excitation amplitude and amount of damping also can attribute to the subtle differences in peak response frequency.

3.7 Summary

The material presented indicates that the information regarding how the assembled sensors respond is strongly determined by the magnetic force developed over the gap. The analyses also show that a nonlinear response can be expected, but that if the level of damping is sufficient, the non-linear response will not be as noticeable. Also, even if the damping was low enough that the non linear behavior could occur, there is a region where operation could occur. Section 4 will discuss testing methodology to determine the response of the sensors to static as well as dynamic gap changes.

4 PARAMETER AND CHARACTERISTICS METHODOLOGIES

4.1 Introduction

To determine the response characteristics of the developed sensors a set of static and dynamic tests were conducted. Sections 2 and 3 presented the expressions that relate the response of the FFPI based vibration sensors subjected to either a static or dynamic load. Since the sensors have parallel constructions, the testing procedures developed here will apply equally to the FOGS and the FOVS sensor with minimal differences in test setups. The discussion will start with the static tests and then proceed to the dynamic tests. Finally, the full sensor system including the signal conditioning unit (SCU), data acquisition system, and computer will be discussed.

4.2 Static Testing Methods

Two types of static testing were conducted. The primary objective for the first type of static test conducted was to verify that the embedded FFPI within the mandrel, or hypo-tube, produced the expected linear response for a given load range. The primary objective for the second type of static test was to determine the overall sensor response when the air gap between the sensor head and target was varied. Each test required that a known incremental input be applied and then the resulting response was monitored and recorded.

4.2.1 Static Test: Deadweight Tests

The objective of the deadweight test is to determine the response of the embedded FFPI to a known load. The input parameter here is a known incremental load in the form of calibrated masses. Figure 4.1 shows a typical test set up. Figure 4.1(a) shows the sensor body secured in a holder. At the sensor head, there is a steel hanger support that is held in place by the magnet anchored to the sensor head. The weight basket is held by an S-hook. Figure 4.1(b) shows a close up of the transition between the hanger support and the sensor head. Care was required to keep the applied load aligned with the axis of the mandrel or hypo tube. Ideally, the FFPI should be in the center of the tube. But, since the diameter of tube is over three times the size of the FFPI, the actual orientation of the FFPI is unknown. The ideal applied load would be a purely axial load, however, due to issues with assembly and applying the load, the actual load applied will be a combined axial and moment load as discussed in Section 3. The design of the sensor does allow for the sensor head to retract far enough into the sensor housing so that the hangar support is constrained within the housing. However, there was enough clearance present that would still allow the hanger support to be off axis by a few mils (1mil = 0.001 in= 25.4μm.).

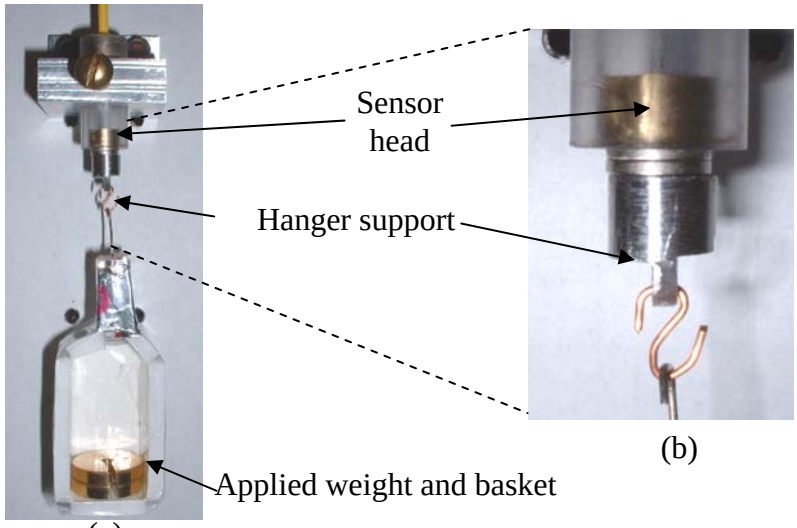

Figure 4.1 Exemplar Dead Weight Test

The procedure applied for this test was to apply incremental loads until either the maximum absolute voltage (5 volts) output from the SCU is obtained, or if one fringe was obtained. The loads used to calibrate are 0.011, 0.022, and 0.044 lb (5, 10, and 20 gram) weights. The maximum load applied is about 0.551 lb (250 grams). Since the hanger support is relying on a contacting magnetic force to secure the weight basket to the sensor head the loads applied need to be light enough to insure that separation between the sensor head and weight basket does not occur. One trial of load capacity was done with the magnet on the FOGS able to support a 2 lb (958 gram) load. Objectives from this test are to determine the overall sensitivity and to determine the linearity of the FFPI to an applied linear load. The overall sensitivity of the system is a function of the sensitivity of the measurement system, including the signal condition unit and data acquisition system, and will be discussed at the end of this Section. However, there is one aspect of the signal conditioning unit (SCU) that merits a discussion. The

optimal quadrature point is a moving target due to laser drift and possible thermal influences at the FFPI and the SCU can adjust the current to the laser and effectively change the optimal quadrature point. For this reason, the signal observed by the SCU is not an absolute measure in regards to the mirror spacing, but rather a relative change in mirror spacing.

The procedure applied was as follows:

1. Zero out SCU, and set data acquisition to record. The data acquisition system displays the registered voltage and % fringe.
2. Apply first incremental mass and record the observed voltage and % fringe. Due to noise at the photo detector and other sources, an average value is taken of 20 to 50 points.
3. Addition of the next incremental mass can be down one of two ways:
    a. Option A: Do not reset the fringe and apply the next mass recording the accumulated voltage change and fringe change.
    b. Option B: Reset the fringe, apply the next mass and record the voltage change and fringe change. These changes would then be added to the previously recorded values.
4. Continue with 3 until final load value, or maximum SCU output is obtained. Then plot the recorded results.

Step 3b. in the procedure requires some explanation. Again, the FFPI is not suitable for static measures due to a drift in the observed signal primarily due to laser drift and thermal influences. So, obtaining accurate and stable static readings is a tricky process.

Option 3.a is doable for a well behaved system, and if the static load is applied “fast” enough. Otherwise, option 3.b allows you to observe the relative change for each increment, from which the accumulated results can then be plotted. One cautionary note regarding this test is the attachment of the hanger support to the sensor head. The off axis positioning of the hanger support can introduce a moment loading which can, as shown in Section 3, alter the desired axial load. The positioning of the hanger is done by eye and a misalignment of a few mils is quite probably. For this reason, it is necessary to conduct a number of tests with the hanger attached, then resetting the hanger and repeating the tests. This will produce a range of operation. An additional consideration for the hanging load is the swinging of the basket. Although the frequency and amplitude are low, the swinging can introduce a higher than expected value for the static load. The swinging can be minimized by applying a suitable averaging period that covers two to three periods of the natural frequency of the basket. The rate at which the load is applied to the weight basket is also of concern too. That is, just dropping the weight into the basket will cause a spike in the loading and it is possible to overshoot the nominal static value.

4.2.2 Static Test: Gap Calibration

The primary objective for the second static test conducted was to determine the response of the sensor to the change of the gap. The previous test provided a relation between an applied load and resulting voltage output. Coupled with the data from the gap change to voltage change, the load developed on the sensor due to the change in magnetic force can then be determined. Although the force relationship is not really

required, the information could be useful to relate the magnetic field properties to the sensor properties and this information could be useful for future sensor development. The force measure could also be useful to determine whether the force developed for a particular gap setting could impact the body to be measured.

The response of the FOGS to a change in gap for a static change was done by placing a steel target on an incremented index stage. The drum of the index stage is incremented in 0.02 mm and was outfitted with a ten turn 1-kΩ potentiometer so that the movement of the stage could be monitored by the data acquisition system, figure 4.2. This allows for the calibration to be done with the problems described for the deadweight testing to be minimized in regards to laser drift and other influences. The barrel micrometer drum translates as it rotates requiring that the potentiometer outer casing is allowed to travel while not rotating. This allows the potentiometer wiper to move providing a direct correlation between the translation of the index stage due to the adjustment of the barrel micrometer to the change in voltage across one leg of the potentiometer. The use of the potentiometer allows for an analog reading of the index stage and the resulting voltage can be used to provide an absolute as well as relative measure of displacement. The system is adjustable so that the index stage can be set at the half way point of the barrel micrometer and the potentiometer can then be adjusted so that it is at mid range too. This allows for the observation of the sensor response to motion about a particular gap setting.

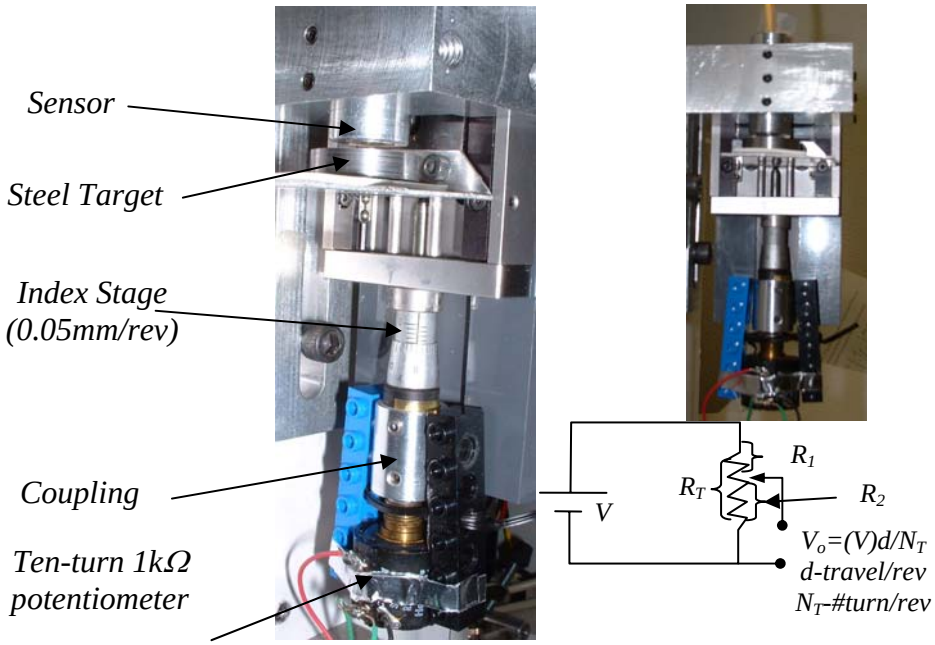

Figure 4.2 Gap Calibration Rig

The gap calibration test conducted is to observe the response of the sensor to a large change of the gap. This test provides information regarding the nonlinearity of the expected sensor response over the entire range of travel. This test can also provide information regarding how linear or nonlinear the response is about a particular gap setting for a given amplitude of motion. The procedure for the gap test is as follows:

1. Set the barrel micrometer so that it is at midrange. Then set the potentiometer so that it at midrange.
2. Adjust the sensor till the desired gap is obtained. The gap can be set by use non-ferrous gap gages such as Bently Nevada's plastic feeler gages.
3. Trigger the SCU so that the reference fringe is reset.

4. Activate the data acquisition system. The rate of change of the gap is to be slow, so the rate at which data is collected should be set appropriately, 20 sample/sec as an example.
5. Turning the barrel micrometer clock-wise will close the gap while turning the barrel micrometer counter clockwise will open the gap. The rate at which the barrel micrometer is rotated should be steady. The amount of gap change can be observed by watching the hash marks on the barrel micrometer. Each small hash mark on the barrel signifies 0.5 mm (19.7 mils) while each hash mark on the drum signifies 0.02 mm (0.787 mils). Note: 1 mil =0.0254 mm.
    a. Motion about a fixed gap: Turn the barrel micrometer to a preset gap change in one direction, then turn the barrel back in the opposite direction till the same gap change occurs on the opposite side of center.
    b. Large motion. Large motion requires that the barrel is turned continuously until either the voltage limit of the SCU is reached (5 volts) or the desired large gap change is reached.
6. Save the data and make necessary notes on observations.

The tests require that a number of iterations are performed so that an overall average can be obtained. Key things to observe in the data set are that the data sets are repeatable, data follows a consistent line, i.e. little scatter of data points, and any abrupt changes in trends.

The static testing for the FOVS sensor is a little different due to the presence of the proof mass. The same instrumented index stage is applied but the fixture mounted to the index stage is such that the proof mass is held fixed and the housing is moved, figure 4.3. This rig allows for the proof mass to be set at its equilibrium position, or at one of the two extremes. The principle of operation for this sensor arrangement is that the force developed between proof mass and the sensor head is registered by the FFPI imbedded within the hypo-tube. Once the rig is assembled, the procedure for testing is the same as for the gap testing for the FOGS probe.

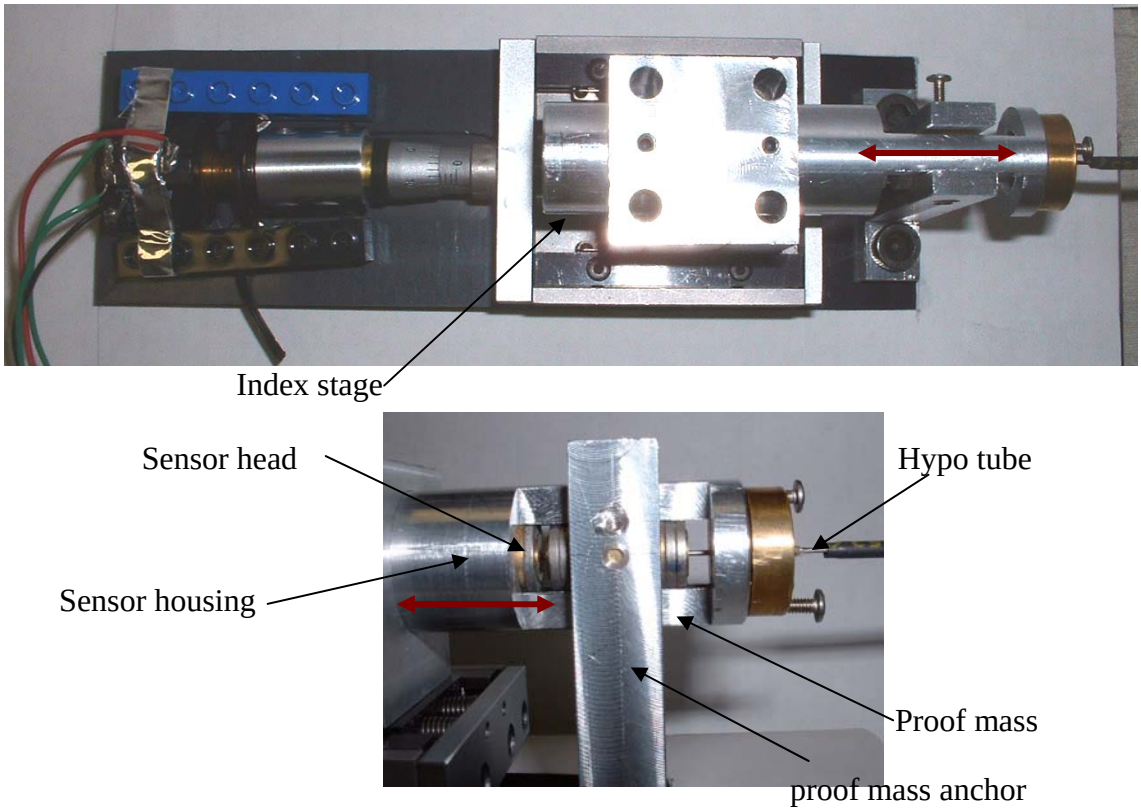

Figure 4.3 FOVS Gap Testing Rig

4.3 Dynamic Testing

The static tests provide information on how the overall sensor, which includes the electronics, responds to slow variance of the change in gaps. The static tests also provide information that can be used for a conversion of the registered voltage to a measurand value, i.e gap change. Dynamic tests are required to show how the sensors will respond overall to dynamic vibrations. In addition, the tests will also incorporate an eddy current probe (Bentley Nevada 3300-XL series) and accelerometers (PCB 100 mV/g and a 50 mV/g) for a comparison. By using the eddy current probe (ECP) this will provide information regarding the displacement of the shake table and the accelerometer will provide information regarding the acceleration. The use of two industry standard sensors is necessary so that each of the developed sensors can be compared to them. Each sensor will be subjected to two dynamic tests. The first sets of tests are done utilizing a shaker box and the second sets of tests are done on an actual machine. The FOVS will be subjected to a free response test so that the natural frequency of it can be determined.

4.3.1 Free Response Test (Flick Tests)

The flick test subjects the test specimen, namely the proof mass of the FOVS, to an initial deflection and then released causing the proof mass to vibrate. The objective of this test is to observe what the natural frequency is and also possibly the mode of damping as well as an average damping ratio value. This test will require that a number of flick responses are obtained so that the time traces can be compared to ensure that the results are repeatable. Analysis of the time waveforms can provide information on the

damped natural frequency and damping ratio by examining the peak response values. Augmented Fourier transforms can also be utilized to observe harmonic components.

4.3.2 Dynamic Test - Shaker Box

The shaker box is an instrument used to check the calibration of vibration sensors. The shaker table used was a Model 813 by Hardy Instruments (formerly Dynamic Instruments). The shaker box has a platform driven by an inductance coil. The excitation frequency can be varied from 10 Hz to 1500 Hz. However, the shaker box is rated for a ±3% of the displayed output level for excitation frequencies from 30 to 1500 Hz. The input amplitude can be either in zero to peak (0-Pk) acceleration, zero to peak velocity, or peak to peak displacement. The allowable amplitudes are limited depending on the weight on the sensor mount. The allowable amplitude is related to the maximum number of g's the shaker table can delivery through the induction coil. The shaker table has a 50 mv/g accelerometer embedded within it for reference. The table also allows for attachments to be threaded into the table mount as well as brackets to accept other sensors, figure 4.4.

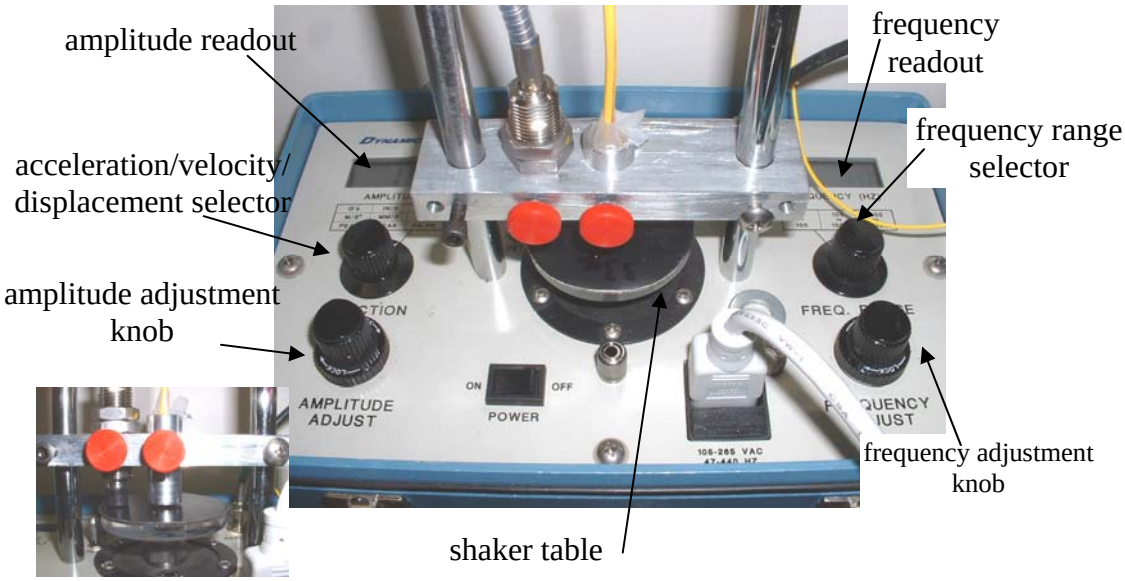

Figure 4.4 Shake Table for Dynamic Response

4.3.3 Dynamic Response Test

The primary objective for the first dynamic response test is to determine the overall response of the sensor for a given range of excitation frequencies and amplitudes. The test is conducted by setting the excitation frequency below the resonance frequency of the sensor and stepping the excitation frequency beyond the resonance frequency. The resulting response should then take the form to one of those presented in Section 3. By conducting the tests at different amplitudes, or acceleration levels, the resulting range of responses can be used to determine threshold levels to generate a suitable observable signal as well as maximum observable levels. A suitable signal will be defined as one that represents “smooth” sine wave as should be observed by the eddy current probe (ECP). The maximum threshold value and minimum response are restricted by the

signal conditioning unit and data collection system. The maximum threshold of 5 volt output from the SCU will restrict what maximum input levels can be applied to the sensor. Gap distance will play a role in this too. That is, in the case of the FOGS, if the gap is nearly closed, then the response of the FOGS for small gap changes could result in the output voltage of the SCU to max out at 5 volts. The minimum threshold value is that value that is required to overcome the resulting noise from the SCU (photo detector shot noise) and the minimum byte level of the data acquisition system.

The data to be collected for this test are the time waveforms and the resulting spectrums. From this data the excitation frequency and resulting response amplitude at this frequency for each sensor will be extracted. The phase response for each test sensor will be examined and related to the response of the reference probes. The time waveforms will under go an initial operation to remove any DC offset that may be present in each signal, and then the waveforms will be processed using windowing operations from which the spectrums will be determined.

4.4 Dynamic Test-Demo Rotor Kit

Demonstration of the FOGS and FOVS sensor to an actual application will be demonstrated by utilizing a demo rotor. Although the demo rotor is a simplified mock up of an actual machine it is capable of providing vibrational scenarios that emulate an actual machine. That is, although the machine may operate at a constant speed, the resulting vibrations are not a singular vibration due to the interaction of all the assembled components, thus the sensors are subjected to many different vibrations. The

intent of this test is to demonstrate the capability of the FOGS and FOVS to sense machine vibrations.

The demo rotor has a thick disk that is attached to a slender shaft mounted on ball bearings. The shaft is driven by a rubber belt by a variable speed motor. The kit is capable of operating from 120 rpm (2 Hz) to 3300 rpm (55 Hz). Figure 4.5 shows the rotor kit as well as the placement of the various sensors. The rotor disk is made of steel, has a width of 1 inch (25.4 mm), a diameter of 3.25 inch (88.6 mm), and weighs around 2 lbs (8.91 N). The bore on the rotor is 0.375 in (9.52 mm) and is machined such that the shaft is a slip fit. The rotor is secured to the shaft by set screws on either side of the rotor face. The attachment of the rotor to the shaft results in an eccentricity of the rotor assembly which can change depending on the alignment of the rotor disk eccentricity with the shaft's eccentricity at each assembly. This is due to the presence of eccentricity of the shaft, possible bow of the shaft, eccentricity of the rotor, and that the tightening of the set screws can force the rotor disk off center. The rotor rotates n a anti-clockwise motion as viewed in figure 4.5. The 1X rotation of the rotor is obtained by utilizing a Hall effect sensor. This sensor is used to provide a reference for each revolution of the shaft by generating a voltage spike from the passage of a slot on the shaft. The FOVS and a 0.1 V/g accelerometer are attached to the horizontal cross beam. The prototype FOGS sensor was developed so that it would respond in the vertical direction and is oriented along the vertical, or Y axis of the rotor. The ECP probe is oriented so that it is aligned with the horizontal, or X axis of the rotor. By orientating the ECP and FOGS so that they are oriented by a 90^0 angular separation allows for the orbital motion of the

rotor disk to be obtained. This represents a typical application of gap sensors as applied to the monitoring of rotating equipment and for rotordynamic studies. A rigorous rotordynamic study would require that the mechanical runout, or the orbit due to geometrical features with the rotor turned at a slow speed (i.e. 1 Hz), be subtracted from the orbit of the rotor at operating speed. The resulting orbit would then reflect the response of the disk to dynamic loads. Since this demonstration is to show that the

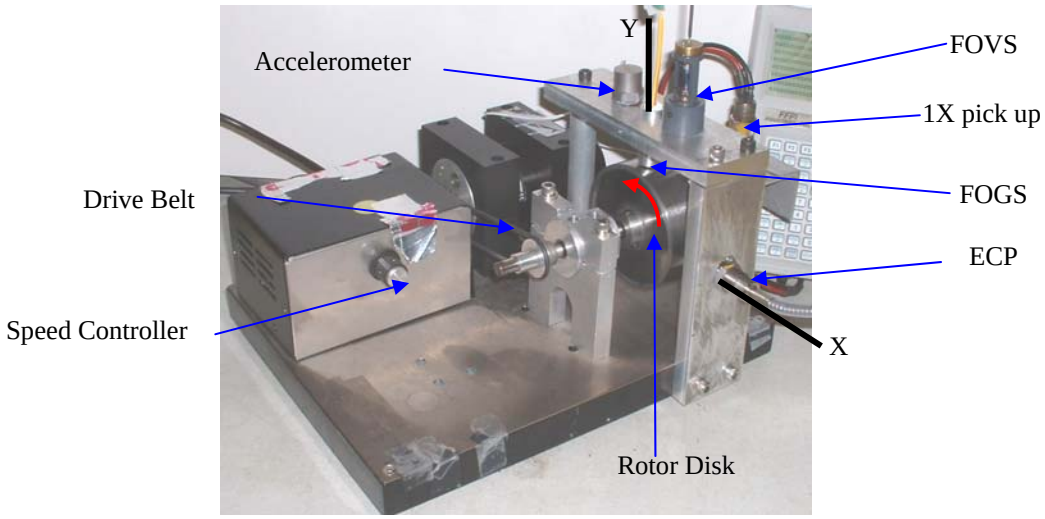

Figure 4.5 Demo Rotor Test Stand

FOGS is capable of responding to the similar excitation as the ECP, the orbits presented will be uncorrected.

The tests conducted are studies that essentially demonstrate how the developed sensors respond when subjected to a vibratory system that can produce a rich spectrum of vibration amplitudes, frequencies, and act in multiple directions even though the system operates at a single speed. This is a sharp contrast from the dynamic tests

utilizing the shake table where the direction, amplitude, and the excitation frequency of the vibrational excitation are controlled.

4.5 Signal Conditioning Unit and Data Collection

The monitoring of the FFPI is done by using a Signal Conditioning Unit (SCU). The SCU is a commercial device from Fiber Dynamics Corporation (disbanded in 2004) that can monitor up to 24 FFPI systems at one time. The SCU is limited in sampling rate to 2400 Hz and provides a bipolar output of ±5 Volts. The SCU is capable of resetting the optimal fringe level through either a triggering device, or by manual means. This reset feature is useful to remove any DC component that can arise due to laser drift or thermal growth. For the length of the tests conducted, the manual means for triggering was employed. The scheme employed by the SCU for monitoring the FFPI is covered in [6],[20], and [28].

The data collection system consists of a National Instruments (NI) data acquisition system and a 400 MHz Pentium II computer. The NI data acquisition board used was an AT-AI-16X6-10 coupled with a NI BNC-2090. The board is limited to a 12 byte sampling resolution. LabVIEW 6.0 was used to generate the virtual instruments that were used for collecting, signal conditioning, observation, and storage of the data from sensors for each test. The primary data operations to look at were time waveforms and spectrums.

5 RESULTS AND DISCUSSION

5.1 Introduction

The results from tests that were conducted will be presented in this section. The presentations will start with results from static tests and then the dynamic tests for each sensor and then a final presentation will cover the dynamic results from a demonstration rotor test stand.

5.2 Fiber Optic Gap Sensor (FOGS) Test Results

5.2.1 Static Deadweight Test

The first static test conducted on the FOGS sensor was to determine the linearity of the FFPI that was embedded within the hypo tube. This test consisted of applying a set of known masses on to the sensor head and observing the resulting voltage change, figure 5.1 is a plot of these results.

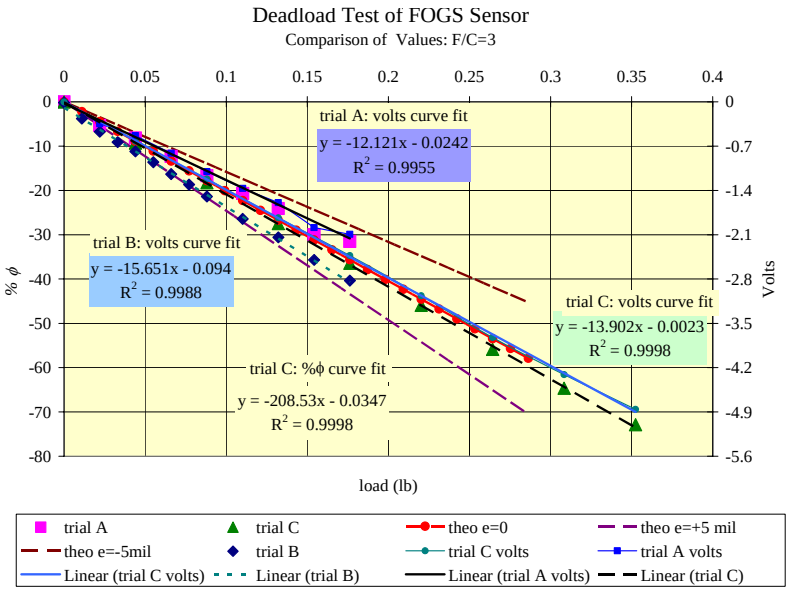

Figure 5.1 FOGS Dead Weight Response

The % fringe, %ϕ, shown is calculated from the observed voltage. The % fringe is used to relate the observed voltage to the deflection within the hypo-tube/FFPI, equation 2.11. The full-scale, *F*, and calibration constant, *C*, that are set on the SCU also dictate the observed voltage. The ratio of *F/C* effectively acts as an indicator of the gain. That is, an *F/C* =1 should respond with three times more sensitivity than an *F/C* =3. By utilizing an *F/C=3* for this test allows for a larger range of weights to be applied. One measure that is useful to know is how much load is required to generate one fringe shift, or 100%ϕ corresponds to π radians. Since the maximum output of the SCU in a bi-polar configuration is ±5 volts the graph in figure 5.1 shows that for trial C a maximum output voltage of 5 volts was reached when a load of about 0.35 lbs (159 grams) was applied. This translate to an axial stress of 427 psi (2.94 MPa), and, the load only generated about a 70% fringe shift. This would also indicate that for an *F/C*=1, that a load of 0.1167 lbs (53 grams) would generate a 5 volt output. Figure 5.l shows the results from three dead load tests, Trial A, Trial B, and Trial C. Each test does generate a linear result with a COD of linear fit greater than 0.99. However, each test has a slightly different slope. An explanation that can account for the difference in slope was presented in Section 4 in that applying the dead load exactly along the axis of the hypo-tube or FFPI is difficult to achieve and the result is that a moment load will occur. As a reference, two theoretical lines that represent an eccentric loading of ± 5 mils are shown that represent an envelope which does contain the measured results. In addition, a third theoretical curve is shown to represent the response if no eccentricity is present. The three theoretical trends do match up well with the measured trial data.

5.2.2 Static Gap Testing

The static gap testing of the FOGS was done by utilizing an index stage outfitted with a potentiometer. This yielded data that was used to correlate the change in gap to the response of the FOGS. The data was collected by setting the gap to a maximum gap value, as an example, of 80 mils (2.03 mm) and then closing the gap till either the maximum output voltage (5 volts) of the SCU was reached or if the gap was nearly closed (around 5 mils (0.127 mm)). Full closure of the gap was not done as this would require a larger force to break the contact holding force between the magnet tip and the target plate and could result in overloading the 5 volt SCU limit or overload the sensor. Then, the gap was reopened until the initial starting point was reached. Figure 5.2 shows the raw data for a sample test. The upper trace shows the motion of the index stage

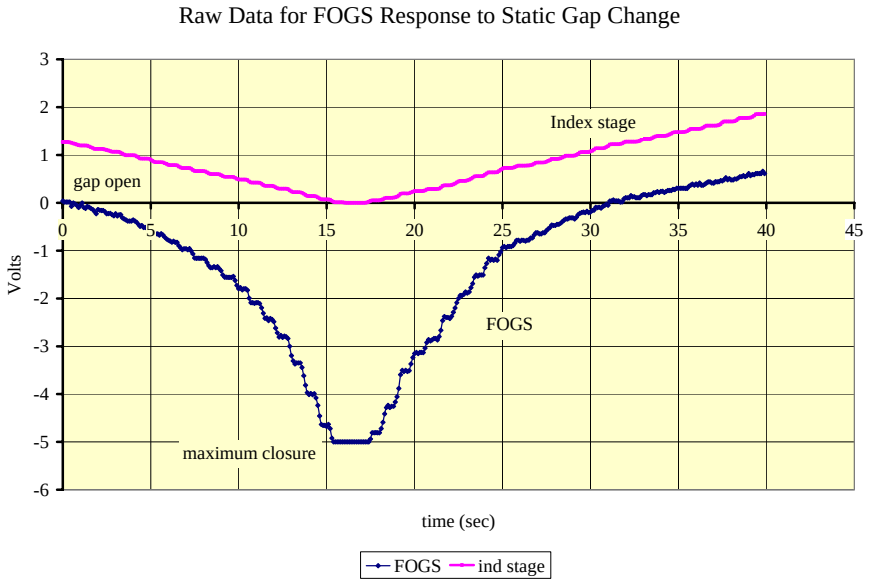

Figure 5.2 FOGS Raw Data Due to Gap Change

while the bottom trace shows the response of the FOGS to the increase in load onto the sensor head. Again, the test was conducted so that the gap was closing which brings the target closer to the sensor head which results in an increase in force on the sensor head which results in a tensile load to be applied to the FFPI. The observed stair-step response shows points where the fingers used to adjust the index stage were repositioned. Also, the left trace showing the negative slope shows the closing of the gap while the positive slopes show the opening of the gap. The next step is to convert the index stage data to translation data and then produce a plot of the FOGS response to the change in gap. An additional observation that can be made is that as the gap closes, the tensile load is increasing on the FOGS hypo-tube which results in a negative voltage. That is, if the SCU is reset to a zero fringe setting, and a negative voltage is then observed if the gap changes on the FOGS, this would indicate that the tensile strain has increased on the sensor and that the gap between the FOGS and the target is decreasing.

The resulting FOGS response to gap change provides information as to how the embedded FFPI responds to the gap change. By plotting the closing response over the opening response, any hysteresis that might be present can be observed. Figure 5.3 shows the resulting plot with curve fits polynomial curve fits of 2^{nd}, 3^{rd}, and 4^{th} order with coefficient of determination (COD) greater than 99.5 for all cases. The data from

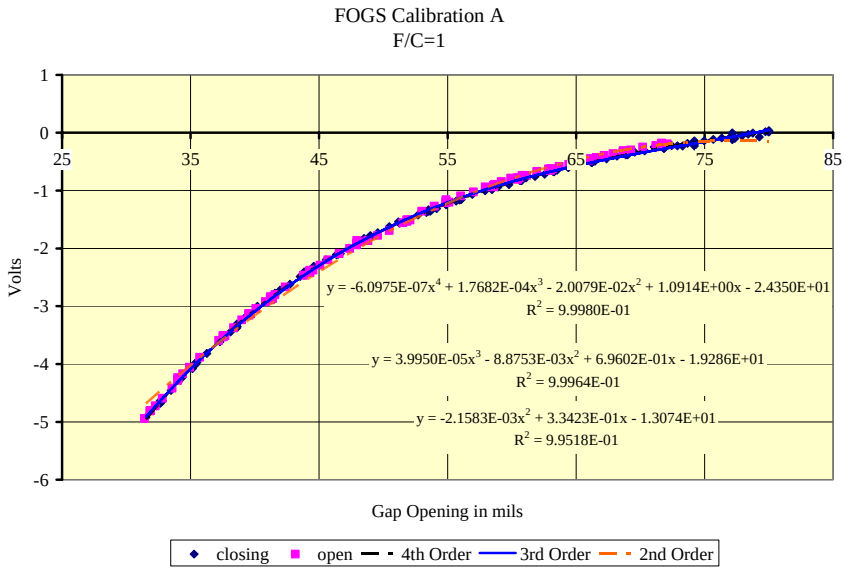

Figure 5.3 FOGS Gap Calibration Curve

this plot can then be used to estimate the amount of force acting on the FOGS due to the gap change by applying the expression found in equation 3.18. Figure 5.4 shows the resulting relative change of force due to the gap change. The expression relative force is used as the SCU is reset at the beginning of each test so that the resulting voltage response is due to the incremental change of force. Observation of the right side of the curve does show that the curve is approaching the abscissa in an asymptotic fashion indicating that there is little change of force near the 80 mil (2.03 mm) gap setting. Also, the static test estimated that a 5 volt output for an *F/C*=1 would be obtained if 0.12 lbs (0.534 N) was applied. The force curve shows that a maximum force around 0.122 lbs (0.543 N) was reached. This confirms the scaling property of the *F/C* ratio in terms of optimizing the output of the SCU to stay within the $\pm$ 5 volt output. The end

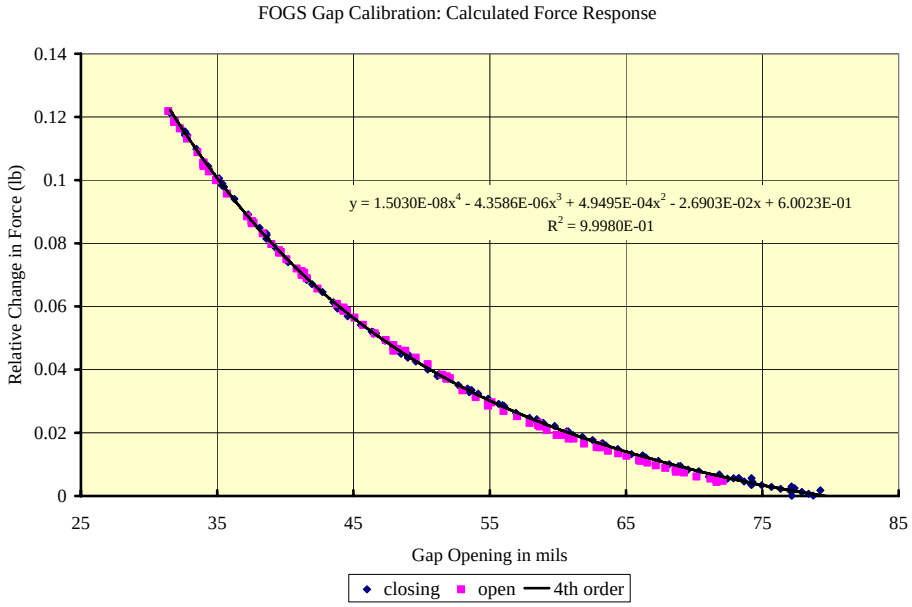

Figure 5.4 FOGS Gap Force Response

objective of the calibration runs is to obtain relations which demonstrate how the voltage response from the FOGS can be converted to displacement measures. To do this, the data from figure 5.3 can be restated by swapping the axes resulting in figure 5.5. The polynomial expressions in Figure 5.5 can be used to obtain the gap change in mils for the corresponding voltage. Note that the results presented here are for a particular F/C setting for the SCU. If the F/C setting is changed, the resulting polynomial values will change. To obtain proper calibration curves, the original data would need to be rescaled appropriately, then the calibration curves can be redefined.

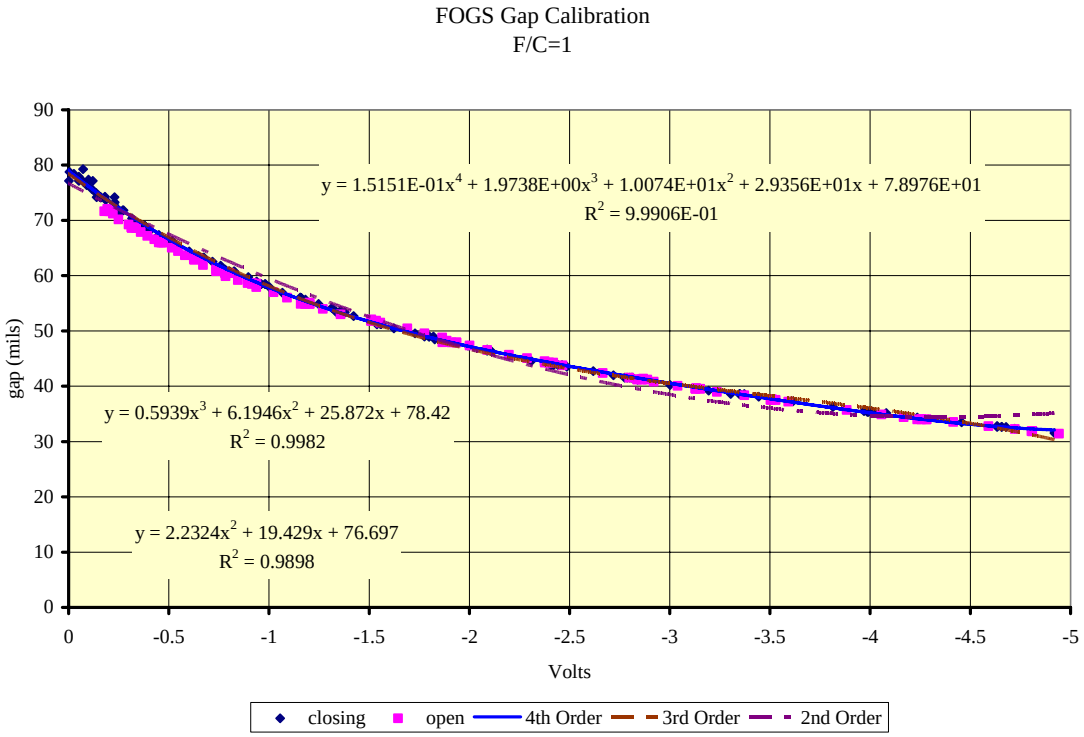

Figure 5.5 FOGS Anti-calibration Curve

5.2.3 Dynamic Testing of FOGS with Calibration Curves Applied

Employing the gap calibration curves (gap to volts) such that the observed signal on the computer display reflects the motion of the target body is done by selecting an arbitrary excitation frequency and observing the response for seven peak-peak (Pk-Pk) amplitudes generated by the shake table. The response of the scaled FOGS will be compared to the response of the scaled ECP (eddy current probe), comparison of the normalized raw time waveform to the scaled time waveform (FOGS only), and corresponding spectrum plots comparing FOGS response to the ECP response. An objective of this demonstration is to show that for low amplitudes of motion, the raw

time waveform of the FOGS is minimally distorted where as high amplitude motion does generate a distorted time waveform that waveform can be “corrected” by passing it through the anti-calibration curve (volts to gap).

The Pk-Pk amplitudes used for this test were 4, 12, 16, 20, 24 and 30 mils (0.102, 0.305, 0.406, 0.508, 0.61, and 0.76 mm) with an excitation frequency of 43 Hz. The gap for the FOGS probe was set to 50 mils (1.27 mm). However, this is the gap between the target and the end of the housing of the FOGS probe. The sensing head is recessed about 7 mils (0.178 mm) inside the housing to protect from incidental contact with the target. This resulted in a total gap around 57 mils (1.45 mm) between the target and the sensing head. Knowledge of the gap for the FOGS probe is necessary as that value is required to apply the data processing scheme presented earlier near the end of Section 3.5, figure 3.13. The ECP was gapped around 30 mils. Figure 5.6 shows the input screen used and the corresponding calibration and anti-calibration curve values utilizing a fourth order polynomial. Figure 4.4 shows an example of the arrangement of the test probes.

The scaled response for the FOGS and ECP are compared in figure 5.7 a through g. The FOGS response appears to show good agreement with the ECP response. The last three figures demonstrate that a linear scaling factor can be applied to the FOGS raw signal and the resultant waveform is on par with the ECP probe response. The response

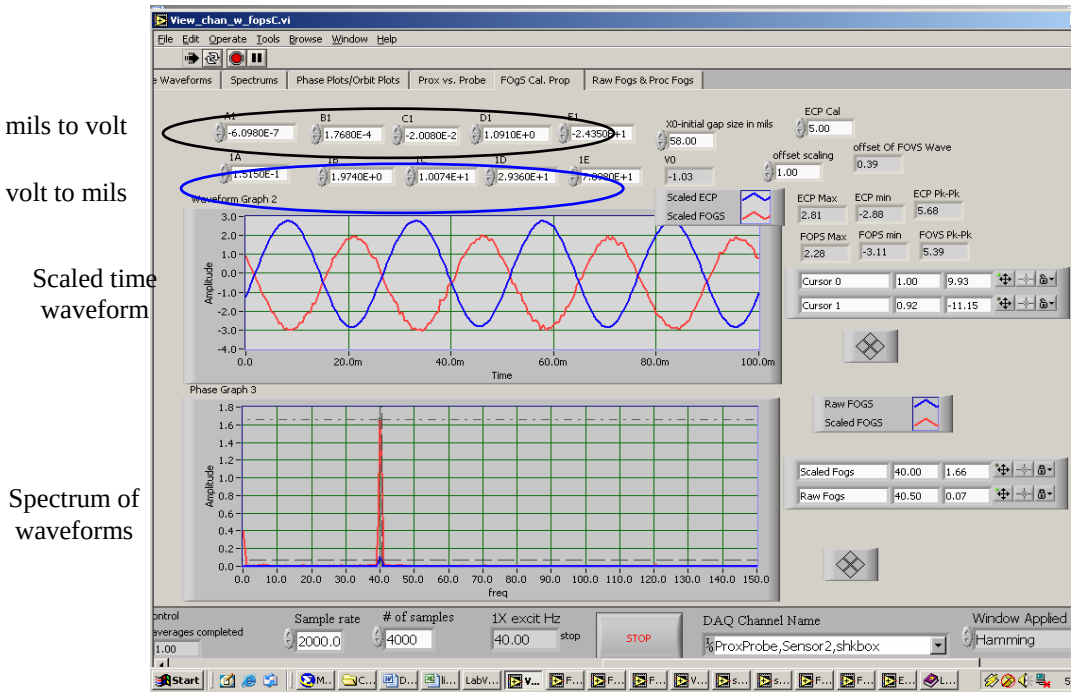

Figure 5.6 FOGS Scaled Data Input Screen

observed for the 4 mil (0.102 mm) Pk-Pk response is a result of the "large" gap. At this gap setting, the amount of tug, and variance of the tug, isn't quite enough to produce a smooth change for a 2 mil (0.05 mm) 0-Pk amplitude. Figure 5.8 reflects the average values for the peaks and valleys for each test case over a two second window. The error relative to the theoretical peak and valley values range from 2% to 10%. It is worth mentioning that the error in the output of the table is ± 3%. An additional note worthy observation in regards to the phase is that the deviation between the ECP response on the FOGS response is very minimal (±2 degrees). This confirms that the phase of the FOGS is nearly zero degrees.

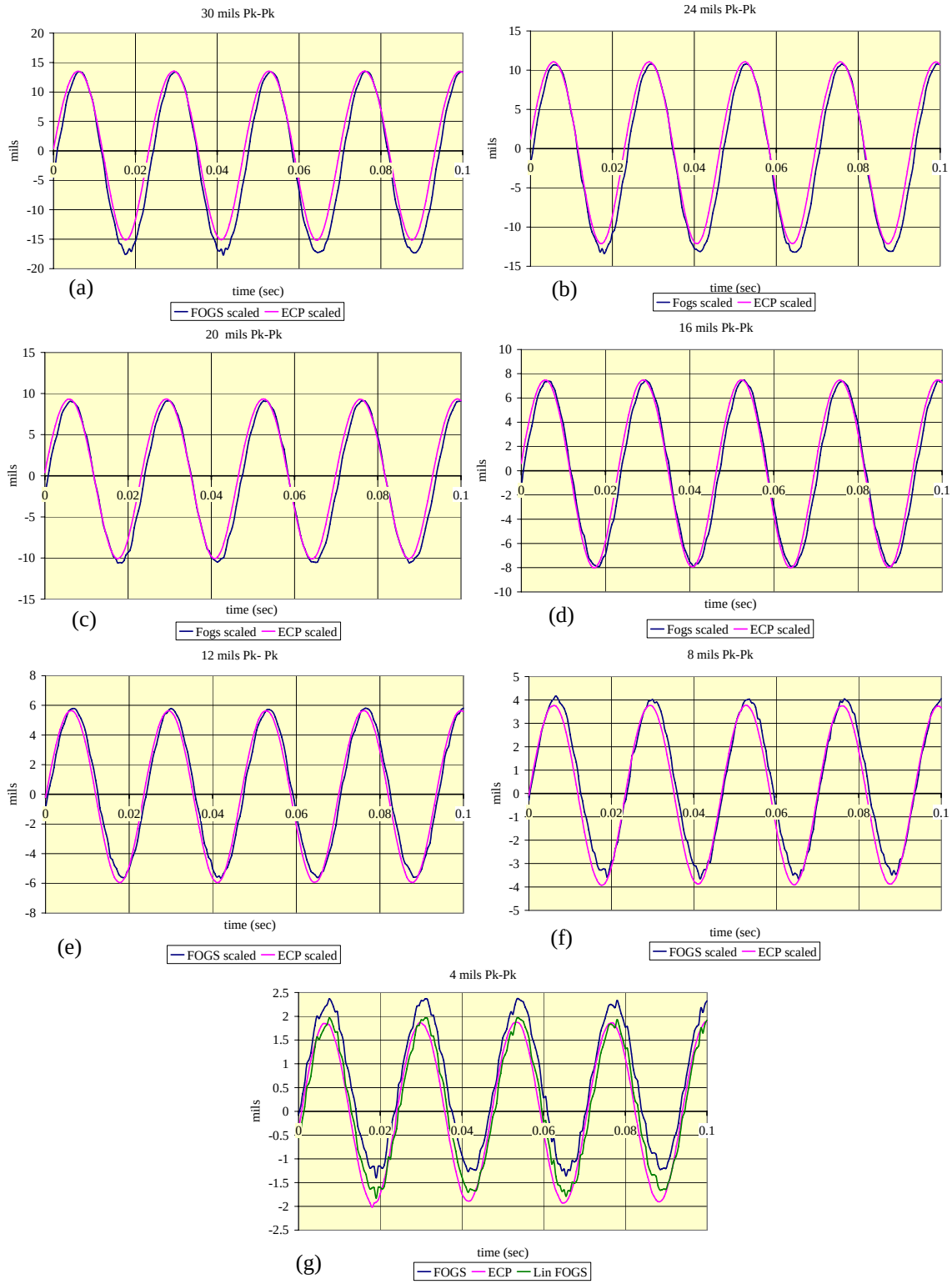

Figure 5.7 Comparison of FOGS and ECP Scaled Data

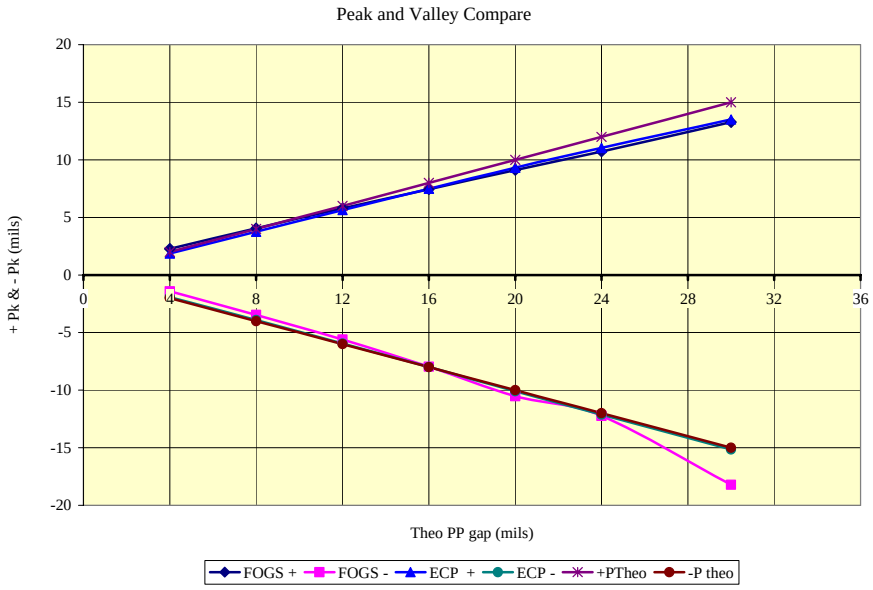

Figure 5.8 Peak and Valley Comparison

As a demonstration of the application of a linear conversion factor for the FOGS to peak to peak motion at or less then 10 mils (0.254 mm), figure 5.9 shows the normalized time waveforms for the raw and scaled FOGS response. The 30 mil (0.762 mm) Pk-Pk response shows that the valleys of the raw data are much sharper than the peaks. This is due to the greatly increased load on the sensor head as the gap closes, but, when the gap fully opens, the amount of pull on the sensor head diminishes. Applying the anti-calibration curve results in peaks and valleys that are more symmetric in shape and amplitude which better reflects the input motion of the shaker table platform. The response of the raw data and scaled data are nearly a close match at the 12 mil (0.305 mm) Pk-Pk response, but the 8 mil (0.203 mm) Pk-Pk and lower responses show a near match on responses confirming that for "small" motions about a gap setting a linear response is possible.

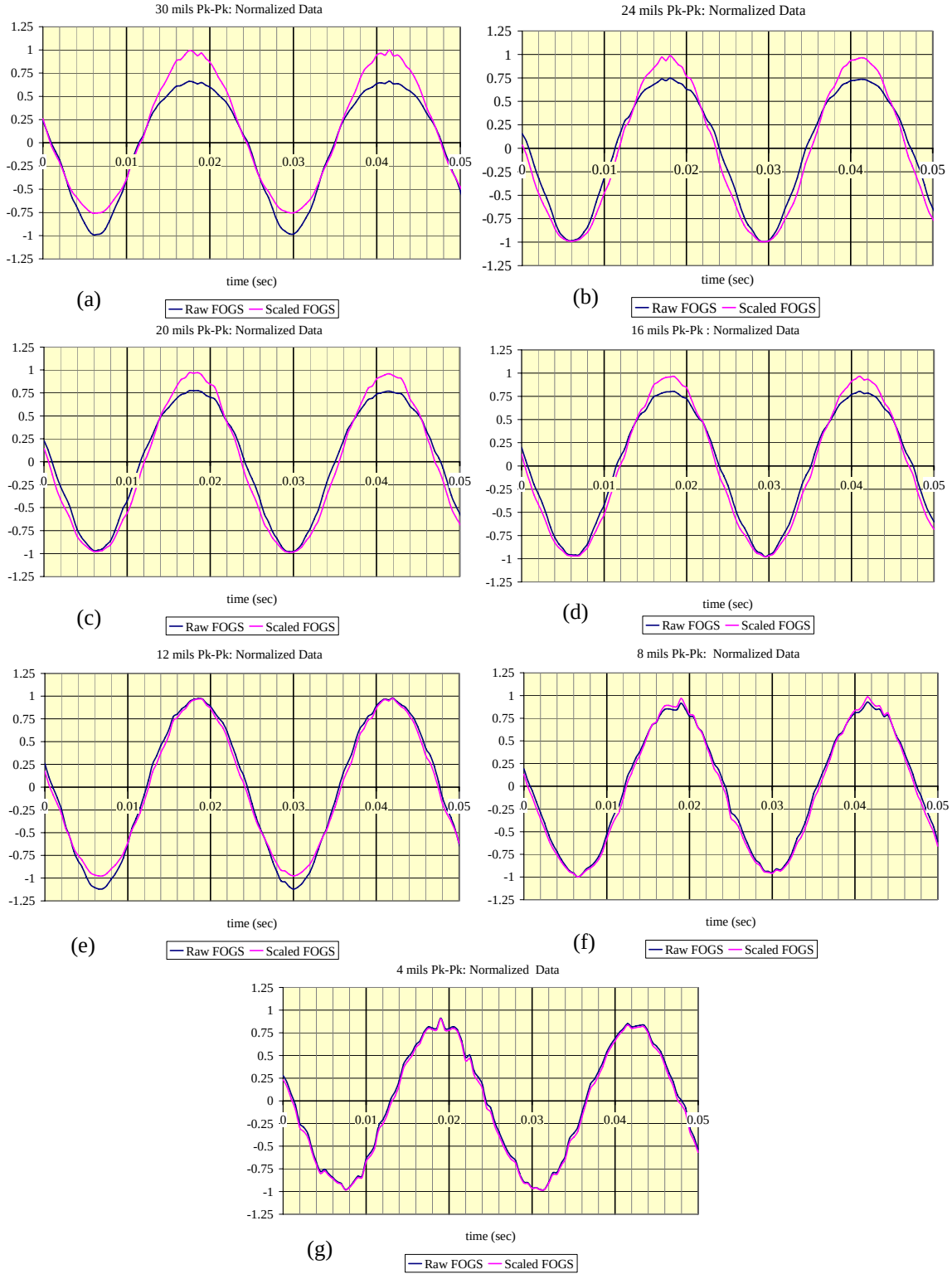

Figure 5.9 FOGS Time Waveform Comparison with Varying Pk-Pk at 40 Hz

The last form of the data to examine is the spectrums. Figure 5.10 shows a cascade plot of the spectrums for each case of the raw and scaled data. The spectrum for each case is presented from the lowest amplitude, 4 mil (0.102 mm) Pk-Pk, to the highest case, 30 mil (0.762 mm) Pk-Pk. Each spectrum is offset in amplitude and frequency for clarification. It is expected to see the amplitudes at the 1X excitation frequency, 43 Hz, increase in amplitude linearly. The more important observation is that the un-scaled spectrums of the FOGS sensor, figure 5.10(b), show 2X and 3X peaks that result from the unsymmetrical time waveforms as predicated in Section 3. However, the scaled spectrums, figure 5.10(a), demonstrate the resulting application of the anti-calibration curve results in time waveforms that are symmetrical. Comparison of these spectrums with the ECP spectrums, figures 5.10(c) and (d), show that the spectrums reflect similar trends since a linear conversion was applied to the raw ECP data, thus the only effect was a scaling of the data. The 2X component that is observed in the ECP spectrums is a result of the ECP tip being too close to the edge of the shaker table platform. The FOGS was located at the center of the table. The last set of graphs, figure 5.11, shown are the power dB of the respective 2X, 3X, and 4X to the 1X amplitudes. Inspection of the FOGS dB plots, figures 5.11 (a) and (b), show that the scaled harmonics dB levels are around 40 dB, or 1 % of the 1X amplitude. Again, the responses observed on the ECP plots, figures 5.11 (c) and (d), are expected to be similar in trend as a linear application was applied. The last plot, figure 5.11(e), displayed is of the shake table response. This was included to show that the level of the harmonics observed in the other two sensors is on par with the shake table accelerometer. The time

waveform of the shake table was not included as the time waveforms had a drift due to the discharge of the accelerometer and the phase response is 180^0 out from the other two sensors.

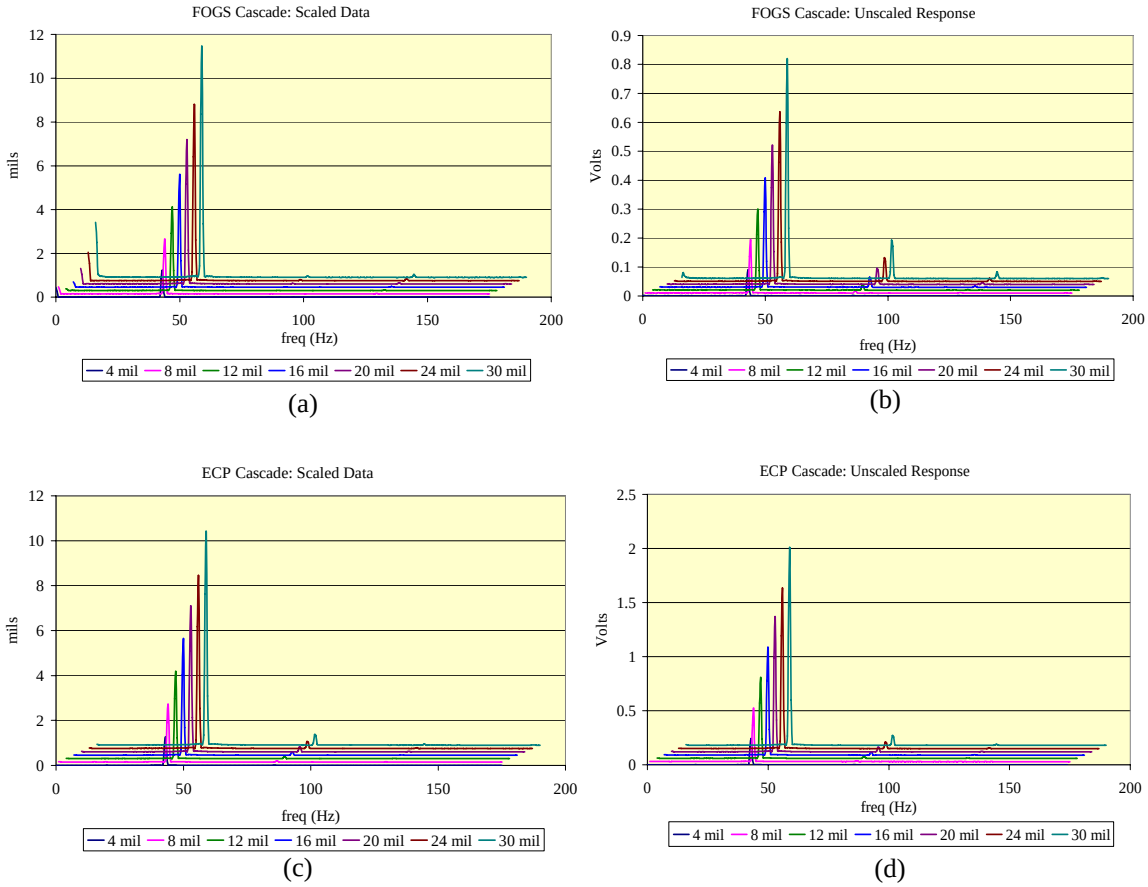

Figure 5.10 FOGS and ECP Spectrum Cascade

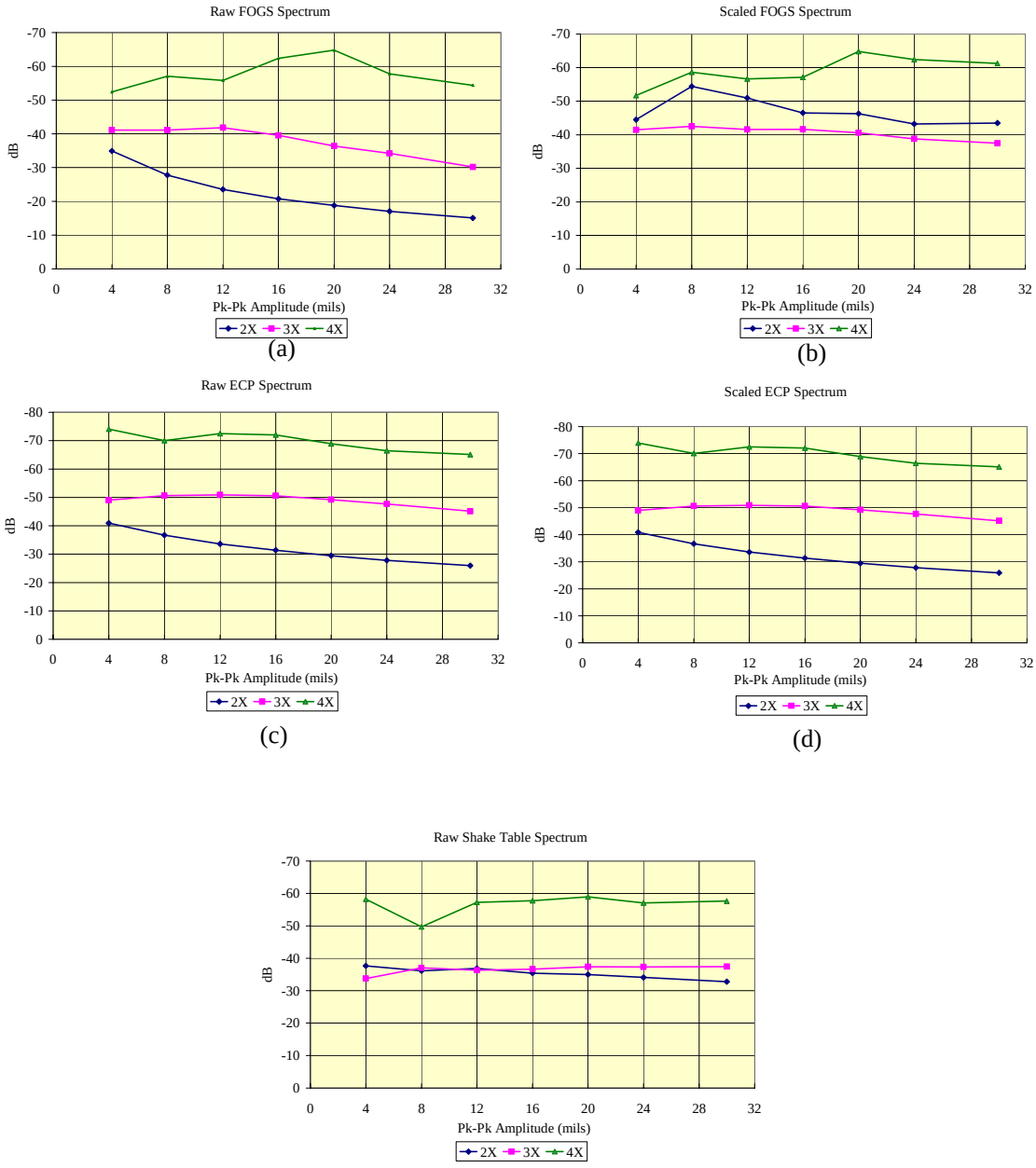

Figure 5.11 Comparison of Harmonics

5.3 Fiber Optic Vibration Sensor (FOVS)

5.3.1 Static Calibration Test

There two static calibrations conducted on the FOVS. The first is the response of the embedded FFPI within the hypo tube and the second is the response of the FFPI to a change in gap between the proof mass and the sensor head. The response of the embedded FFPI is conducted in the same fashion as that conducted for the FOGS sensor.

5.3.2 Static Gap Calibration

The static gap calibration was conducted by changing the gap between the proof mass and the sensor head. This was accomplished by anchoring the proof mass and moving the sensor body by incrementing the index stage utilized for the gap test for the FOGS sensor, Figure 5.12. The proof mass is held fixed to the base plate while the

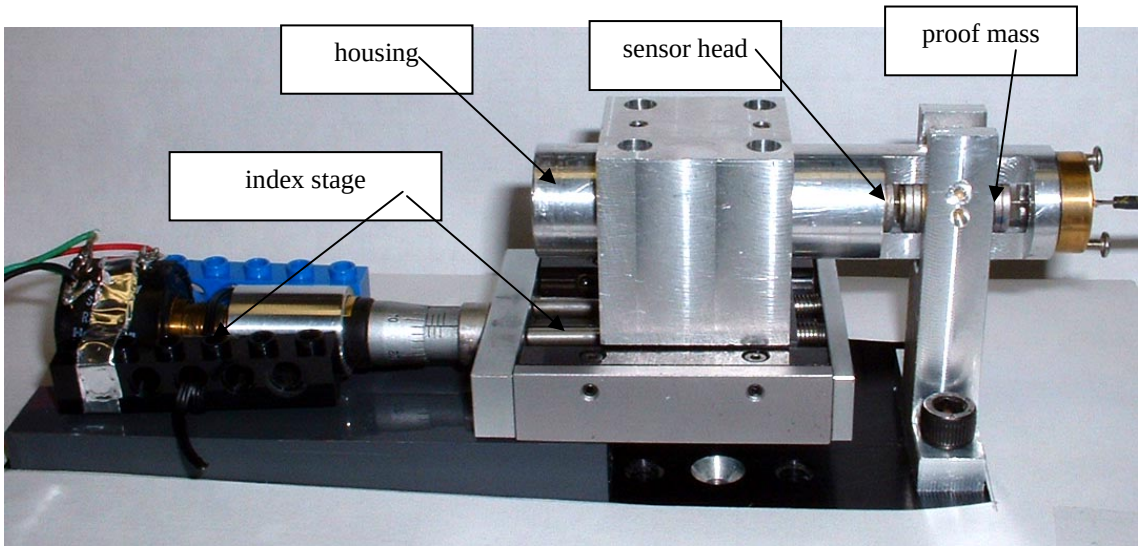

Figure 5.12 FOVS Gap Calibration Test Rig

housing is mounted to the movable platform of the index stage. The proof mass can be moved so that it is either at the maximum gap opening, at the minimal gap opening, or at the equilibrium point of the proof mass relative to the sensor head. Then the gap opening can be incremented by adjusting the barrel micrometer on the index stage. Figure 5.13 shows the test configuration with the proof mass close to the sensor head.

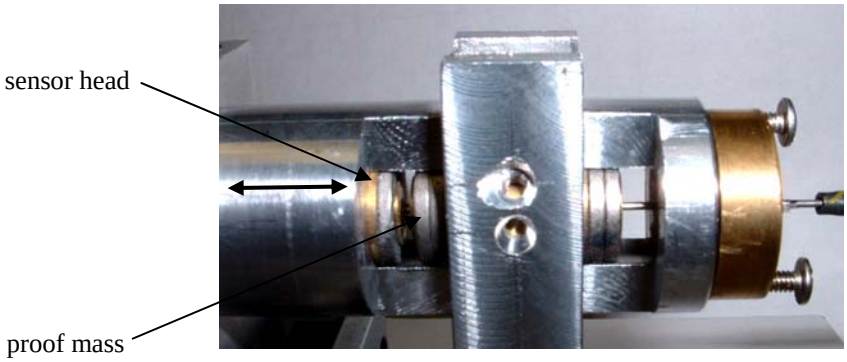

Proof mass close to sensor head.

Figure 5.13 FOVS Gap Calibration

The data resulting from this test can provide information regarding the force to voltage change between the proof mass and the sensor head, what shape the response curve will take when the proof mass travels along the hypo tube, and can provide information as to a suitable F/C setting on the SCU.

Data resulting from setting the gap between the proof mass and the sensor head to the maximum opening is shown in figure 5.14. This trace shows the response of the sensor head in conjunction with the response of the index stage. A more useful presentation of this data is to plot the sensor head response to the change in gap, figure

5.15. The data is not as smooth as would be desired, but can be explained. First, the loading that is occurring is a result of a combination of the axial load due to the repelling action between the magnets and due to a moment loading. The moment loading could arises due to a combination of three sources. The first is the bending of the hypo-tube due to the proof mass moving along the length of the hypo tube due to either the tube being bent, or due to mis-alignment due to assembly tolerances. A second possible source for the bending moment is that the faces between the two repelling magnets are not parallel. An angle between the two gaps would cause the sensor head and proof

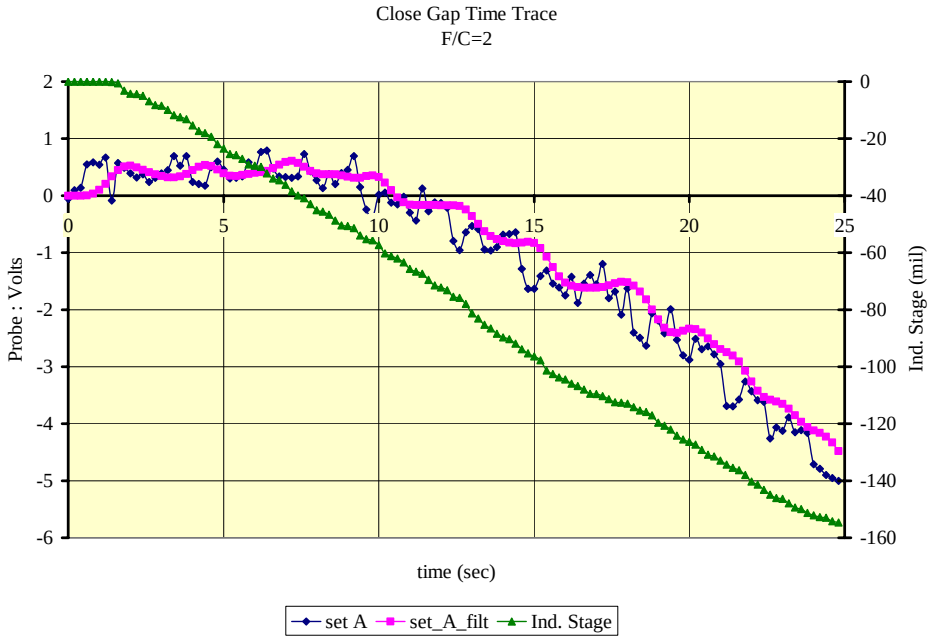

Figure 5.14 FOVS Raw Gap Calibration Data

mass to want to rotate which would result in a bending moment to be applied to the hypo tube. The ability for the FFPI to observe a moment load is quite possible as the FFPI is

most likely not along the central axis of the hypo tube, figure 3.7, and the hypo tube is not likely along the center of the sensor head and anchor. This indicates that the stress developed in the tube can be defined as

$$\sigma = \frac{P}{A} \pm \frac{Mc}{I} \tag{5.1}$$

where P is the axial load on the tube, A is the cross-sectional area of the tube, M is the bending moment on the tube, c is the distance from the center of the tube to the FFPI, and I is the area moment of inertia of the hypo tube. Note that if the bending moment results in a negative moment, it can offset the contribution of the axial loading, figure 5.1. Recall that the magnets are set in a repelling configuration which results in the axial load on the hypo-tube to be a tensile load and that the degree of loading increases as the gap closes. To determine whether the hypo-tube is bent, and to determine the alignment error the sensor would need to be dismantled. However, to do this might have resulted in damage to the FFPI. Since there was no longer access to additional fibers, the risk of disassembly was to great.

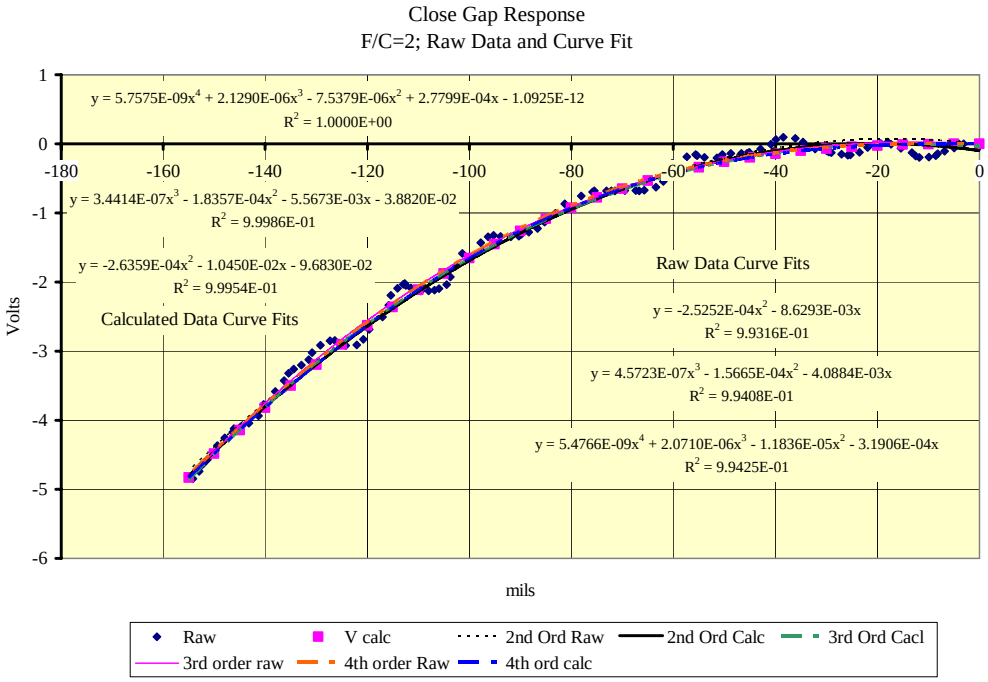

Figure 5.15 FOVS Gap Curve Fit

The data described as V_{calc} is produced by generating coefficients for a 4th order polynomial. This curve smoothes the data so that it can be converted to its third form which relates the force developed to the change in gap. This curve is useful as the slope can be used to determine the stiffness to the equilibrium position of the proof mass. This value can then be used along with the mass of the proof mass to determine the linear natural frequency of the proof mass. Figure 5.15 also shows a number of curve fits ranging from a 2nd order to a 4th order fit as well as the corresponding COD (coefficient of determination). The use of a 4th order polynomial was selected as the worst case scenario. The lower the order of polynomial required to generate suitable response behavior, the more efficient the response can be calculated. Also, the selection of the

order of the polynomial can also be selected on the range of motion that the proof mass may undergo. That is, if the relative motion between the proof mass and the sensor head is small, less than 10 mils (0.25 mm) 0-Pk, then the 2nd order of even a linear approximation could be applied. However, if the proof mass undergoes large motion, greater than 20 mils (0.5 mm) 0-Pk, then the 4th order polynomial would be suited best.

The next step is to adjust the plot to represent the motion of the proof mass about its equilibrium point, which is about 77 mils (1.96 mm). This motion is demonstrated in figure 5.16. This figure is helpful in that it demonstrates that as the gap between the proof mass and sensor head increases, the relative voltage change is less than a corresponding closing of the gap. Also, by applying the equation 3.19 from Section 3 that relates the voltage response to the applied load allows for a force versus gap change plot to be obtained. This conversion is useful in that it can provide information regarding the stiffness between the proof mass and the sensor head, figure 5.17. The slope of the curve at the equilibrium point will yield a stiffness value that can be used to determine the approximate natural frequency of the proof mass, figure 5.17.

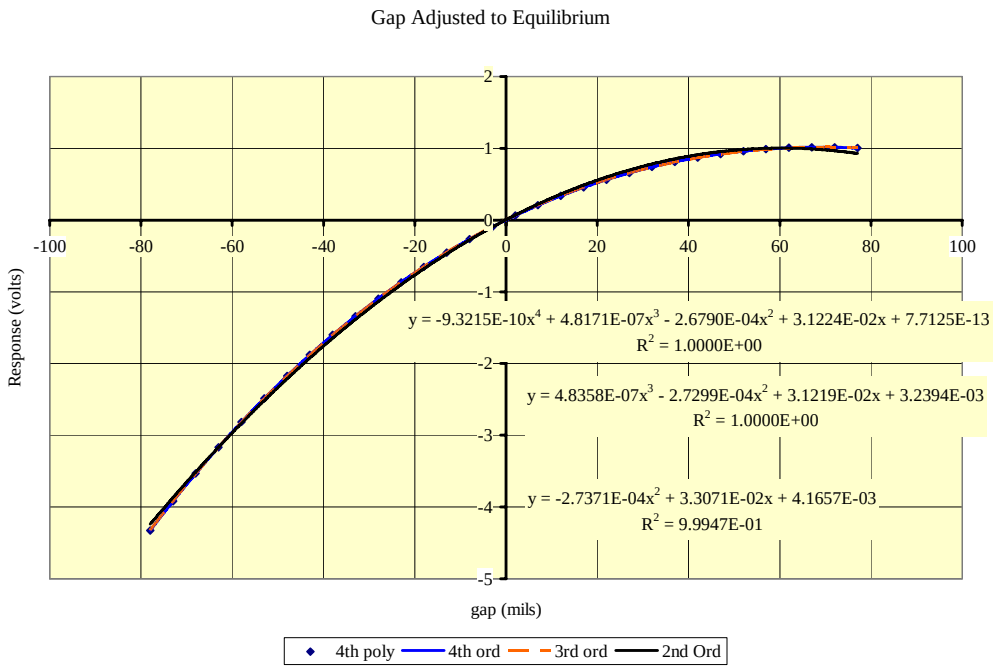

Figure 5.16 FOVS Gap Adjusted to Equilibrium

Although the force axis ranges from a positive force to a negative force the sign change is not indicative of the change of direction of the force. What it does indicate is an increase in tension, negative sign, and a decrease in tension, positive sign. Examination of the polynomials from the curve fit in figure 5.17 show that the first derivative at gap setting of zero yield stiffness values shown in Table 5-1. The proof mass is 0.0264 lbs (12 grams) which results in an undamped natural frequency around 32.5 Hz. This value

Table 5-1 Proof Mass Stiffness

Polynomial Order	Slope at zero gap (lbs/mil)	Lbs/in.	Nat Freq (Hz)
4^{th}	1.414E-03	1.414	32.4
3^{rd}	1.413E-03	1.413	32.4
2^{nd}	1.497E-03	1.497	33

for the natural frequency will help in defining test parameters for the shake table testing. Figure 5.18 shows a plot of the natural frequency of the FOVS related to the change in the existing gap. The initial natural frequency of the FOVS was to be 10 Hz. The

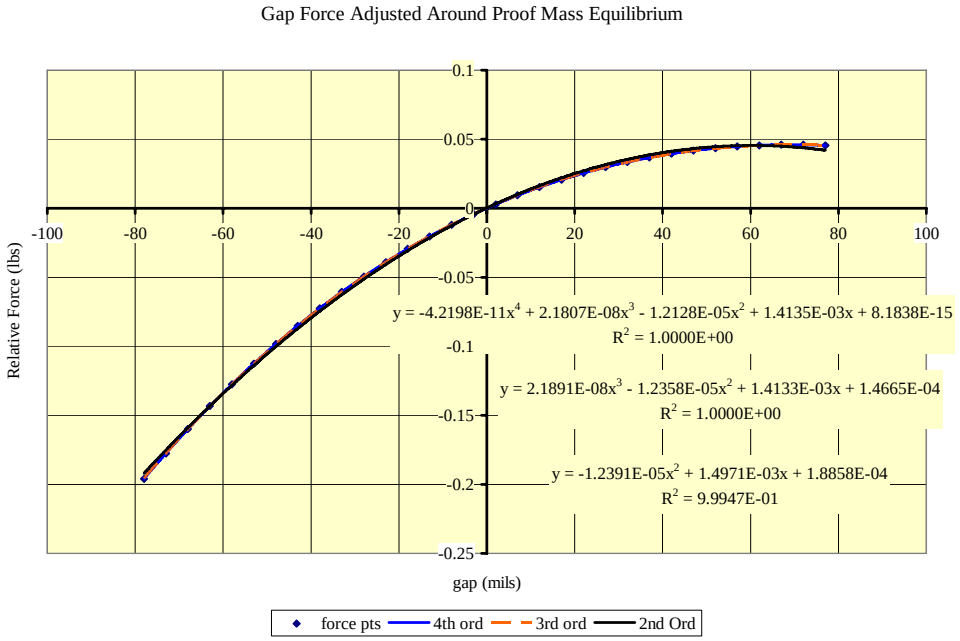

Figure 5.17 FOVS Relative Force Versus Gap Relation

initial force vs. gap relation was based on preliminary data from the FOGS response so it did not reflect the actual FOVS system. Also, from figure 5.18, if the equilibrium gap was widen by 0.06 in. (1.52 mm) then the natural frequency would be close to 10 Hz. The assembly of the FOVS involved holding the proof mass close to the top of the sensor (recall there is a set of repelling magnets at this end too) while attaching the sensor head to the end of the hypo-tube. The sensor head is attached using

cyanoacrylate (super glue) which cures quickly so not setting the proper gap correctly was very easy to do.

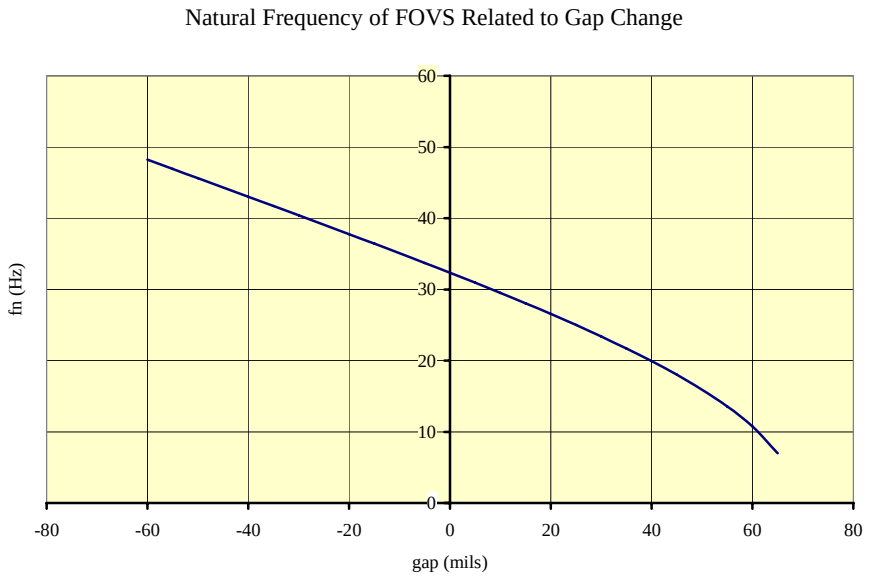

Figure 5.18 FOVS Natural Frequency to Gap

5.3.3 FOVS Dynamic Testing

The dynamic testing of the FOVS involves three tests. The first test is to observe what the natural response of the proof mass is by displacing the proof mass by flicking it. The second test is to subject the FOVS to a series of excitations over a range that emulates the theoretical responses covered in Section 3. The final test is to subject the FOVS to the vibrations from a demonstration rotor test stand.

5.3.3.1 Free Response Test: Flick Response

The proof mass of the FOVS was displaced and then released allowing it to under go a free vibration response. Data from this type of test will allow for three

observations to be made. First, the damped natural frequency can be observed, second the damping value can be estimated along with the possible mode of damping, and the relative shape of the time waveform for different extremes of relative motion between the proof mass and the sensor head.

The data was collected over a four second time span with a number of flicks made. The term flick is used as the method of displacing the proof mass was to catch the top with a finger nail, and then flick it downward. Figure 5.19 shows a sample of the raw time trace. The time trace shows six full responses. Negative response values correspond to the proof mass moving toward the sensor head of the FOVS. The initial gradual downward response is the initial flick. The high value negative spikes is the proof mass experiencing a large rebound until it reaches a point where an apparently sinusoidal decay occurs. This is the region of the response that will yield the most useful information. For this reason, the time trace is then parsed so that only the desired regions are examined.

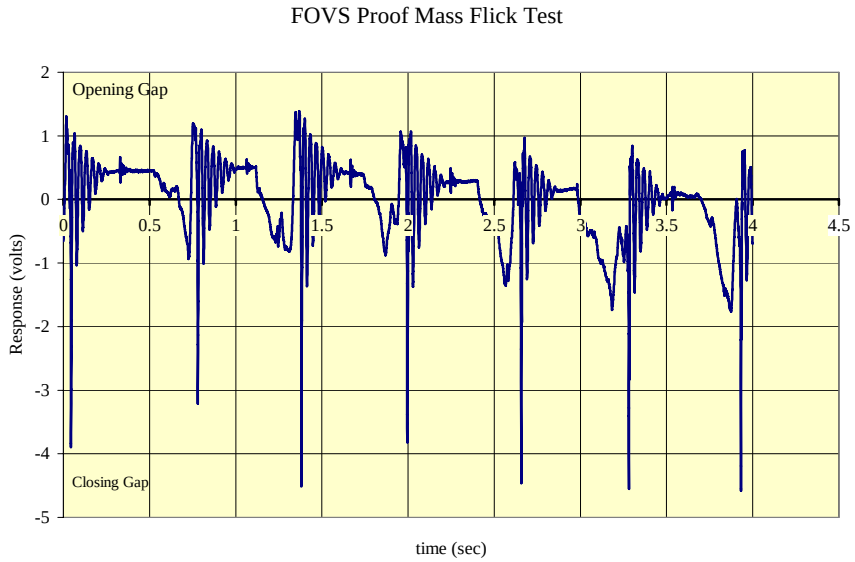

Figure 5.19 Flick Response: Raw Time Waveform

Figure 5.20(a) shows the above time trace reduced by setting a threshold point and collecting a set number of points to capture each response and setting each to a common time scale. Parsing the time set and then applying an appropriate number of zero pads to the time set will allow for a smoother analysis of the time response utilizing a Fourier transform to identify the dominant harmonic components. Inspection of the collected time responses does show that each parsed time response have similar shapes and occurrences. The gap calibration responses obtained from the static test can then be used to correlate the observed voltage to an observed gap motion, or relative motion between the proof mass and the sensor head, figure 5.20(b). One result of this conversion is that the roles of the ordinal extremes are reversed. That is, the positive values of figure 5.20(b) are indicative of the proof mass moving toward the sensor head and negative indicates moving away from the sensor head. Also, these measures are taken from the equilibrium point of the proof mass. By taking the average of these time traces, a single time waveform can be obtained that can be analyzed to get a generalized idea as to how the system is responding, figure 5.21.

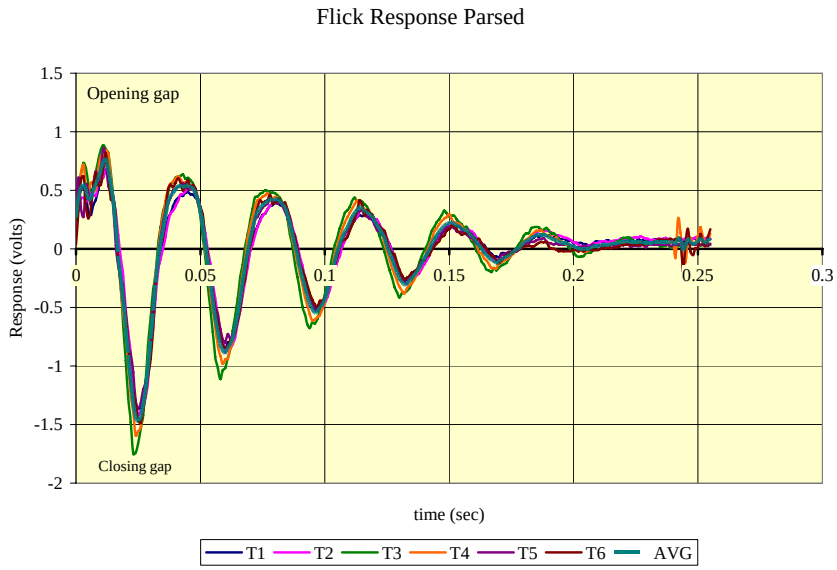

(a) Parsed time waveforms

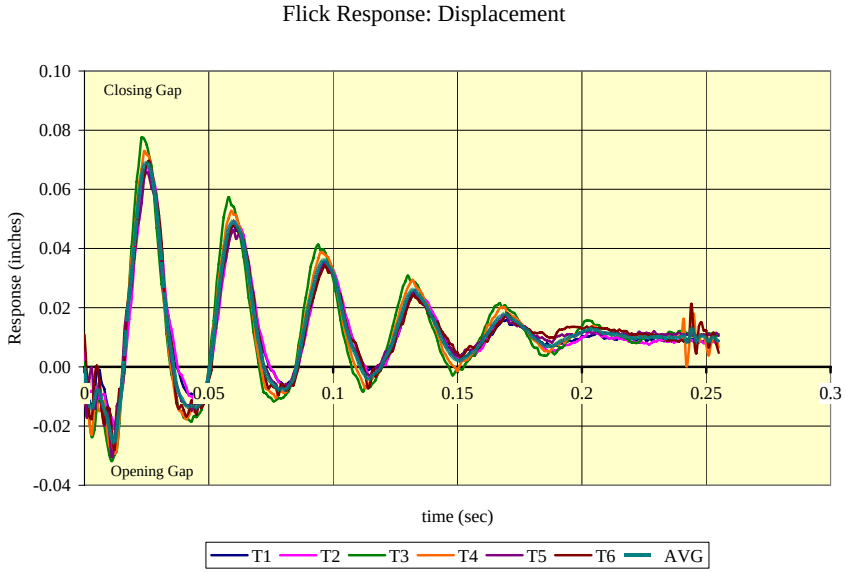

(b) Parsed relative motion time waveforms

Figure 5.20 Parsed Flick Time Waveforms

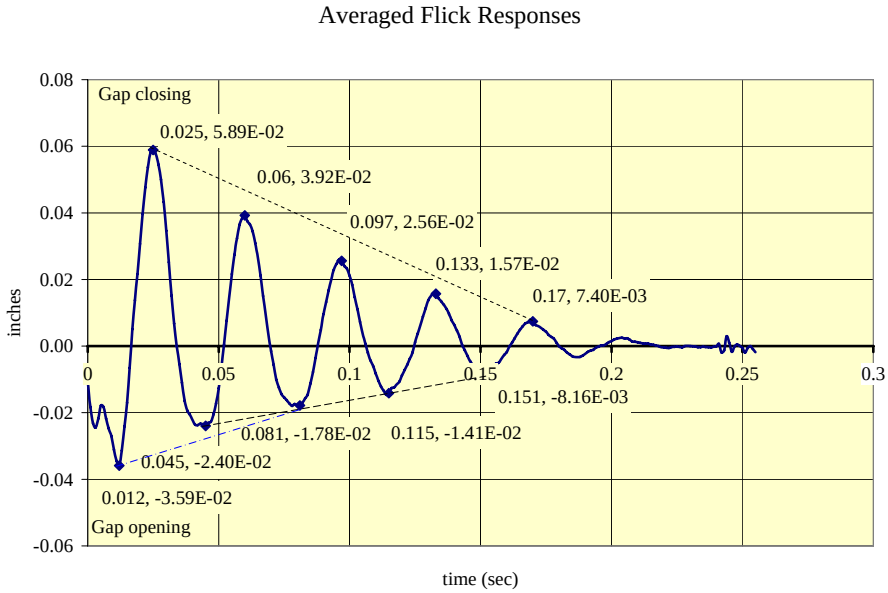

Figure 5.21 Averaged Flick Response

Table 5-2 Flick Response Results

	t (sec)	P (in)	log dec	ζ	T (sec)	fd (Hz)	fn (Hz)
+P1	0.025	0.0589					
+P2	0.06	0.0392	0.407	**0.064**	0.035	**28.57**	28.63
+P3	0.097	0.0256	0.426	**0.067**	0.037	**27.03**	27.09
+P4	0.133	0.0157	0.488	**0.077**	0.036	**27.78**	27.86
+P5	0.17	0.0074	0.752	**0.12**	0.037	**27.03**	27.22
-P1	0.012	0.0359					
-P2	0.045	0.024	0.402	**0.063**	0.033	**30.30**	30.361
-P3	0.081	0.01782	0.297	**0.047**	0.036	**27.78**	27.81
-P4	0.115	0.01412	0.232	**0.037**	0.034	**29.41**	29.43
-P5	0.151	0.00816	0.548	**0.086**	0.036	**27.78**	27.88

Table 5-2 shows the resulting damping ratio obtained from looking at adjoining positive peaks and adjoining negative peaks. Additional analysis includes the resulting period, damped natural frequency, and the resulting undamped natural frequency. The average damping value from observing the first the values from the positive peaks is

0.069. The last damping value, 0.12, was not factored into this average as the mode of damping appears to change for very low amplitudes of motion. This jump in damping can also be observed by looking at the last value for the negative peaks. Also, by observing the dotted line on the gap closing side of figure 5.21 the peaks do not touch the line. This can be an indication of a viscous type of damping. The average damping value for the negative peaks is harder to discern as the damping values vary widely. An explanation to the disparity is that the proof mass experiences a different form of damping while the gap closes than when it opens. That is, there is a point while the gap opens where the proof mass is forced to rub against either the housing or hypo-tube. The periods resulting from looking at the time difference follow an interesting trend of increasing period as the amplitude of motion decreases. This is not too unexpected as it was shown in Section 3 that the natural frequency is dependent on the initial amplitude based on a non-linear response. However, the results do produce an average damped frequency of 28.2 Hz. Coupled with the low damping value of 0.07, the resulting undamped natural frequency is approximately 28.3 Hz. The theoretical natural frequency was targeted to be around 32 Hz. The difference could be attributed to the possibility that the equilibrium point used in the theoretical calculation is off and that the flick test causes the proof mass to travel slightly different than the travel used to obtain the stiffness curve. Applying a Fourier transform to the parsed flick responses yields the spectrum shown in figure 5.22. Here the peak response occurs at 28.1 Hz. There is a secondary hump around 56 Hz which is not unexpected as the flick responses are not symmetric and higher order responses are expected.

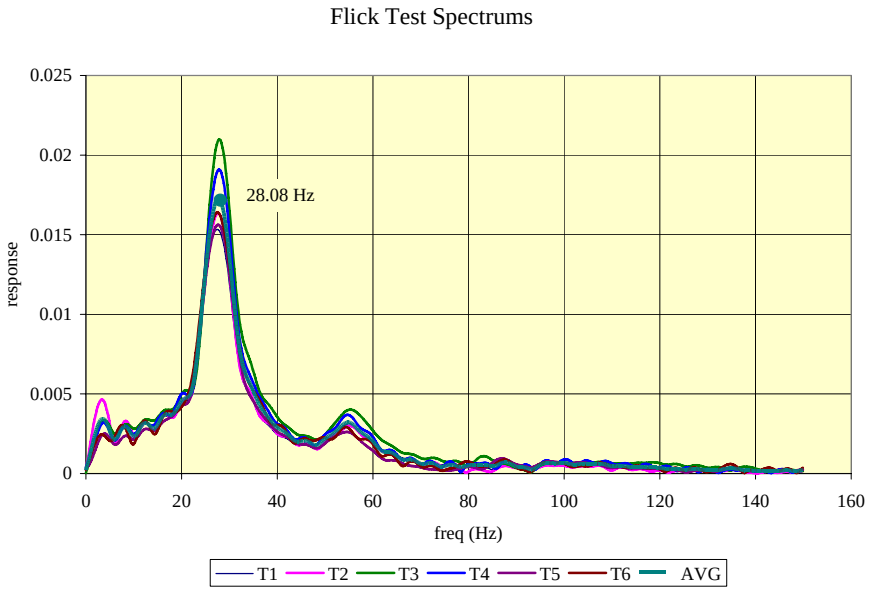

Figure 5.22 Spectrum of Flick Response

5.3.4 FOVS Shake Table Testing

Subjecting the FOVS to a controlled input and monitoring the response of the FOVS and the accelerometer built into the shake table (STA) will allow for the response characteristics of the FOVS to be established. There are three objectives in conducting these tests. The first is to characterize the response of the FOVS sensor around the natural frequency point, the second objective is to determine the response of the FOVS in the desired operating region and the corresponding calibration factor, and the third is to examine the response over a range of operation. The first discussion presented will be the determination of the overall general response of the sensor, the second discussion will examine the determination of the calibration factor, and the final discussion will be

on the overall response of the FOVS by including the time waveforms and the reference sensor.

5.3.5 Overall FOVS Response

The FOVS sensor is subjected to a Pk-Pk amplitude over a set frequency range and then a constant *g* level while stepping through a set of excitation frequencies. The excitation frequency range is from 25 Hz up to 100 Hz. The ability of the shake table to produce accurate amplitudes below 30 Hz decreases from 3% error to 10% error. But, it is possible to determine the peak response frequency of the FOVS sensor. This test will help confirm the results from the flick test as well demonstrate how the sensor will respond when the excitation frequency is above the natural frequency of the system.

Subjecting the FOVS sensor to two runs, one with a constant Pk-Pk displacement amplitude over a frequency range and the other a constant 0-Pk acceleration amplitude over the same frequency range, will help establish which frequency response model established in Section 3 will apply. The first test subjected the FOVS to a Pk-Pk amplitude of 10 mils (0.25 mm) over a frequency range of 25 Hz to 100 Hz. The resulting response is shown in figure 5.23(a). The response plots shown are obtained by applying a Fourier transform to the time waveforms and tracking the response at the applied excitation frequency. The comparison sensor for this test was the accelerometer built into the shake table (STA). The ECP (eddy current probe) is not shown as the combined weight of the platform and of the FOVS limits the peak *g* load to 2*gs.* At 100 Hz, a 5 mil (0.125 mm) peak response generates a g-load of 5.18*g*. Since the applied 0-Pk amplitude is constant, the response of the STA is expected to follow a parabolic

curve since $a=X\omega^2$, where a is the acceleration, X is the 0-Pk amplitude, and ω is the excitation frequency in rad/s^2. Observation of the FOVS response shows that the peak response of the FOVS is around 30 *Hz* and that the response to the right of the peak response, 40 to 100 Hz, follows a trend similar to the STA. The second test, figure 5.23(b) shows the response when the FOVS is subjected to a constant acceleration amplitude of 0.75*g* over the frequency range of 19.5 *Hz* to 85 *Hz*. This response compares the response of the FOVS to the STA and to the ECP. The response of the STA is expected to follow a horizontal curve since the excitation is of constant acceleration amplitude. The STA has a stated calibration of 0.05 mv/g and the Labview Fast Fourier transform applies a $1/\sqrt{2}$ factor which would result in a response value of 0.0265 volts. However, the value observed for the linear curve fit is around 0.0261 volts as an average value with an average percent difference of 3.71. There are variations of the desired responses for each iteration to the observed responses. This is an indication that the calibration of the shake table may be off. The ECP is expected to follow a curve that is nearly the inverse of the STA shown in figure 23(a) since $x = a/\omega^2$. The FOVS response shows a peak response around 31.5 Hz. The difference in amplitude can be explained by two possibilities. The first possibility is that the response peak observed in figure 5.23(a) is due to an acceleration level of 0.45 *g's*, or about 60% of the level used in figure 5.23(b). The response models developed in Section 3 showed that the frequency of the sensor is a function of excitation amplitude. The second possibility is that the frequency increment, about 5 Hz, used to step through the tests may have resulted in missing the exact response level for each test.

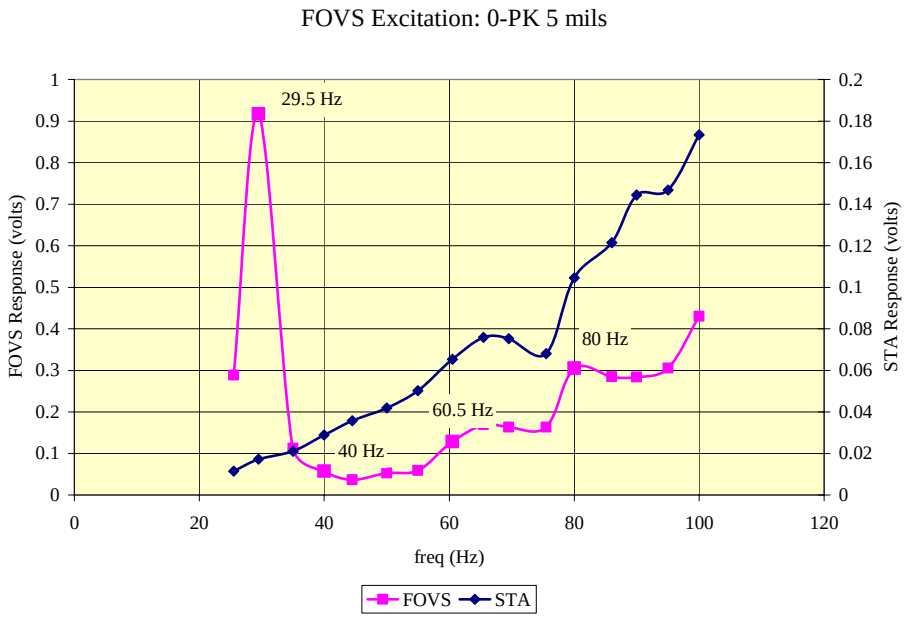

(a) 10 mil Pk-Pk Excitation

FOVS Response: 0.75*g* Excitation Level

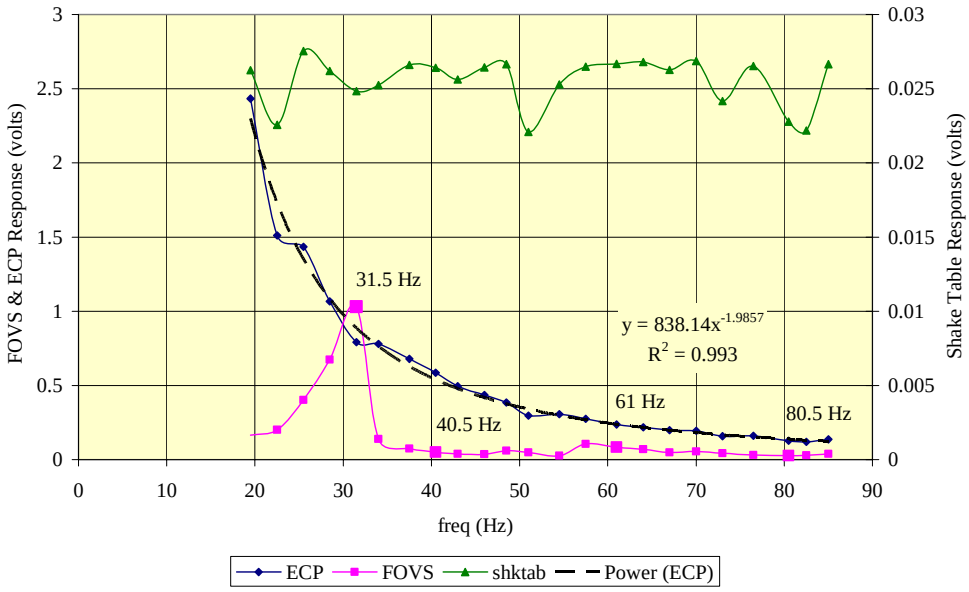

(b) 0.75 g 0-Pk Excitation

Figure 5.23 FOVS Response at 0.75 g

A way to characterize the response of the FOVS is to look at the ratio FOVS/STA. This ratio is useful if the responses of both sensors are related to acceleration. This derives as follows

$$g = \frac{V_{STA}}{C_{STA}} = \frac{V_{FOVS}}{C_{FOVS}} \rightarrow C_{FOVS} = C_{STA}\frac{V_{FOVS}}{V_{STA}} \tag{5.2}$$

where V_i is the voltage of the sensor, C_i is the calibration factor V/g for each sensor. Figure 5.24 shows the calibration factor curves for the two tests. The curves follow comparable trends to the right of the response peaks. These areas are emphasized by

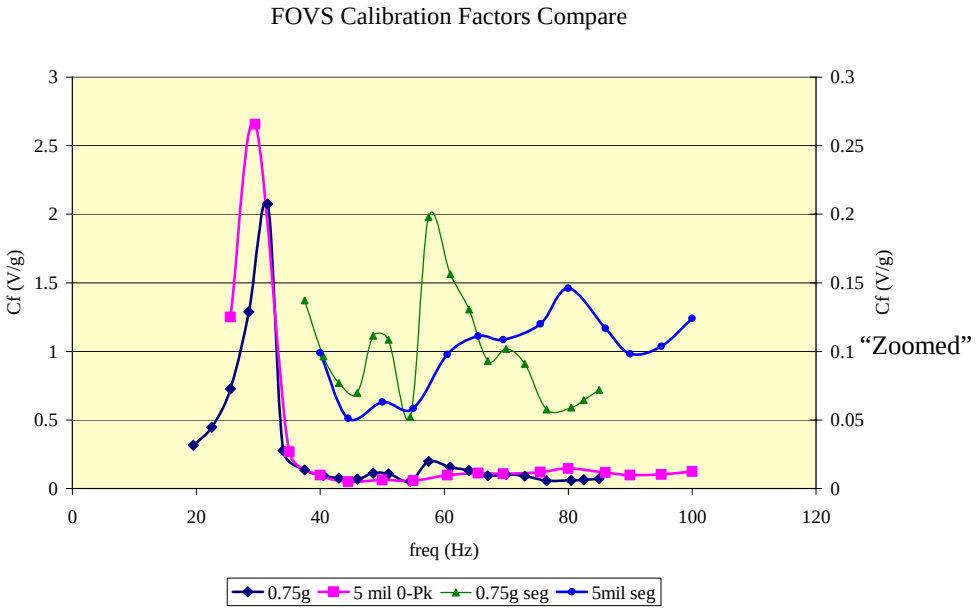

Figure 5.24 FOVS Calibration Curves

the data 0.75*g-seg* and 5*mil-seg*. These "zooms" display a wide variation for C_f with a mean value of 0.098 for the 0.75*g* and a mean value of 0.1 for the 5 mil-0-Pk. The average percent difference for each test is 0.00%. Obviously, these results shows some of the discrepancy between what a broad overview presents versus what is actually

happening. Figure 5.25 shows a cascade plot for each test. These figures show the spectrums for each successive test. Figure 5.25(a) shows the 0.75*g* excitation and that the spectrums are rich with components above the desired 1X excitation. This is a good indication that the time waveforms are distorted. The figure for the 0-Pk 5mil excitation displays a cleaner overall response. This is primarily due to the fact that the excitation at

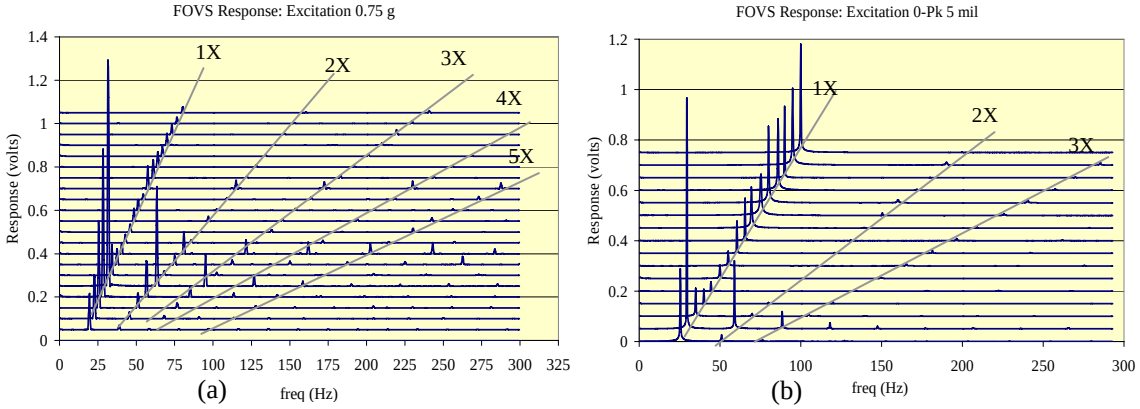

Figure 5.25 Cascade of FOVS for Two Tests

this level is 2 to 3 times higher than 0.75*g* excitation. To aid in understanding as to why there is such a discrepancy in response a study of the final construction of the FOVS and the resulting time waveforms is required.

The successful operation of the FOVS sensor relies on the unobstructed relative motion between the proof mass and the housing and hypo-tube. That is, no rubbing or bumping of the proof mass into the housing or, more importantly, with the hypo-tube occurs. Recall that the FFPI is housed within the hypo-tube. There are three factors that could account for the marginal response of the FOVS. The first factor is that the repelling of a body by a magnetic force with out any support or guides results in an

unstable body. There are six degrees of freedom for a levitated body. For the FOVS sensor, two degrees of freedom, translation along the hypo-tube, *z*, and rotation about the hypo-tube, θ_z, are permitted. The other four degrees, *x*, *y*, θ_x, and θ_y are constrained and the degree of constraint depends on the tolerances between the proof mass and the housing. Motion along the *x*, *y* and tilting about *x*, and *y* could result in the proof mass impacting the hypo-tube resulting in spurious signals to be generated and could hinder its motion. The second factor to look at is the clearance between the hypo-tube and the proof mass. The design intent was to allow for enough room for the proof mass to move over the hypo-tube without any contact with the hypo-tube. However, it is possible that the hypo-tube is bent and a rub occurs. Also, the bore on the proof mass required that it be drilled from both ends. A combination of the drill wandering off center and not boring exactly on center from either side could have resulted in a step, or bump, to be formed somewhere in the middle of the proof mass. That is, the bore of the proof mass does not follow the axial center of the proof mass. Again, the resulting eccentricity of the bore holes could result in the proof mass impacting the hypo-tube. Also, it is possible that both events occurred furthering comprising the clearance issue. Another factor that could occur is that the faces of the repelling magnets between the sensor head and proof mass are not perfectly parallel. This could result in a force distribution field that is not centered along the hypo-tube. The eccentric field would result in a moment loading of the sensor head onto the hypo-tube that again would result in a spurious vibration. Examination of the assembly issues would entail soaking the sensor in a debonding solution. This could have resulted in damage to the FFPI bonded with the

hypo-tube. Also, the fabrication of new FFPI and hypo-tube assembly was not feasible as the process for fabricating the FFPI was not available at the time as the equipment was under repair. Also, re-machining of the elements would have required access to a shop that has equipment with tighter machining tolerances and funds were not available to have the machining done.

Interpretation of the FOVS signal requires an understanding that the observed signal essentially reflects the relative motion of the hypo-tube, and hence the housing, relative to the proof mass. Figure 5.26 demonstrates the relative motion issue for a resonance case. A negative sign of the FOVS indicates that the gap between the sensor head and proof mass is decreasing while a positive sign indicates that the gap is opening. The ovals in figure 5.26 highlight points where there are possible contact issues between the proof mass and the hypo-tube. A change in value, in principle, should indicate that there is a change in the gap, and hence an increase in motion of the housing relative to the proof mass.

The data presented earlier in regards to the overall response was obtained by tracking the value of the response peak at the excitation frequency from the spectrum obtained from the time waveforms. Inspection of the time waveforms is required as the ability of a sensor to reproduce a clean time waveform is essential. However, as it will be shown, there are obvious issues with the FOVS in reproducing a time waveform due to systematic errors that can be attributed to the machining and stack tolerances discussed in the previous paragraph. Since the excitation source is assumed to be a sinusoidal at a single frequency the resulting time waveforms are expected to show a

sinusoidal response. Inspection of figures 5.27 through 5.30 will show that this is not the case with FOVS. The cases presented reflect the time waveform responses of the FOVS for similar excitation frequencies. The 0.75*g* case includes the reference ECP and STA while the 0-Pk 5 mil case only compares with the STA, due to the removal of the heavy target table used for the ECP.

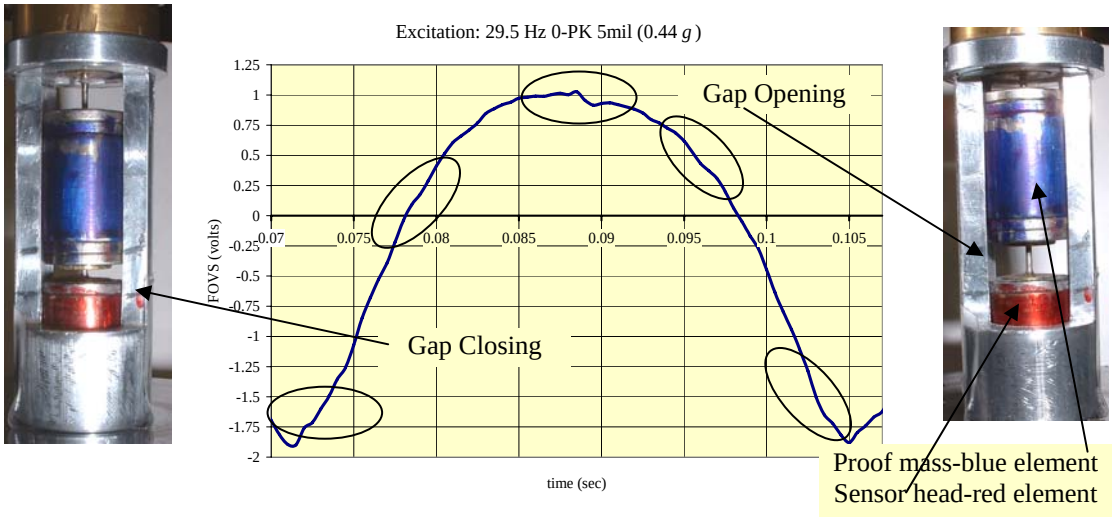

Figure 5.26 FOVS Response Related to Gap Change

The first case shown, figures 5.27 and 5.29 shows the response for the resonance case. The time waveforms for tests near the resonance point of the sensor do show that there are transitions going from the negative peak value, or maximum gap closure, toward the positive peak value, maximum gap opening, followed by some high frequency “ringing”. The corresponding spectrums show that the higher harmonics are present. In successive figures of increasing excitation frequency, the overall amplitudes of the FOVS response decrease as expected but the time waveforms do not display a

singular excitation frequency. For the 0.75*g* case, each successive increase in excitation frequency resulted in a decrease in 0-Pk amplitude. This resulted in the time waveforms to reflect that the sensing assembly is most likely responding to spurious effects from the proof mass traveling over the possible bump between it and the hypo-tube. Also, it is possible that these time waveforms reflect that the sensing head experiences spurious motions.

In contrast, the 0-Pk 5 mil (0.127 mm) case demonstrates the response of the FOVS as the *g*-level increases. The resonance case observed displays a similar time trace to that of the 0.75*g* case. Excitation levels above this point are of greater interest. At 40 Hz excitation, the observed time waveform does have a better resemblance of a sinusoidal wave than its counterpart of the 0.75*g* excitation. However, there is a bit of noise within the signal. The *g* level, 0.82*g*, in this case is 12% higher than the 0.75*g* case. This indicates that there may be a *g* level that can overcome the hindrance between the proof mass and hypo-tube. The next two cases, 60 and 80 Hz, both display time waveforms that appear to be fairly "clean" (no sharp spikes or discontinuities) with spectrums that exhibit predominately a single excitation frequency. Observation of the occurrence of the peaks also shows that the response is nearly 180^0 out of phase from the accelerometer response. This is an indication that at this level the FOVS is acting as a seismometer.

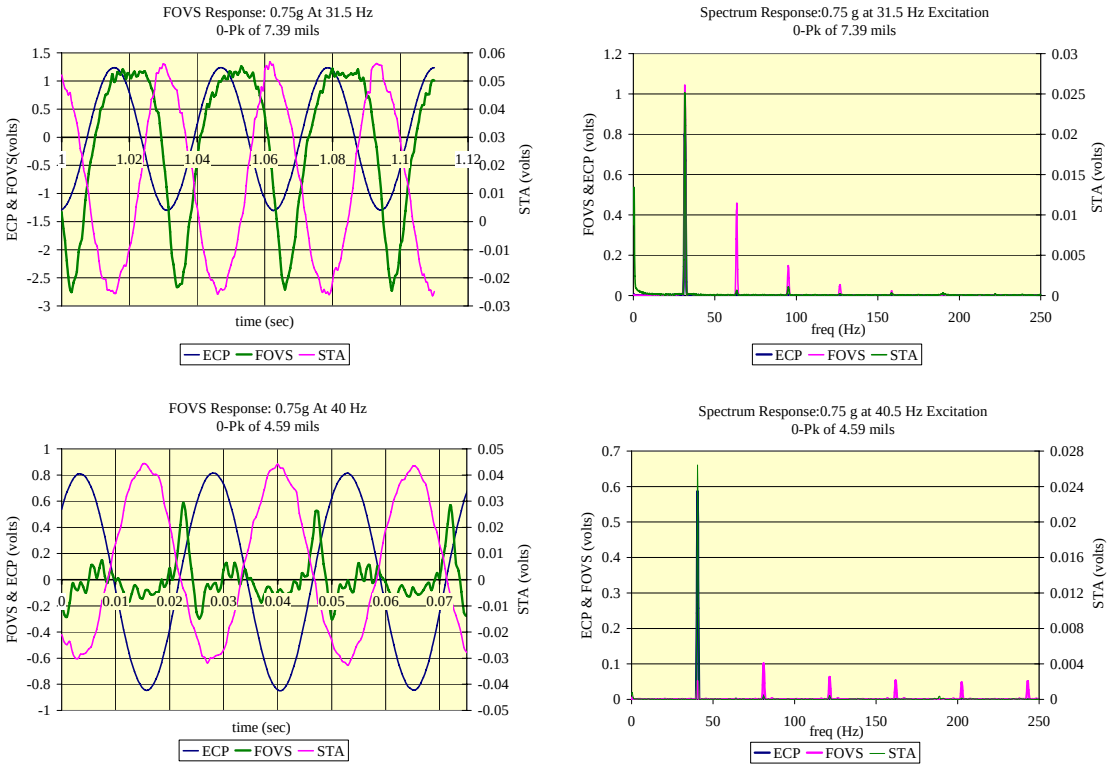

Figure 5.27 FOVS Response 0-Pk 0.75g (Set A)

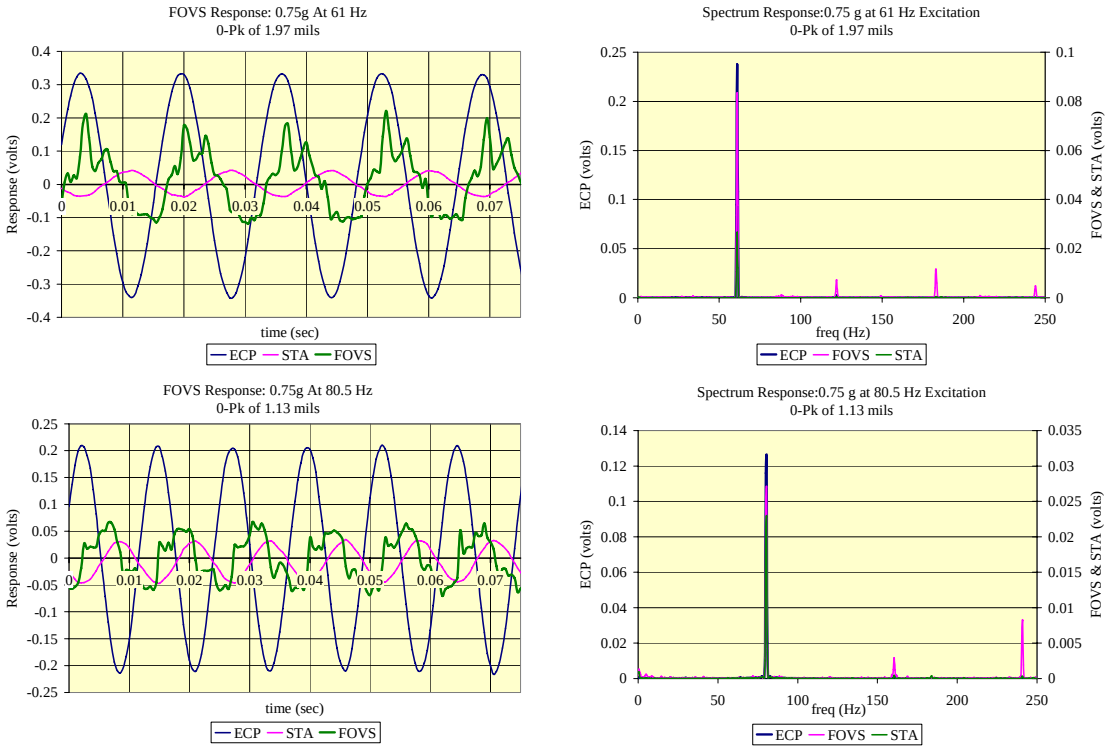

Figure 5.28 FOVS Response 0-Pk 0.75 g (Set B)

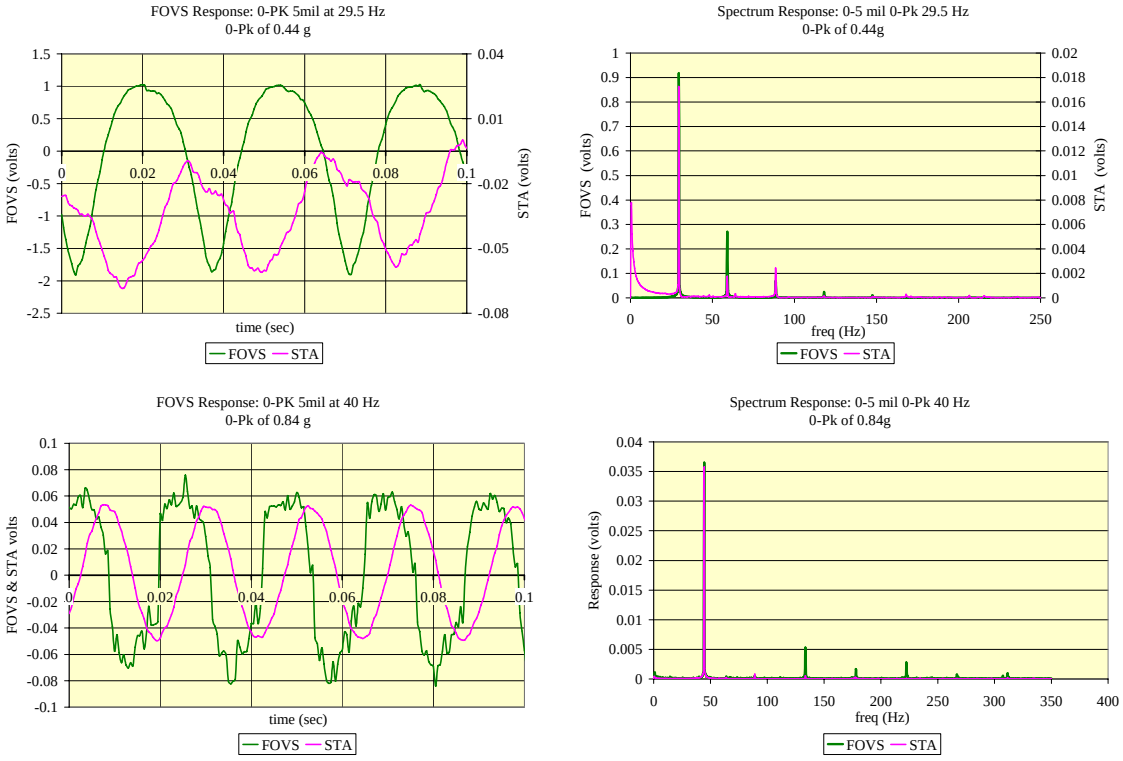

Figure 5.29 FOVS Response 0-PK 5 mil (Set A)

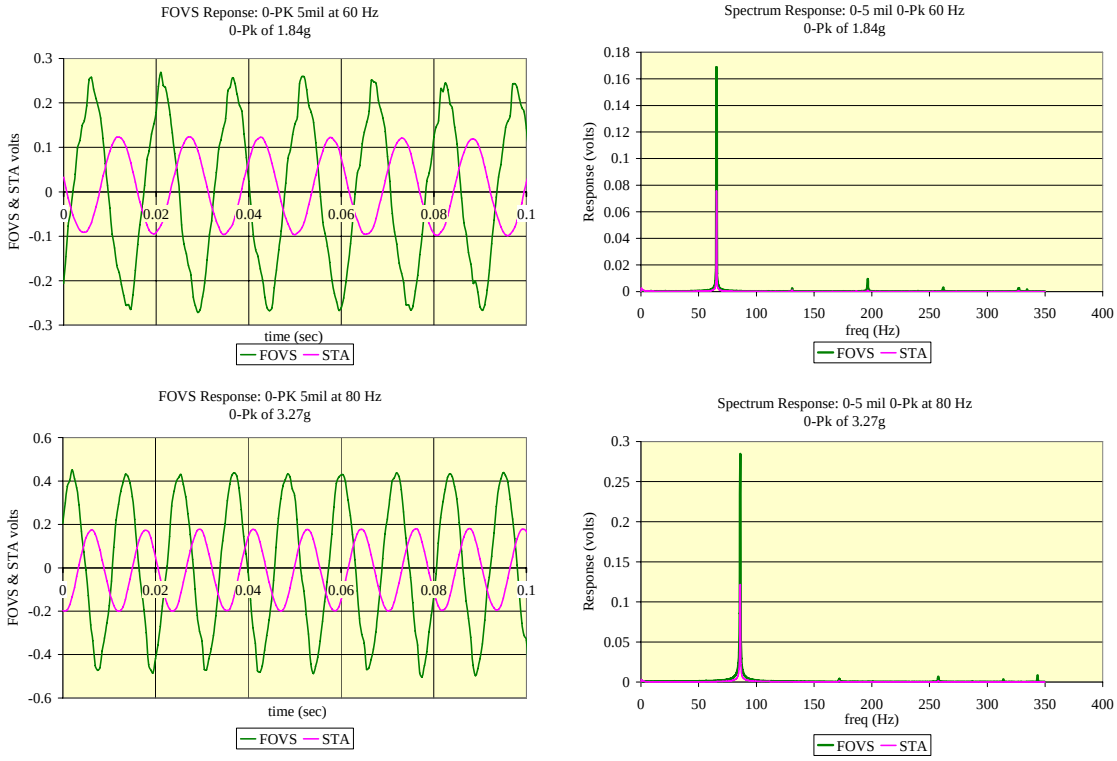

Figure 5.30 FOVS Response 0-Pk 5 mil (Set B)

One last item to address in regards to the time waveforms shown in figures 5.27 to 5.30 is the observed phase. The response of the FOVS does lag the accelerometer response. The degree to which the lag occurs is difficult to establish since there are points where the relative motion between the proof mass and sensor head causes the gap change to be delayed. Then, once a sufficient acceleration is applied, the gap change is sudden causing a spike to occur. The time traces in figure 5.30 yield the best case for establishing the observed phase difference between the shake table accelerometer (STA) and the FOVS response. The figures indicate that the mean phase is about 200^0. The expected phase is around 180^0. The 20^0 difference could be attributed to a frictional lag.

5.3.5.1 Response Prediction

The models presented in Section 3 combined with the static calibration and flick data presented does allow for the overall response of the sensor to be approximated. Figure 5.31 displays the experimental response plot for the 0.75*g* test case and the theoretical response plot. The traces do show an overall good agreement in estimating the predicating the peak response level, in volts, as well as the shape of the resonance response hill. The fit on the right side of the curve is of the same magnitude, but the experimental response levels appear to be higher. This is possibly due to the presence of additional harmonics such as the sensor head moving, the proof mass rocking, and other spurious influences.

The response models presented in Section 3 also indicated that the peak response point is a function of excitation amplitude. Figure 5.32 shows the results from conducting tests at five different *g* excitation levels from 27 to 41 Hz. The figure shows that as the excitation levels increase, the peak response frequencies shift to the right as demonstrated in figure 3.21. A limitation in the viewed data is that the incremental frequency step was 2 Hz. Setting the frequency steps of the shake table to 1 Hz increments is tricky as it has a ±0.5 Hz error. Subjecting the FOVS sensor to a frequency sweeping excitation would allow for a more accurate measure of the peak response point. Determination of the peak response point is critical as this sets the boundary for what excitation level the sensor would be useful at. If the peak response of the sensor is around 31 Hz, then the frequency point where it could be implemented would be around 70 Hz as a seismic accelerometer.

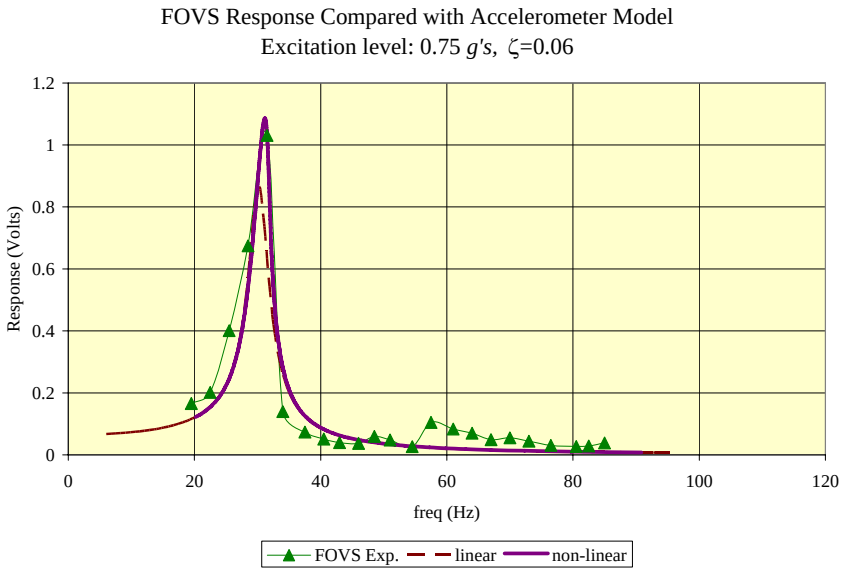

Figure 5.31 Comparison of FOVS Experimental

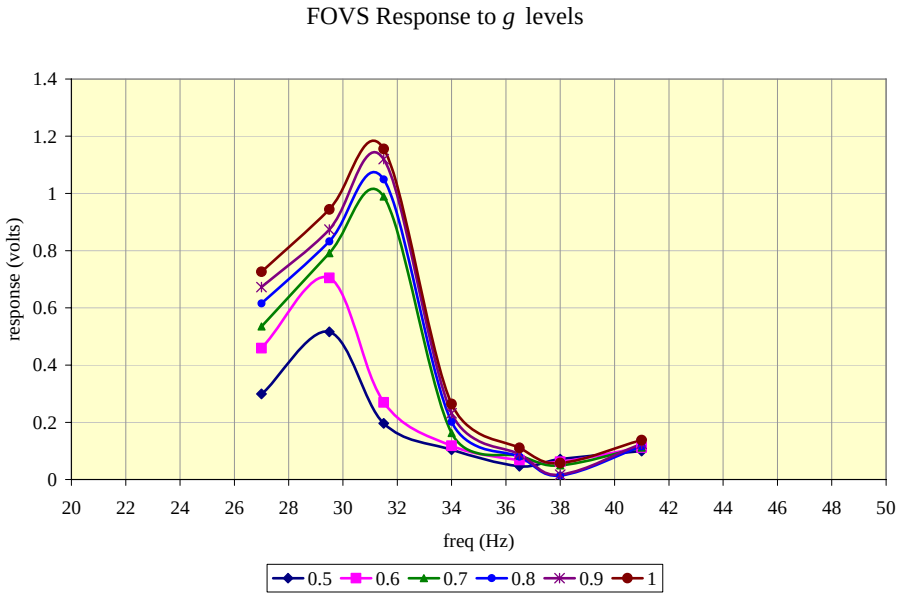

Figure 5.32 FOVS Jump Response

5.4 Response of Sensors to Rotor Excitations

Demonstration of the FOGS and FOVS sensor to an actual application will be demonstrated by utilizing a demo rotor, figure 5.33. Although the demo rotor is a simplified mock up of an actual machine it is capable of providing vibrational scenarios that emulate an actual machine. That is, although the machine may operate at a constant speed, the resulting vibrations are not a singular vibration due to the interaction of all the assembled components, thus the sensors are subjected to many different vibrations. The intent of this test is to demonstrate the capability of the FOGS and FOVS to sense machine vibrations.

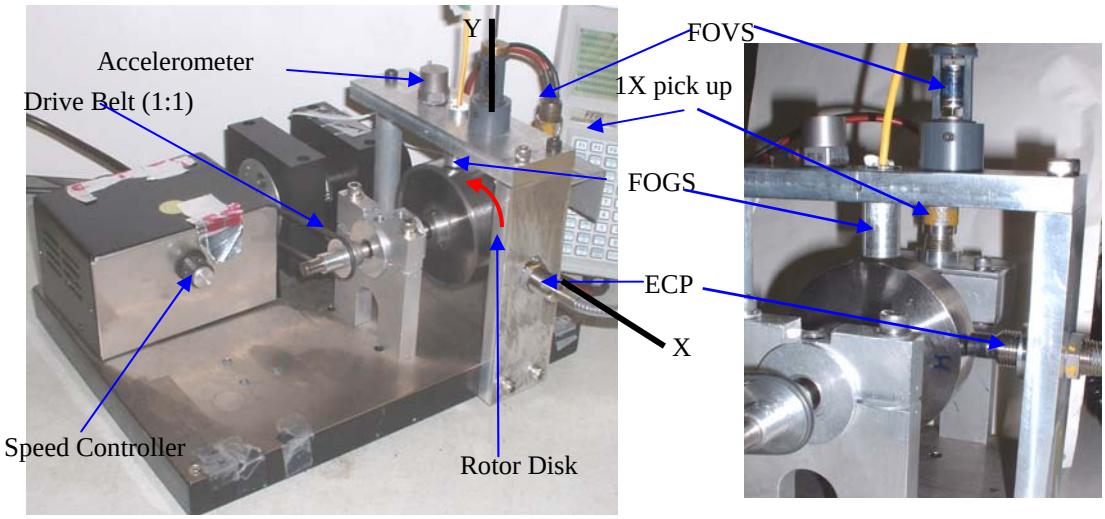

Figure 5.33 Demo Rotor Test Stand

The wide spectrum of possible vibrations is of concern as the developed sensors were designed (as a first cut prototype) for one particular axis of operation and are susceptible to transverse excitations. As an example, the FOGS sensor is configured such that it is responsive along the axis of the hypo tube that supports the sensor head. However, the configuration does a minimal job in suppressing the transverse sensitivity as the sensor head can impact the housing and is susceptible to moment loading too. This is important as the FOGS in the proximity of the rotating surface of the rotor disk is subjected to the radial displacement as well as the transverse motion of the rotor face. The transverse motion of the rotor surface past the sensor head results in a drag force that acts on the sensor head toward the housing. Also, the rotor face may not be true such that it is susceptible to a wobble. This wobble could cause the gap to not be uniform which could result in the resultant magnetic load to act off axis of the hypo-tube and induce a resultant moment load. Figure 5.34 demonstrates the three sources of transverse vibrations mentioned above.

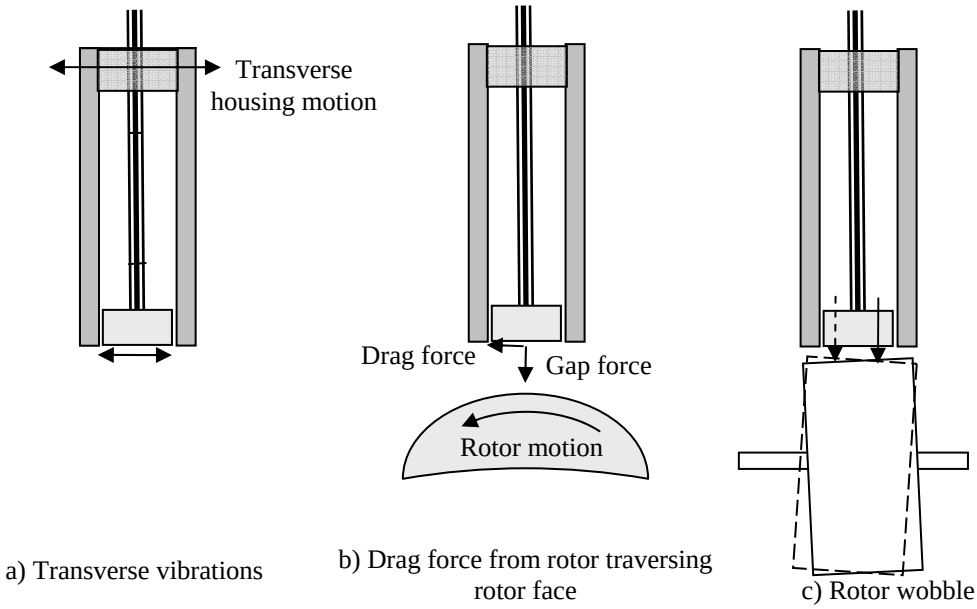

Figure 5.34 Transverse Excitation Sources of FOGS

5.4.1 Rotor Test with No "Defects"

The preliminary rotor test was conducted with the rotor as is with no purposefully introduced defects. These tests were conducted at various operating speeds as a means to demonstrate the response of the sensors for different excitation levels. The diameter of the rotor disk is 3.25 in. (82.6 mm) and the rate at which the surface of the rotor passes each gap sensor can range from 20.4 in/s (1.16 kmh) at an operating speed of 2 Hz to 510 in/s (47.0 kmh) at 50 Hz. The response of the gap sensors will result in the gap changing primarily due to the mechanical run-out resulting from alignment and assembly. To gage what the initial reading of the gap sensors could be, a dial indicator is used to determine what the overall peak to peak displacement would be. This test is conducted so that only the mechanical run-out would be observed. The "at speed" tests

would result in minimally different values as the eccentricity of the rotor disk will result in the shaft flexing due to the centripetal force of the rotor. Figure 5.35 shows the dial indicator and the Pk-Pk value of the mechanical run-out of the rotor disk. By comparing

Figure 5.35 Dial Indicator on Rotor

the peak-peak motion observed by the two gap sensors at low speeds to the reading observed on the dial indicator will allow for a means for a measure of the application of the calibration factors obtained from the dynamic and static tests previously conducted.

5.4.2 Unmodified Rotor at Speed

The tests to demonstrate the response of the sensors at different operating speeds will be done at 2, 20, and 40 Hz. Each test will look at the comparison of the time waveforms of the respective sensors, i.e. FOGS sensor to ECP sensor and FOVS to accelerometer, the spectrums, and the resulting orbit from the gap sensors. Since the dial indicator shows that the peak to peak motion is less than 10 mils (0.254 mm), the FOGS

calibration will apply both the full fourth order quadratic expression as well as the linear calibration factor.

The time waveforms shown in figure 5.36(a) show the responses of the ECP and FOGS probe when the rotor is turning at 2 Hz (120 rpm). This baseline response shows that the ECP is responding to some anomaly that occurs primarily along the X-axis of the rotor. The large symbols on each time trace represents the 1X timing mark of the rotor. The FOGS trace would show a corresponding hump if it could react to it. Inspection of the rotor surface does not show any indication of any noticeable damage or other defect. Comparing the two time traces shows that the peak-peak response are comparable and the difference observed could be attributed to a stack error of the rotor parts. The average values observed for each sensor in table 5-3 are comparable to the reading from the dial indicator of 2.75 mils (69.8 μm), and are in good agreement with each other. The value of 2.75 mils (69.8 μm) is an approximate reading as the dial gage can only read down to 1 mil (25 μm), and the initial zero setting of the dial face may have been off by some too. A curious result of the data shown in table 5-3 is that the

Table 5-3 Peak Responses for FOGS and ECP at 2 Hz

ECP		
max (mils)	min (mils)	pk-pk (mils)
1.47	-1.13	2.6
1.38	-1.22	2.6
1.4	-1.16	2.56
1.42	-1.25	2.67
	Avg =2.61 (mils)	

FOGS		
max (mils)	min (mils)	pk-pk (mils)
1.37	-1.35	2.72
1.31	-1.35	2.66
1.25	-1.36	2.61
1.27	-1.36	2.63
	Avg =2.66 (mils)	

ECP and FOGS do not register the same positive and negative peak values, but the total peak to peak values are comparable. An explanation for this might be due to the gap setting of the FOGS. Recall the scheme in Section 3 to transform the FOGS signal into a gap measurement requires that the initial gap be used to determine a reference voltage that is summed with the observed voltage signal. This summed voltage value is then used to determine the overall gap value from the gap calibration curve. Then, to get the relative gap value, the initial gap value is subtracted. If the actual gap of the FOGS is off by a few mils, an offset will occur. The difference in gap measure can be due to how tight or loose the gap is gauged using the plastic feeler gages plus accounting for the protuberance of the sensor head. Examination of the two tests at 20 Hz (1200 rpm) and 40 Hz (2400 rpm) show that the relative Pk-Pk values do not change by an appreciable amount, the general shape of the time waveforms are similar to the 2 Hz test. One noticeable feature of the two at speed tests for the FOGS response is the added high frequency components.

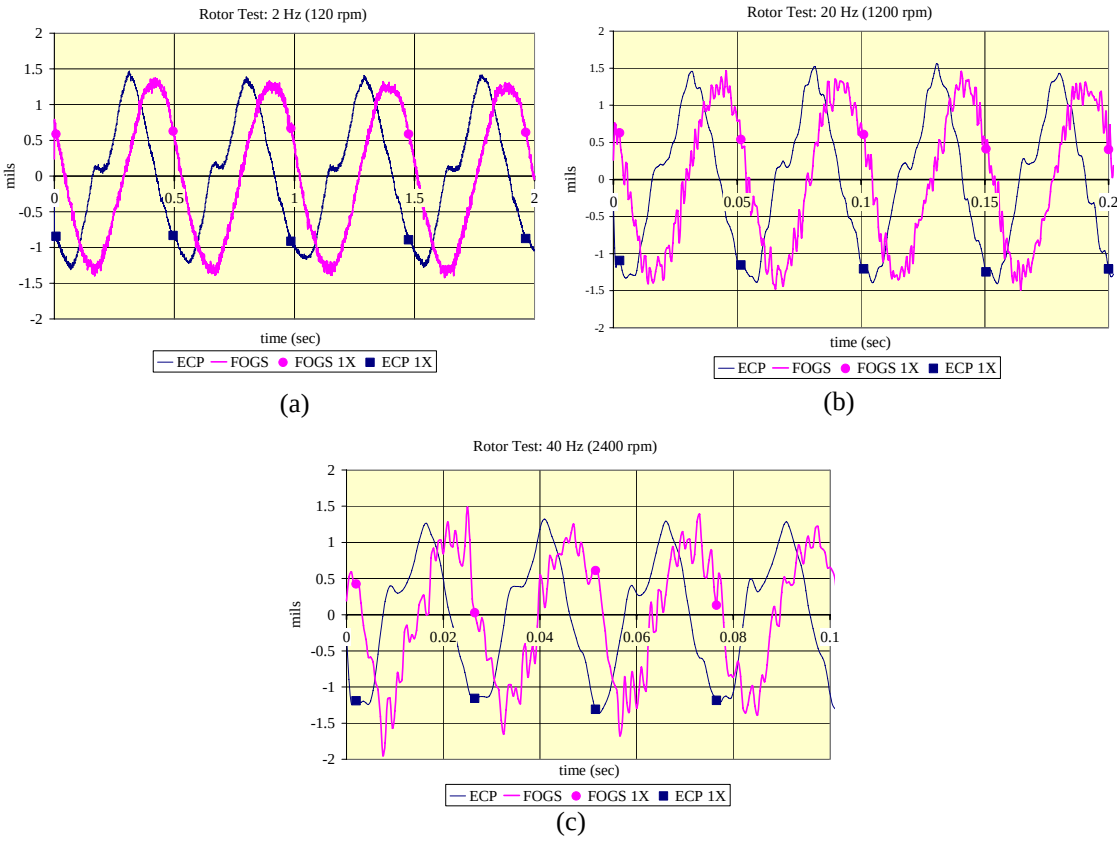

Figure 5.36 Rotor Test: ECP and FOGS Time Waveforms

These components can be attributed to the existence of the possible transverse components discussed previously. In addition, these higher components of the FOGS make producing tables similar to table 5-3 for the 2 Hz run difficult as extracting the peak and valleys values would require either an eyeball approximation or filtering of the time waveforms. Plotting the X-axis response, ECP results, versus the Y-axis response, FOGS results, results in an orbit plot. This orbit plot provides insight into the radial motion of the rotor disk. Figure 5.37 shows the orbits for the 2, 20, and 40 Hz tests. The data shown are for unfiltered results. The plots of the symbol indicate where the 1X

trigger is located in relation to other events in the orbit and the arrow indicates direction of rotor rotation. These figures show that the shape and relative Pk-Pk motion remains consistent from test to test. Again, the 20 Hz and 40 Hz orbit plots are not compensated for runout. The intent of these figures is to show that the FOGS is capable of responding consistently across a range of testing speeds. Figure 5.38 shows the same orbits when a low pass filter is not and is applied. With the removal of the higher frequency elements, and with the orbits over laid the subtle difference between the 2 Hz and the 20 and 40 Hz speeds can be observed.

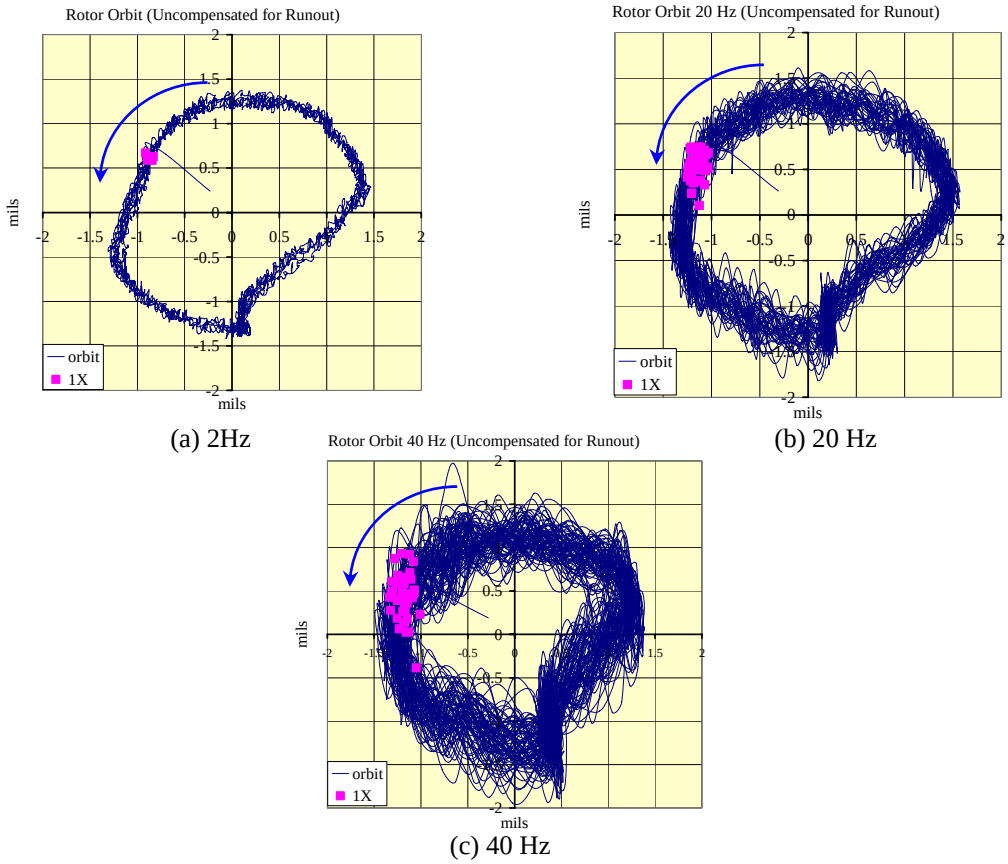

(a) 2Hz (b) 20 Hz

(c) 40 Hz

Figure 5.37 Unfiltered Orbits at 2, 20, and 40 Hz

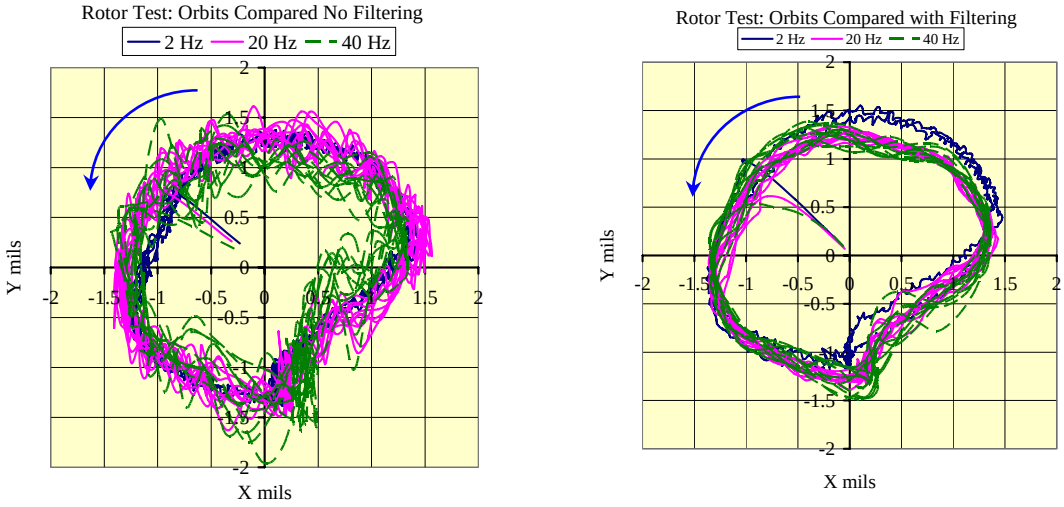

(a) No filtering. (b) Low Pass Filtering

Figure 5.38 Rotor Test: Unfiltered and Filtered Orbits

The last item for discussion regarding the FOGS and ECP sensors are the resulting spectrums, figure 5.39. The time waveforms for both sensors do not fit the profile of a smooth sine wave and the observed orbits are not circular, and with the presence of the protuberance on the bottom of the orbit the resulting spectrums should consist of multiple frequencies. The spectrums show that the ECP has strong 1X, 2X, and 3X components for each test case. The FOGS shows a strong 1X and a minimal 2X component in each test. The 1X level for each sensor does show a decrease in amplitude that could be attributed to increased belt load, imbalance, or other dynamic loading. The 20 Hz and 40 Hz FOGS spectrum do show an increase response levels in a region from about 150 to 400 Hz. This area could represent the transverse response of the sensor head. An averaging scheme could be employed to reduce random events. But, a better solution would be to develop a sensor that would reduce the transverse sensitivity.

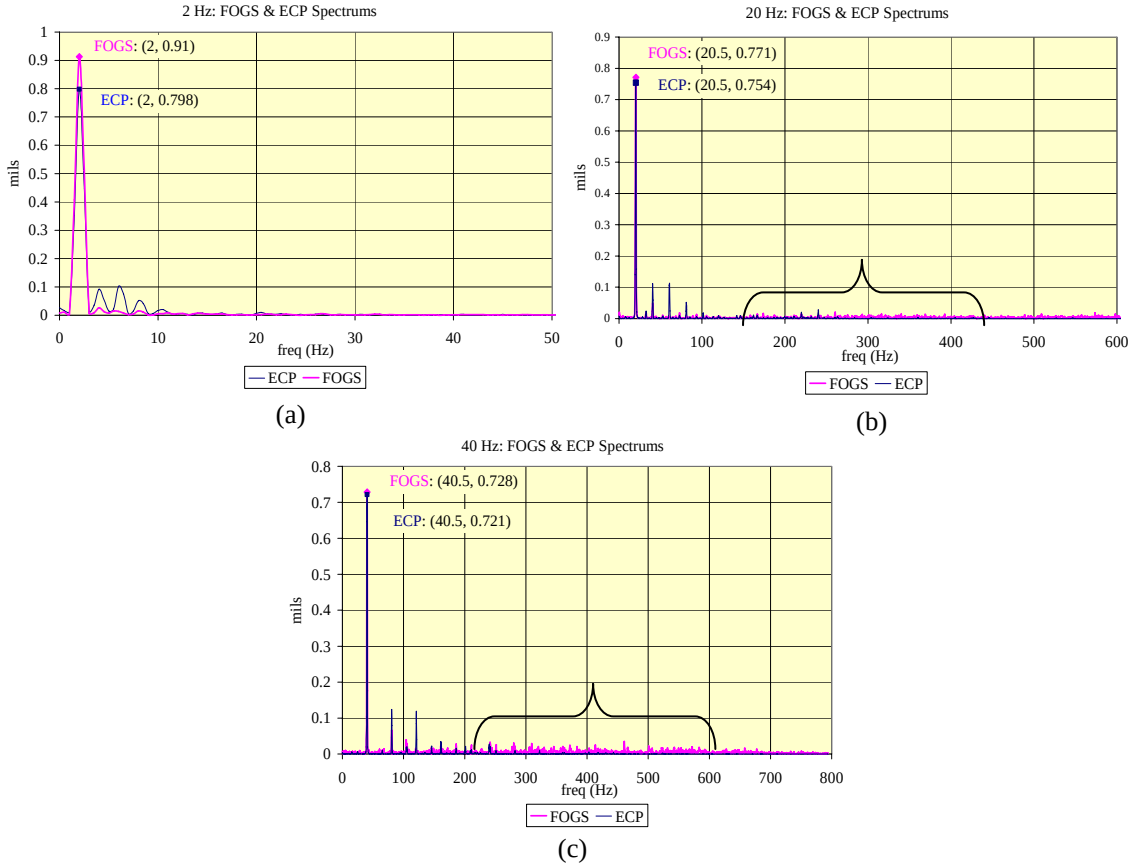

Figure 5.39 Rotor Test: ECP and FOGS Spectrums

The second set of sensors to cover is the accelerometer and FOVS that are attached to the horizontal beam that supports the FOGS. The horizontal beam is connected to the demo rotor base, which is a 1 in. (25.4 mm) thick polymer slab with a 0.0625 in (1.59 mm) stainless steel sheet, by two stiff supports. This results in the horizontal beam reacting primarily to the vibrations that are transmitted through the base generated by both the rotor assembly and by the drive motor. The 2 Hz time trace, figure 5.40 shows that the accelerometer (0.1 g/V) is responding with a noisy signal to the excitations. The FOVS on the other hand does show a very high response to a high

frequency excitation source, but does not show any dramatic response due to the 1X rotor motion. The “g” level displayed for the FOVS does not reflect an actual g-level. The calibration factor obtained for the FOVS from the shaker table test was at 0.1 V/g as an average value. However, this value does not apply if the FOVS happens to experience vibrations its region of resonance frequencies, figure 5.32. Inspection of the other two time traces at 20 and 40 Hz shaft speed shows that the high frequency component in the FOVS is still present with minimal growth in amplitude. A note of caution is required when reviewing the time responses. The rotor speeds used unfortunately coincide with points that border the response peaks of the FOVS found from the shake table tests. This would result in highly inflated response values. But, both the accelerometer and the FOVS show an increase in response that coincides with the speed of the rotor. Inspection of the spectrums shows that the high frequency component is at 120 Hz. The speed controller for the motor utilizes a controlled rectified waveform. This essentially takes a 60 Hz AC input, and rectifies the wave resulting in a 120 Hz signal that goes to the motor. When switching on the motor, there is a noticeable hum and high frequency vibration in the base plate of the rotor can be felt when touched. This 120 Hz appears to be close to some resonant frequencies that the FOVS has aside from the natural frequency of the proof mass. The FOVS shows a significant 1X component at 40 Hz primarily because the rotor table is close to bouncing up and down on its rubber support feet.

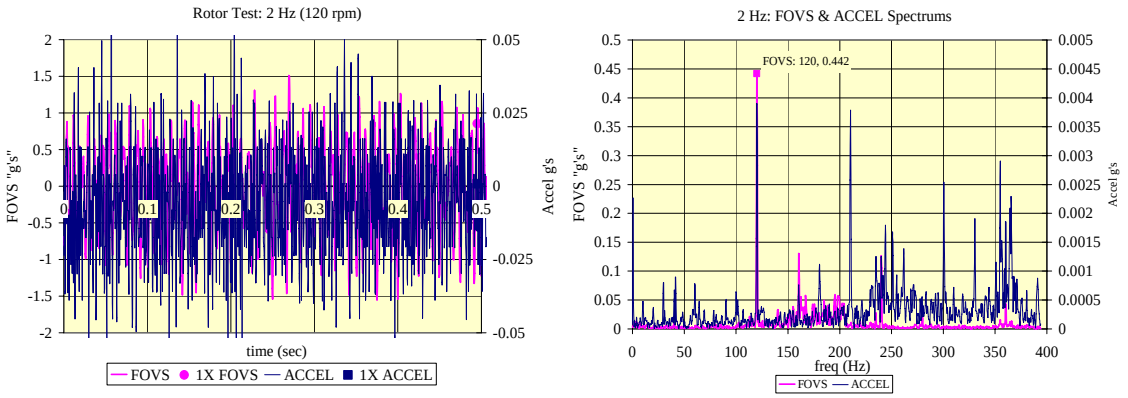

(a) 2Hz

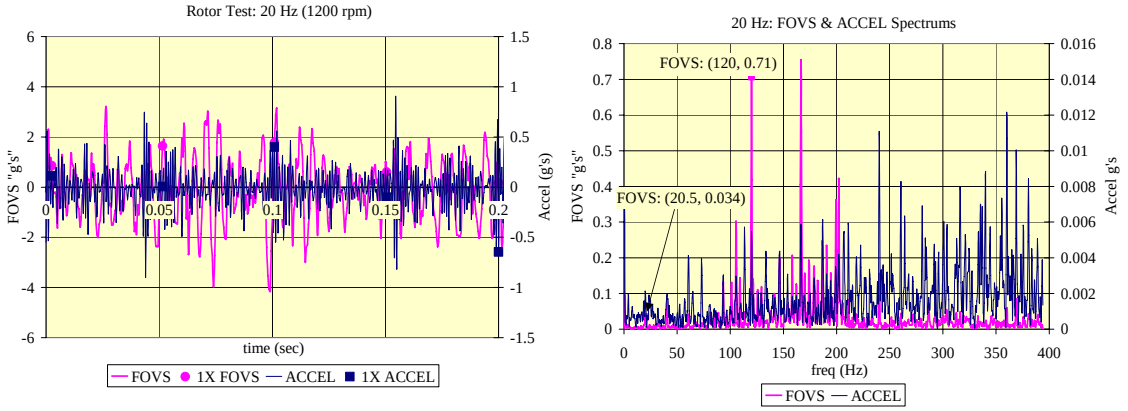

(b) 20 Hz

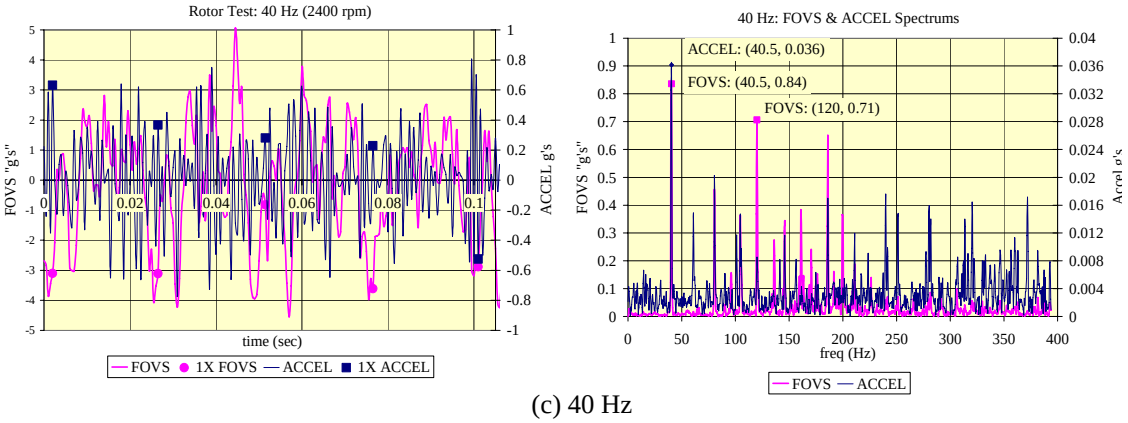

(c) 40 Hz

Figure 5.40 Rotor Test: FOVS and Accelerometer Responses

5.4.3 Rotor Face with Paramagnetic Strips

The ECP responds to any type of metallic structure that passes through the sensing, or eddy field. The FOGS probe has the strongest interaction to ferromagnetic materials and has a negligible response to thin paramagnetic materials such as brass or aluminum. To demonstrate the difference in response between the two sensors, brass shim stock of 1, 2, and 3 mils (0.025, 0.051, and 0.075 mm) thickness, 0.5 in. (12.7 mm) long and 1 in. (25.4 mm) wide were attached to the face of the rotor using super glue. Figure 5.41 shows the rotor face with the shim stock attached such that the 1 mil thickness will traverse the sensors first, then 54^0 later the 2 mil stock will pass, then another 45^0 of rotation results in the 3 mil stock passing.

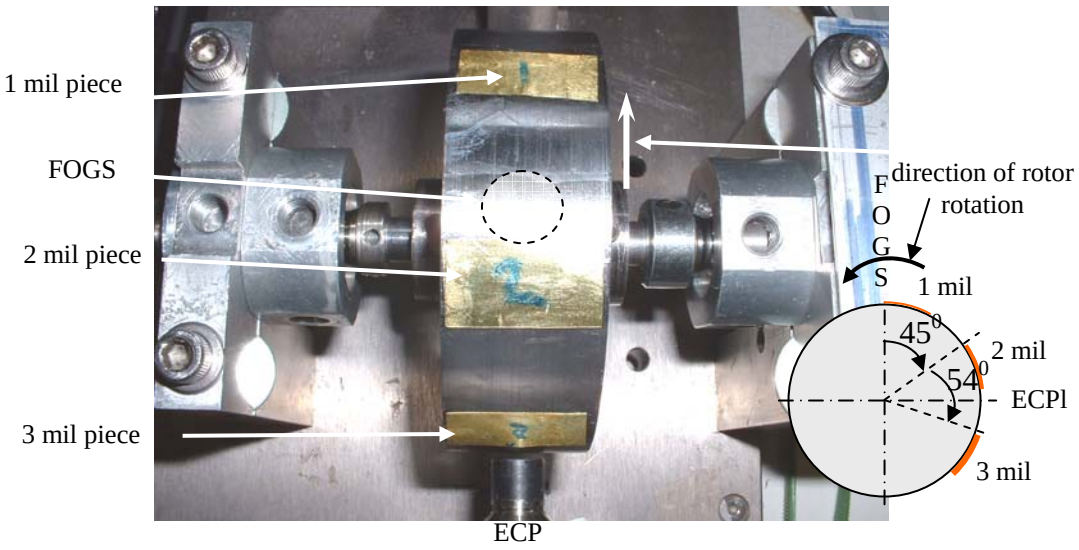

Figure 5.41 Rotor with Brass Shims

The tests are conducted at two speeds and the primary responses of interest are the time waveforms to see how each sensor responds to the “defect” on the shaft surface. Figure 5.42 shows a time response trace for the ECP and FOGS with the shaft speed near 300 rpm (5 Hz). The ECP trace shows three noticeable spikes. The first spike is the passing of the 1 mil strip. An additional observation is that the time waveform does show a noticeable offset when compared to the data for the non-shimmed rotor.

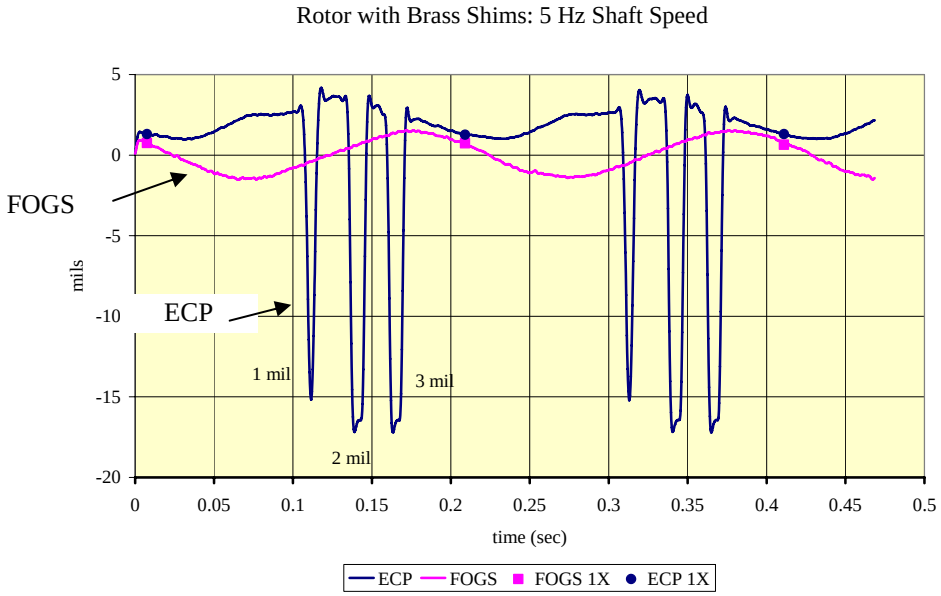

Figure 5.42 ECP and FOGS Shim Response

The FOGS sensor, if it would react to the shims, would display incidents between the 0.15 and 0.2 second time marks, or just as the FOGS responds to the passage of the positive peak of the rotor. An alternative way of examining the traces is to plot the responses relative to the rotation of the rotor. Figure 5.43 shows such a trace. Since the probes are at a 90^0 orientation to each other the affect of a strip seen by the ECP should

then appear on the FOGS 90^0 later. The FOGS trace has two markers to the left of the FOGS 1X marker located near the 400 degree coordinate. The FOGS 1X marker coincides to the 3mil shim, the next marker to the left coincides with the 2 mil, and the next marker coincides with the 1 mil. Again, no noticeable distortion of the response curve is observed. Conducting the same test at a speed of 25 Hz produces similar results, figures 5.44 and 5.45. These data had a low pass filter with a cutoff frequency of 300 Hz applied so that the high frequency components of the FOGS seen in the previous rotor test were reduced.

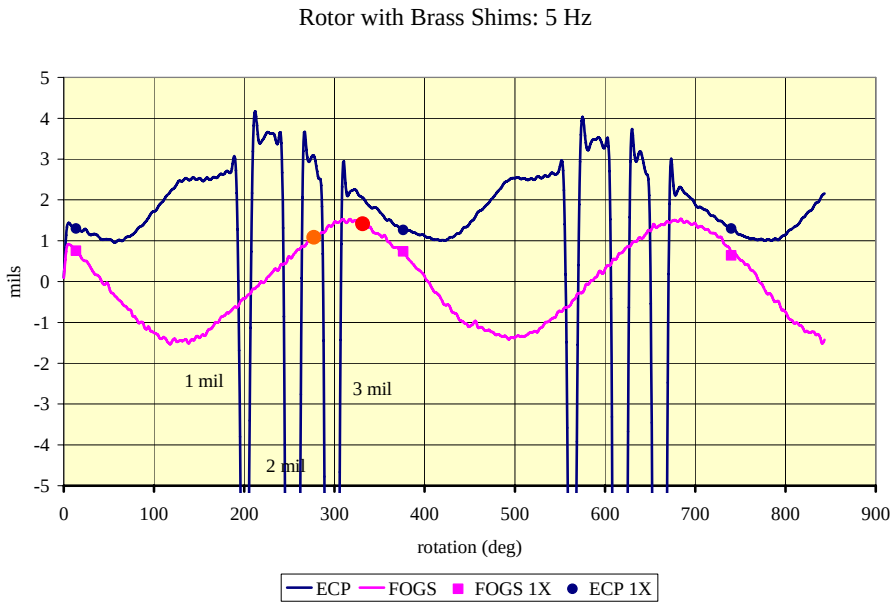

Figure 5.43 Shimmed Response at 5 Hz Referenced to Shaft Angle

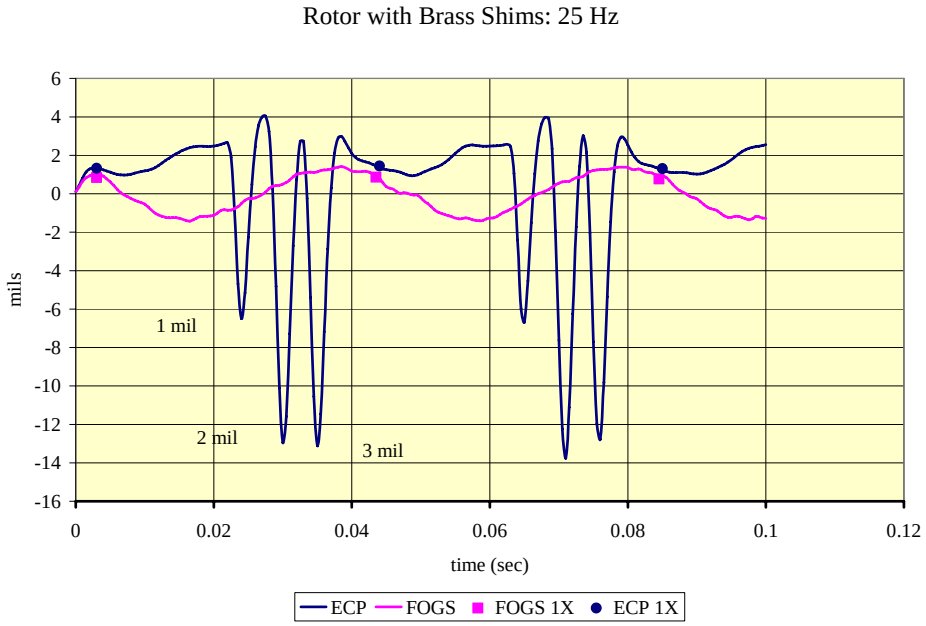

Figure 5.44 FOGS and ECP Shim Response

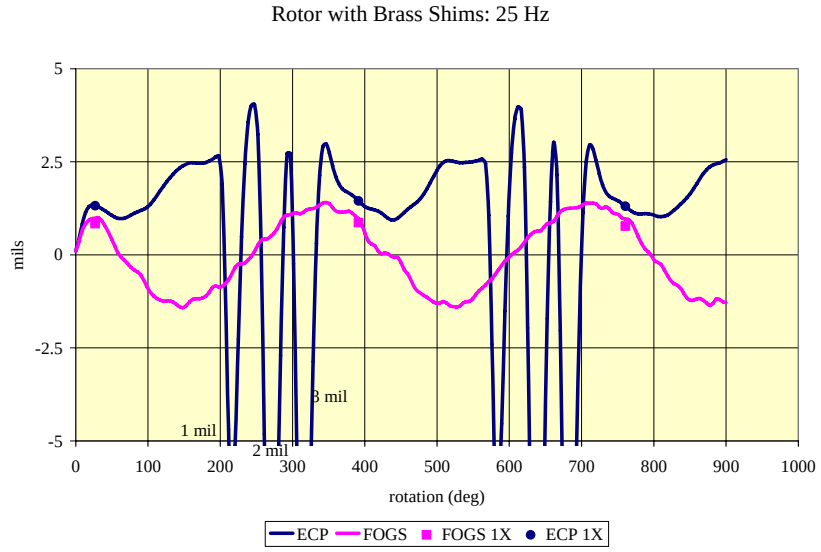

Figure 5.45 Shimmed Response at 25 Hz Referenced to Shaft Angle

5.5 Summary

The response of the FOGS and FOVS when subjected to a series of static and dynamic tests to establish their respective response characteristics was presented. The results for the FOGS sensor showed that the sensor is capable of measuring the gap change and that employment of a set of gap calibration curves can remove the nonlinear effects of the nonlinear force developed on the sensor head due to the gap change. It was also shown that if the gap change was less than 12 mils (0.3 mm) Pk-Pk, then a linear conversion model could be employed. The sensitivity of the FOGS sensor is a function of the initial gap setting, but ranges from 250 mV/mil for a 30 mil gap to 50 mV/mil for a 65 mil gap. The dynamic range of the FOGS sensor is from 0 to 820 Hz (calculated). The response of the FOVS sensor produced a set of mixed results. The peak response frequency can be predicted and observed. However, due to systematic errors from machining and assembly, the response of the sensor produced time waveforms that did not clearly reflect the excitation. The time waveforms indicated that the motion between the proof mass and hypo-tube was restricted or obstructed in some fashion. Acceleration levels around 1.8 *gs* (0-Pk 5 mil at 60 Hz) were high enough to overcome any restrictions of the relative motion between the proof mass and hypo-tube and resulted in time waveform traces that exhibited a “clean” response.

Dynamic tests incorporating a demonstration rotor to show the developed sensors respond when subjected to an array of vibrations. The FOGS was capable of reacting to the Pk-Pk gap change of 2.6 mils caused by the geometric features of the rotor face but exhibited a high frequency content resulting from transverse vibrations. Although the

FOVS showed a response that coincided with the rectified 120 Hz signal used to drive the motor the performance was lacking particular because the rotor speeds coincided with the resonance peak response region, 20 to 40 Hz. A strong 1X signal was observed when the rotor speed was at 40 Hz. Lastly, a test utilizing brass strips ranging in thickness from 1 to 3 mils on the rotor surface showed that the FOGS probe did not react to the strips unlike the ECP which produced severe spikes on the time waveform. This demonstrated a clear advantage of the FOGS probe over the ECP.

The configurations of each sensor presented were initially intended to be a prototype to determine if these simplistic configurations would indeed work. At the onset of this research, access to additional interferometers and other magnet configurations was hoped for. However, these resources did not arise in a timely fashion. Overall, the concept of operation for each sensor was successfully demonstrated.

6 CONCLUSION AND SUMMARY

The need for a set of vibration sensors that do not rely on an electrical source (voltage or current) was met by incorporating the fiber Fabry-Perot interferometer along with permanent magnets. The developed sensors included one that is capable of measuring the vibration of a body across a gap and one that can detect the vibratory motion of a body while being in direct contact with the body. Each sensor incorporates the use of permanent magnets to transfer the excitation source to the sensing FFPI element. Although the developed sensors are essentially a first generation and have inherent issues primarily due to machining and assembly reasons, the basic concepts of operation was confirmed along with the initial steps in modeling their performances.

The Fiber Optic Gap Sensor (FOGS) was capable of reproducing the excited time waveforms when the applied excitation acted along the sensor's axis. The response of the FOGS over large gap changes is non-linear, but the developed scaling scheme was capable in removing the nonlinear issues. Also, if the overall gap motion is less than 10 mils (0.25mm), a linear calibration factor could be applied. The FOGS sensor presented did reach the targeted sensitivity and operation range. The overall sensitivity of the FOGS does vary due to gap and can range from 250 mV/mil (9.84 mV/μm) at a gap of 30 mils (0.076 mm) to 50 mV/mil (1.97 mV/μm) at a gap of 65 mils (1.65 mm). The dynamic range is from 0 to 820 Hz. Tests conducted on the demo rotor kit resulted in inherently noisy time waveforms due to the sensor head possibly banging within the housing due to transverse excitations. Construction that restricts the sensor head better along with damping of the hypo-tube would greatly aid in reducing the transverse

influences. The size of the prototype FOGS was determined by permanent magnets that were on hand and does not reflect on an optimal configuration. More compact FOGS could be developed by customizing the permanent magnets to fit the desired housing. Refinement of the models that can better relate the magnetic field strength to geometry, gap and target, could further reduce the size. That is, the strengths of the magnets used were more than ample and a smaller magnet could be used to reduce the overall size. As an example, providing that the minimum voltage resolution for the system is 2.4 mV, and using the same geometry of hypo-tube, a minimum force of $6.31(10^{-4})$ lbs ($2.81(10^{-4})$N) would be required. One possible approach to a next generation FOGS sensor is to form the entire sensor head out of the permanent magnet, but leave a hole within in it to accommodate the mandrel for the FFPI. An additional approach for the FOGS is to make NdFeB chip and epoxy mixture and coat the FFPI with the mixture, mold it, and then magnetize the chips. One issue of concern in this case is the possibility of introducing birefringence due to kinking of the fiber. Cure rates of the epoxy mixture, fiber preload, and molding could all influence the reduction of birefringence.

The Fiber Optic Vibration Sensor (FOVS) did react to the vibratory excitation sources. However, the performance in the desired region was marginal due to the possible restrictive or obstructive nature of the construction. The sensitivity and dynamic range of the FOVS is difficult to characterize for a large range of motion, but, a response of 0.1 V/g was found from 40 Hz to about 100 Hz. This is a narrow range of operation but could be extended if tighter control of manufacturing and use of damping. to help better constrain the hypo-tube and better constraining of the extra degree of

freedoms of the proof mass and sensor head. Although the force acting between the proof mass and the sensor head is nonlinear in nature, it does not present an issue if the motion is not near the natural frequency of the sensor and if adequate amount of damping is provided. The study of the developed FOVS did not explore the introduction of damping and is left for future examination. An intriguing aspect to examine is that the damping in future generation of FOVS could rely on a combination of fluid and magnetic damping as motion of magnets past certain materials can introduce damping due to the generation of eddy fields. An additional aspect of interest would be to look at the profile of the magnets used between the proof mass and the sensor head especially if a profile could be found that could act to keep the proof mass aligned with the loading axis of the hypo-tube. One drawback of the initial prototype was that large motions of the proof mass resulted in a response that is not symmetrical about the time axis. It could be possible to develop a sensor where the motion of the proof mass results in a symmetrical response from the sensor head. The other item that would be useful to examine is the feasibility of developing the sensor so that it can be operated in the horizontal plane. The existing configuration is for operation primarily in the vertical direction. Lastly, the FOVS might be adaptable for applications where a specific seismic event is desired such as vehicular motion. The FOVS might have the ability to respond to ground tremors induced by motor vehicles that could be used to trigger other monitoring stations. To expand this capability, it could be possible to configure the FOVS with an adjustable gap between the proof mass and sensor head such that it could

be tuned for a specific vibration. This concept could be attractive since the transmission distance of the fiber optic system is on the multiple kilometer level.

Further issues that would be prudent to address is the influence that these sensors might have on what they are measuring. The FOGS probe requires that a force acts between the sensor and the target. It is possible that this force could actually affect the target. To minimize this possibility, assessment of minimum magnetic field and mandrel configuration to FFPI sensitivity needs to be addressed. An example of the possibility of the FOGS influencing the behavior of a body is if the FOGS was used to measure the response of a rotor that is marginally stable. The combination of existing dynamic forces acting on the rotor and the addition of the FOGS could result in the rotor becoming unstable. An additional concern could be the possibility that the FOGS could generate stray currents within the target that could result in arcing, damage to other sensors, or possible explosions. Lastly, the concern of how the magnetic fields of the permanent magnets extend beyond their housing and the possibility that they could impact another device should be addressed. Selection of housing materials could be optimized to reduce the field leakage outside of the sensor.

REFERENCES

[1] American Petroleum Institute, *Machinery Protection Systems*, 4th Edition, 2000, API 670 Machinery Monitoring Guidelines.

[2] National Electrical Code, ANSI/NFPA 70, 2002, National Fire Protection Association, Quincy, MA.

[3] Kent B., Personnel Communication, GE Bently Nevada Houston Office, March 2006.

[4] Hecht, J; 1990, *Understanding Fiber Optics*, Howard W. Sams Company, Carmel, IN.

[5] Wilcoxin Instrumentation Catalog W15, 2002, Gaithersburg, MD.

[6] Lee C.E.; 2003, "Fiber Optic Fabry-Perot Sensor for Machinery Monitoring" in *Proceedings of SPIE Sixth Pacific Northwest Fiber Optic Sensor Workshop*, Vol. 5278 pp. 11-20, Troutdale, OR.

[7] Miller M S Myhre D C, 1999,"Optical Sensors for Turbine Engine Applications", *Proceedings of SPIE 1998 Process Monitoring with Optical Fibers and Harsh Environment Sensors*, Vol. 3538, pp 99-110, Boston, MA**.**

[8] Lee C E Taylor H F, 1998, "A Fiber-Optic Pressure Sensor for Internal Combustion Engines; Sensor", Sensors, **15.3**, pp20-23 Helmers Publishing, Peterborough, NH.

[9] Kimura M, Tosihma K; 1998, "Vibration Sensor Using Optical-Fiber Cantilever with Bulb Lens"; Sensors and Actuators A Physical **66** Elseveir Sciences, pp 178-183.

[10] Zook J D, Herb W R, Bassett C J, Stark, T, Schoess J N, Wilson M L; 2000, "Fiber Optic Vibration Sensor Based on Frequency Modulation of Light Excited Oscillators"; Sensors and Actuators **83**, Elseveir Science, pp 270-276.

[11] Wang T, Zheng S, Yang Z; 1998, "A High Precision Displacement Sensor using a Low-Finesse Fiber-optic Fabry-Perot Interferometer" ; Sensors and Actuators A Physical **69** ; Elseveir Science, pp 134-135.

[12] Bartow M J, Calvert S G, Bayly P V, 2003, "Fiber Bragg Grating Sensors for Dynamic Machining Applications"; *Proceedings of SPIE Sixth Pacific Northwest Fiber Optic Sensor Workshop*, Vol 5278, pp 21-31, Troutdale, OR.

[13] Philips G J; 1982, "The Fiber Optic Bearing Monitor"; International Instrumentation Symposium, 28th, Instrument Society of America, May, pp 379-395, Las Vegas, NV.

[14] Conkey AP Juarez J C Taylor HF, 2003, "Monitoring Rolling Element Bearings Using Fiber Optic Rolling Element Sensing Technology (FOREST)"; *Society for Machinery Failure Prevention Technology 57th Annual Meeting; April 2003*; pp133-147, Virginia Beach, VA.

[15] Atkins K of Engineering Dynamics Inc San Antonio Texas, personnel communication, March 2005.

[16] Eisemmann, R.C.; 1998, *Machinery Malfunction Diagnosis and Correction*, Prentice Hall, Upper Saddle River, NJ.

[17] Childs, D, 2005, *Dynamics and Vibrations Dynamics in Engineering Practice*, 6th edition, Wiley, Danvers, MA.

[18] Harris, C.M., 2002, *Shock and Vibration Handbook* 5th ed.; McGraw-Hill Inc, New York

[19] Campbell, P., 1994, *Permanent Magnet Materials and Their Application*; Cambridge University Press, New York.

[20] Skomski, R. Coey J.M; 1999, *Permanent Magnetism*; Institute of Physics Publishing, Philadelphia, PA.

[21] Furlani, E. P., 2001, *Permanent Magnets and Electromechanical Devices Materials, Analysis, and Applications*, Academic Press, San Diego.

[22] Magnet Sales & Manufacturing, www.magnetsales.com/Design/DesginG_frames/frame_dgbod2.html; 5/25/04.

[23] Reitz JR, 1970, "Forces on Moving Magnets due to Eddy Currents"; Journal of Applied Physics **41** No 5, pp 2067-2071.

[24] Parker, R.J, 1990, *Advances in Permanent Magnetism*; John Wiley & Sons, New York, NY.

[25] Taylor H F, 1995, "Fiber Fabry-Perot Interferometer (FFPI) Sensors"; *50th Annual Symposium on Instrumentation for the Process Industries*, Instrument Society of America, pp 13-17.

[26] Butter C.D., Hocker G.B., 1978, “Fiber Optic Strain Gauge”, Applied Optics, **17**, No. 18., pp 2867-2869.

[27] Sadkowsiki R, Lee C E, Taylor H F, 1995, “Multiplexed Inteferometric Fiber-Optic Sensors with Digital Signal Processing”; Applied Optics, **34**, No 25, pp 5861-5866.

[28] Juarez JC, Conkey A P, Perez R X, Taylor HF, 2003, “Digital and Analog Readout Systems for Fiber-Optic Strain Sensors as Applied to the Monitoring of Roller Element Bearing Systems”; Applied Optics, **42** No 31, pp 6276-6283.

VITA

Andrew P. Conkey started his collegiate career at Texas A&I University, Kingsville Texas. He began his teaching career there during his junior year where he covered Physics labs and Mechanical Engineering labs. He received his Bachelors of Science in mechanical engineering from Texas A&I in 1987. He continued on at Texas A&I to receive his Master's of Science in mechanical engineering in 1990. During this time Texas A&I was renamed to Texas A&M-Kingsville. He stayed on at Texas A&M-Kingsville as a lecturer for nine years. During this time he did minor consulting work, worked on a biomass harvester to harvest primarily mesquite trees. He started his Ph.D. work at Texas A&M in College Station in 1999. During his time at Texas A&M University he worked on a fiber optic roller bearing force sensor, a passive compass for a towed sonar arrays, curriculum material for the freshmen engineering program, was a TA for the dynamics and vibrations class, and provided assistance for a Dynamics and Vibrations text book. In 2001 he received an award for TA of the year from the mechanical engineering department. He completed his Ph.D. of Interdisciplinary Engineering in August 2007. He can be reached through the mechanical engineering department at MS 3123, College Station TX, 77840.